

**Similarity and Versatility of Lanthanides  
Mixed and Matched for Medical Applications**

Mayer, F.

**DOI**

[10.4233/uuid:436de838-0962-4b7f-898b-fe409f565689](https://doi.org/10.4233/uuid:436de838-0962-4b7f-898b-fe409f565689)

**Publication date**

2021

**Document Version**

Final published version

**Citation (APA)**

Mayer, F. (2021). *Similarity and Versatility of Lanthanides: Mixed and Matched for Medical Applications*. [Dissertation (TU Delft), Delft University of Technology]. <https://doi.org/10.4233/uuid:436de838-0962-4b7f-898b-fe409f565689>

**Important note**

To cite this publication, please use the final published version (if applicable).  
Please check the document version above.

**Copyright**

Other than for strictly personal use, it is not permitted to download, forward or distribute the text or part of it, without the consent of the author(s) and/or copyright holder(s), unless the work is under an open content license such as Creative Commons.

**Takedown policy**

Please contact us and provide details if you believe this document breaches copyrights.  
We will remove access to the work immediately and investigate your claim.

# **Similarity and Versatility of Lanthanides**

**Mixed and Matched for Medical Applications**

**Florian MAYER**



# **Similarity and Versatility of Lanthanides**

## **Mixed and Matched for Medical Applications**

Proefschrift

ter verkrijging van de graad van doctor  
aan de Technische Universiteit Delft,  
op gezag van de Rector Magnificus Prof.dr.ir. T.H.J.J. van der Hagen,  
voorzitter van het College voor Promoties,  
in het openbaar te verdedigen

op woensdag 27 oktober 2021 om 10.00 uur

door

**Florian MAYER**

Diplom-Chemiker, Universität Ulm, Duitsland  
geboren te Ehingen an der Donau, Duitsland

Dit proefschrift is goedgekeurd door de promotoren:

Prof. dr. U. Hanefeld

Dr. K. Djanashvili

Samenstelling promotiecommissie:

Rector Magnificus,	voorzitter
Prof. dr. U. Hanefeld	Technische Universiteit Delft, promotor
Dr. K. Djanashvili	Technische Universiteit Delft, promotor

Onafhankelijke leden:

Prof. dr. H.T. Wolterbeek	Technische Universiteit Delft
Prof. dr. L. Tei	Universita del Piemonte Orientale, Italië
Prof. dr. E. Jakab-Tóth	CNRS Orléans, Frankrijk
Dr. ir. J.A. Peters	Technische Universiteit Delft
Dr. ir. R.M. Kruijff	Technische Universiteit Delft
Prof. dr. F. Hollmann	Technische Universiteit Delft, reserve lid

The research described in this thesis was performed in the framework of the 3Binding project “Imaging, Interpretation and Therapy; Innovation in Nuclear Diagnostic and Therapy in Health Care”, which is financially supported by the Dutch Ministry of Economic Affairs and by the Province of Zuid-Holland and in the framework of the COST Actions D38 “Metal-Based Systems for Molecular Imaging Applications”, TD 1004 “Theragnostics Imaging and Therapy: An Action to Develop Novel Nanosized Systems for Imaging-Guided Drug Delivery” and TD 1007 “Bimodal PET-MRI molecular imaging technologies and applications for in vivo monitoring of disease and biological processes”.

ISBN: 978-94-6366-466-0

Copyright © 2021 by Florian Mayer

All rights reserved. No part of the material protected by this copyright notice may be reproduced or utilized in any form or by any other means, electronic or mechanical, including photocopying, recording or by any information storage and retrieval system, without written permission from the author.

Printed in Germany

*To my parents*

*Meinen Eltern*



# CONTENTS

<b>LANTHANIDE PROPERTIES RELEVANT FOR MEDICAL DIAGNOSIS AND THERAPY</b>	<b>1</b>
INTRODUCTION	2
MAGNETIC BEHAVIOR OF LANTHANIDES	4
OPTICAL AND LUMINESCENCE CHARACTERISTICS OF LANTHANIDES	10
RADIOISOTOPES FOR MEDICAL IMAGING AND THERAPY	19
CONCERNS ON THE TOXICITY OF LANTHANIDE-BASED AGENTS	27
RECENT DEVELOPMENTS AND OUTLOOK	29
SUMMARY	31
OUTLINE OF THE THESIS	32
REFERENCES	34
<b><sup>17</sup>O NMR AND DFT STUDY OF THE DYNAMICS OF THE CARBOXYLATE GROUPS IN DOTA COMPLEXES OF LANTHANIDES IN AQUEOUS SOLUTION</b>	<b>39</b>
INTRODUCTION	40
RESULTS AND DISCUSSION	42
CONCLUSIONS	56
EXPERIMENTAL DETAILS	57
REFERENCES	60
<b>LUMINESCENCE PROPERTIES OF SELF-AGGREGATING Tb<sup>III</sup>-DOTA-FUNCTIONALIZED CALIX[4]ARENES</b>	<b>63</b>
INTRODUCTION	64
RESULTS AND DISCUSSION	66
CONCLUSIONS	75
EXPERIMENTAL DETAILS	75
REFERENCES	79
<b>NANOZEOLITE-LTL WITH Gd<sup>III</sup> DEPOSITED IN THE LARGE AND Eu<sup>III</sup> IN THE SMALL CAVITIES AS A MAGNETIC RESONANCE OPTICAL IMAGING PROBE</b>	<b>81</b>
INTRODUCTION	82
RESULTS AND DISCUSSION	85
CONCLUSIONS	98



EXPERIMENTAL DETAILS	99
REFERENCES	103
<b>MICROWAVE ASSISTED SEEDED GROWTH OF LANTHANIDE-BASED NANOPARTICLES FOR IMAGING AND THERAPY</b>	<b>105</b>
INTRODUCTION	106
RESULTS AND DISCUSSION	108
CONCLUSIONS	115
EXPERIMENTAL DETAILS	116
REFERENCES	119
<b>SUMMARY</b>	<b>121</b>
<b>SAMENVATTING</b>	<b>125</b>
<b>LIST OF PUBLICATIONS</b>	<b>129</b>
PUBLICATIONS	129
ORAL PRESENTATIONS	130
POSTERS	130
<b>ACKNOWLEDGEMENTS</b>	<b>133</b>
<b>CURRICULUM VITAE</b>	<b>135</b>

---

# Lanthanide Properties Relevant for Medical Diagnosis and Therapy

# 1

Magnetic Resonance Imaging	163 66	Dy Dysprosium
	157 64	Gd Gadolinium
	165/166 67	Ho Holmium
	150 62	Sm Samarium
Optical Imaging	175/177 71	Lu Lutetium
	159/160 65	Tb Terbium
	144 60	Nd Neodymium
	152 63	Eu Europium

Radioimaging (PET, SPECT) and Therapy

## Introduction

The lanthanides are a series of elements with remarkable properties, located in the center of the periodic table. This family of elements includes 15 members, ranging from lanthanum (a.n. 57) to lutetium (a.n. 71) and forms the group of rare earth elements together with the lighter elements, scandium and yttrium. The latter two are included in this group due to the chemical similarity and the appearance in the same natural sources, however, the electronic and magnetic properties differ significantly from the lanthanides. Despite the name ‘Rare Earth Elements’ (RE elements) the abundance of these elements is not rare at all, with cerium being the most abundant at approx. 60 ppm and thulium being the rarest at 0.3 ppm (excluding promethium, which does not have stable isotopes).<sup>1</sup> With this share, cerium is more abundant than many commonly used metals, such as copper or lead. Rare earth elements never occur individually, but they are always found in mixed minerals of altering composition, which are mainly distributed evenly in the earth’s crust. There are only a few deposits that allow economic and efficient mining.<sup>1</sup>

The first discovery of rare earth minerals was documented in the 18th century in Scandinavia, when Carl Axel Arrhenius (an officer in the Swedish army) found a dark mineral close to the village of Ytterby. This mineral, which he called ‘ytterbite’ was later renamed to ‘gadolinite’ in honor of Johan Gadolin and contains mainly cerium and yttrium amongst several other non-rare-earth elements. The location of the first discovery has later inspired the scientists to name four of the elements (yttrium, terbium, erbium and ytterbium) after the village. In addition, some of the lanthanides were named in relation to north-European places, scientists or mythology. Nowadays, the deposits in Scandinavia are not relevant for the world production of rare earth and lanthanide elements anymore. The only two major global players are China and Australia. All other countries, such as Brazil, South Africa and India, make up a low percentage of the worlds production.

With the discovery of ytterbite in 1787, the long quest to identify and separate the individual elements only started and it took 120 years, until 1907, to isolate the last one of the stable rare earth elements.<sup>2</sup> This long period and the large number of renowned scientists that were working in this field impressively indicates how similar the chemical properties of all the rare earth elements are. Early attempts to separate the elements were focusing on precipitation and crystallization methods, resulting in an initial separation of the element

oxides into two groups. The so-called cerium earths and yttrium earths differ significantly in the solubility of the attributed sodium rare-earth double sulphates. However, the isolation of single elements with these methods was limited and resulted in many wrong claims of new elements due to different inseparable mixtures of the rare earth oxides. Probably the most famous of these wrong claims was didymium, which was discovered in 1841 by Carl Mosander.<sup>3</sup> Identifying the individual elements was significantly improved after the invention of spectroscopy in 1850, however, the separation methods remained highly sophisticated, so that the components of didymium were only separated in 1885 by Carl Auer von Welsbach by a fractional crystallization of the double ammonium nitrates.<sup>4</sup> Due to the color of the one part, he named this element praseodymium (from Greek: green didymium), while he called the other neodymium (from Greek: new didymium).

For modern production of rare earth elements, the minerals are digested with acids and/or bases or treated with chlorine at high temperatures (such as in case of monazite) to result in mixtures of soluble RE salts. The actual separation, nowadays, is done by liquid-liquid extraction, in which complexing agents in organic solvents are used as extraction medium. In this process, the RE elements are extracted into the organic phase and can be precipitated by oxalates, hydroxide or carbonate anions. The precipitates are calcined to result in pure oxides. These oxides can subsequently be dissolved in acids to yield pure salts of the rare earth elements. The metallic elements are mainly prepared by smelt electrolysis of the associated chloride or fluoride salts.<sup>1</sup> As an alternative, but less commonly used separation method, ion-exchange and elution with complexing agents is applied. However, in industrial scale the liquid-liquid extraction is most efficient.

The astonishing chemical similarity of the lanthanides finds its basis in the electronic configuration of the elements. Due to the peculiar location in the center of the periodic table and in the first period that involves f-orbitals, the general electronic configuration can be written as  $[\text{Xe}] 6s^2 5p^1 4f^n$  (with  $n = 0$  for lanthanum and  $n = 14$  for lutetium). Although being valence electrons, the 4f electrons are shielded by the electrons in the larger orbitals of the 5<sup>th</sup> and 6<sup>th</sup> shell, so that they are not readily available for interactions with ligands, therefore, the number of 4f electrons does not contribute to the chemical bonding of the elements. The other valence electrons in the 6s and 5p orbitals are ready for oxidation and as these are the same for all elements along the series, the predominant oxidation state of all elements is  $\text{Ln}^{3+}$ . However, some do appear in stable  $\text{Ln}^{2+}$  and  $\text{Ln}^{4+}$  states as well, especially if this state leads

to empty, half or completely filled 4f orbitals (e.g.,  $\text{Eu}^{2+}$  and  $\text{Tb}^{4+}$  with  $4f^7$  and  $\text{Yb}^{2+}$  with  $4f^{14}$  configuration). The consecutive filling of the shielded 4f orbitals along with the increasing number of protons in the atomic core leads to a stronger attraction of the orbitals by the higher charge in the core and thus to a decrease in the ionic radius along the lanthanide series (from 122 pm for  $\text{La}^{3+}$  to 103 pm for  $\text{Lu}^{3+}$  in 9-coordinated complexes). The so-called lanthanide contraction is the main reason for the small differences that exist amongst the lanthanides.<sup>5,6</sup> The different ionic radii lead to slightly different binding energies, hydration energies, lattice energies etc. which are the basis for all separation techniques.

In contrast to the similarity of the chemical properties, the physical characteristics are extremely diverse. The magnetic properties of the  $\text{Ln}^{3+}$  ions range from diamagnetic  $\text{La}^{3+}$  and  $\text{Lu}^{3+}$  to paramagnetic ions with as much as seven unpaired electrons in  $\text{Gd}^{3+}$  and very high magnetic moments.<sup>7</sup> Next to the magnetic properties, the lanthanides also display interesting optical and luminescent properties due to narrow  $f-f$  transition bands in the range from UV to NIR, often occurring with large Stokes shifts.<sup>8,9</sup> Due to the above described shielding of the 4f orbitals, the luminescence properties are hardly affected by the chemical surrounding of the ion. Furthermore, all lanthanides have radioactive isotopes, which can be used in nuclear medicine. These interesting physical properties determine the applications of lanthanides in modern life, e.g. in magnets, ceramics, catalysts, TV screen phosphors, as metallurgical components, catalysts, neutron absorbers<sup>10</sup> and in medical applications.<sup>8,11-14</sup> Especially for medical applications, the abovementioned properties display unbeatable advantages. In the following chapters of this introduction, the key properties will be discussed in relation to medical applications and along with further aspects on the use of lanthanides *in vivo*.

## **Magnetic behavior of lanthanides**

One of the most prominent physical properties of the lanthanide elements is their paramagnetic character. This property is of highest interest for medical diagnosis where it can be used to increase the contrast in magnetic resonance imaging (MRI).<sup>7,11,15</sup> This technology visualizes the differences in the relaxation rates of water protons in neighboring tissues without the use of ionizing radiation and with an excellent spatial resolution and

almost unlimited penetration depth. While still more than half of the MRI scans is performed without contrast agents at all, their use is increasing ever since the first commercial agents were available in the 1980s.<sup>16</sup> This increasing popularity is based on the performance and availability of MRI contrast agents. In addition, they are stable and not costly, compared to e.g., radionuclide imaging agents, which makes them easy to handle and apply. However, in recent times, some concerns were raised regarding the safety and long-term effects of lanthanide-based contrast agents.<sup>17</sup> These concerns will be discussed later in this introduction as they are relevant for all applications of lanthanides *in vivo*.

The suitability of lanthanide ions for the application in MRI is based on the high number of unpaired electrons. The most widely applied contrast agents until nowadays are small complexes of  $Gd^{3+}$  with different chelating ligands, such as cyclic DOTA (1,4,7,10-Tetraazacyclododecane-1,4,7,10-tetraacetate) or linear DTPA (Diethylenetriamine-*N,N,N',N,N'*-pentaacetic acid) and their derivatives (see Figure 1.1).<sup>16</sup> These structures were also the first commercially applied contrast agents. They are especially useful in cases, in which the tissue of interest and its surrounding have very similar properties and therefore, the differences in water  $^1H$  signal intensities are low. Paramagnetic agents that are introduced to the tissue can enhance the relaxation rates of the water  $^1H$  in close proximity, and consequently, increase the contrast between tissues with different concentrations of the paramagnetic compounds. The contrast enhancement by a paramagnetic agent is typically given as its relaxivity ( $R_i = 1/T_i$ ,  $i = 1,2$ ). It is usually quoted as a rate ( $s^{-1}$ ) and is normalized versus the concentration of the agent ( $mM^{-1}$ ). This number ( $r_i$ ) indicates the effectiveness of a contrast agent and can be applied for positive as well as negative agents.

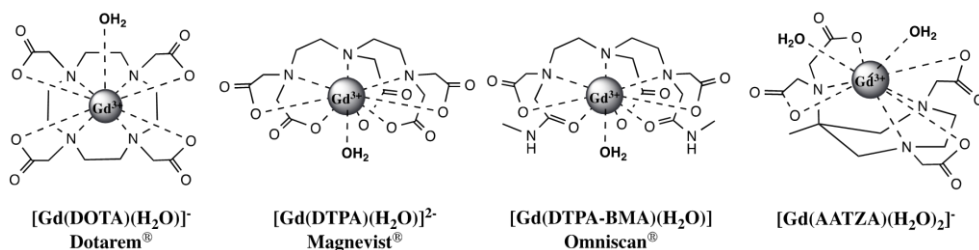


**Figure 1.1.** Clinically applied Gd-containing MRI contrast agents and optimized complex with increased relaxivity (AAZTA) with the corresponding relaxivity values measured at 1.5T and 25 °C.<sup>18</sup> Since 2017, the use of Gd-DTPA-BMA is suspended in the EU (see Table 1.3).

Depending on whether the longitudinal or transverse relaxation rates are most affected, paramagnetic compounds are considered positive ( $T_1$ ) or negative ( $T_2$ ) contrast agents, respectively.<sup>7</sup>  $T_1$  agents give rise to bright spots in  $T_1$ -weighted MRI images, while  $T_2$  agents reduce the intensity in  $T_2$ - and  $T_2^*$ -weighted images. For the ease of interpretation, positive contrast agents were favored over negative ones, but nowadays this issue can be solved by applying specific pulse sequences to invert the contrast and to suppress the background.<sup>19,20</sup> Typical representatives of  $T_1$  agents are small  $Gd^{3+}$ -containing complexes, while for  $T_2$  agents the high effective moments of other  $Ln^{3+}$  (Dy, Ho, Tb) are more favorable. Especially at high magnetic field ( $B_0$ )  $T_2$  agents are much more efficient than  $T_1$  agents as the relaxation enhancement for  $T_1$  decreases at higher field while the one for  $T_2$  increases.<sup>7</sup>

In order to understand the longitudinal relaxivity of a Gd-chelate, the Solomon-Bloembergen-Morgan and the Freed theories can be applied.<sup>15,21,22</sup> While the first one describes the contributions of the water molecules in the inner sphere of the Gd-chelate, the latter one details the outer sphere contribution. With these theories it becomes obvious that complexes can be designed in a way that their relaxivity increases. The main parameters that can be optimized are the number of water molecules in the first coordination sphere ( $q$ ), the residence time in the first coordination sphere ( $\tau_M$ ) and the rotational correlation time ( $\tau_R$ ) (Figure 1.2). Further parameters that impact the relaxivity are the electronic relaxation times and the diffusion correlation time ( $\tau_D$ ), but these are not easily adjustable by the design of the complexes.

The relaxivity of  $T_1$  agents is generally low for small molecule complexes, with a range from  $2 - 6 \text{ s}^{-1} \text{ mM}^{-1}$  at  $37 \text{ }^\circ\text{C}$  and  $1.5\text{T}$ , when compared to the theoretical maximum, which is approx.  $80 \text{ s}^{-1} \text{ mM}^{-1}$ , if all parameters governing the relaxivity were optimal. This leaves a tremendous amount of space for improvement via the three abovementioned parameters. All commonly applied contrast agents consist of a central  $Gd^{3+}$ -ion, coordinated by octadentate ligands. This results in one inner sphere water molecule ( $q = 1$ ). As the inner sphere relaxivity directly correlates with the number of inner sphere water molecules,  $q > 1$  complexes are favorable in terms of  $r_1$ . However, the accommodation of two or more water molecules is sterically demanding and only possible with ligands of lower denticity. Unfortunately, the reduced denticity consequently leads to a lower thermodynamic and kinetic stability of the complex, which is highly unfavorable in view of the toxic properties of free  $Gd^{3+}$  ions *in vivo*. If the free binding sites of the water molecules are next to each other, the contrast agent can

be deactivated by displacement of the water molecules by bidentate endogenous ions, which is another disadvantage of  $q = 2$  complexes. In order to increase  $q$  without having the aforementioned limitations, special ligands were designed. One of the most promising candidates is the heptadentate AAZTA ligand, which allows the accommodation of two separated inner sphere water molecules ( $q = 2$ ) in combination with a still very high thermodynamic and kinetic stability. The  $Gd^{3+}$ -complexes of AAZTA have significantly higher relaxivities than the octadentate complexes.<sup>23,24</sup>

The optimization of  $\tau_M$ , which represents the rate of the water-exchange between the inner coordination sphere and the bulk water, is another option to optimize the relaxivity of contrast agents. Studies reveal that water-exchange is mostly driven by a dissociative, stepwise mechanism. In the first step, the bound water is expelled from the inner sphere and only in the second step, the new water molecule from the bulk enters. The first step is rate limiting and can be accelerated by increasing the steric strain around the water binding site. This leads to a decrease of the difference of free enthalpies of the water bound and water-free stages. However, this is only applicable to a certain extent, because too high steric strain results in a terminal expulsion of the water molecules from the inner coordination sphere<sup>25</sup>. A sharp maximum of the relaxivity can be predicted for  $\tau_M \sim 20$  ns for low magnetic field strength, while the relaxivity is less sensitive for  $\tau_M$  at higher magnetic fields with a wide optimum from 1-100 ns. However, the currently applied contrast agents have higher and thus poorly suitable  $\tau_M$  values.<sup>21,26,27</sup> Close to optimal  $\tau_M$  values are often found in complexes that have a broken number for  $q$  ( $q < 1$ ) due to the high steric strain in these compounds.

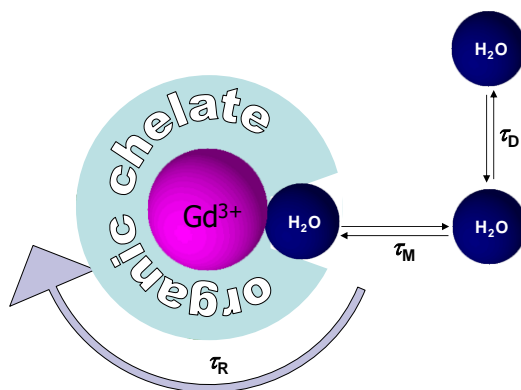


**Figure 1.2.** Schematic representation of the main parameters governing  $r_1$  of a Gd-complex.



The rotational correlation time ( $\tau_R$ ) is a value for the tumbling of the Gd moiety. To increase the  $\tau_R$  values of contrast agents, the overall molecular volume needs to be increased along with a high local rigidity of the whole compound. Increased  $\tau_R$  values can be achieved by, either covalently or non-covalently, connecting small molecule Gd complexes to large volume carriers, such as biopolymers (e.g. peptides<sup>28</sup> or polysaccharides<sup>29</sup>). With this strategy, the overall molecular weight is dramatically increased, and multiple Gd-moieties can be attached to one large molecule. The relaxivity per molecule is then the sum of the contributions of all Gd-moieties. However, the connection of the Gd needs to be rigid to reduce internal motion, which would lead to reduced local  $\tau_R$  values. Only in rigid systems  $\tau_R$  of the complete molecule equals  $\tau_R$  of the individual attached Gd-centers. However, it has to be considered that this change in the molecular size and characteristics might lead to an altered biodistribution. The residence time *in vivo* is increasing and the excretion path for large molecules is most likely a hepatic excretion, while small complexes are quickly cleared from the bloodstream via the kidneys.

The effect of  $\tau_R$  on the relaxivity is only relevant at low magnetic field strength (<1.5T). Upon increase to  $B_0 = 2T$ , the effect becomes negligible and might even turn negative at higher field strength. As this contribution fades away with increasing magnetic field, the theoretical maximum of  $r_1$  is decreasing with higher field strength, from 80 to 18 s<sup>-1</sup> mM<sup>-1</sup> at 1.5 and 9.4 T, respectively.<sup>30,31</sup>

An elegant example of a small molecule Gd<sup>3+</sup>-complex that reversibly binds to human serum albumin is MS-325,<sup>32</sup> which can be used as blood pool agent. An aqueous solution of the compound displays a relaxivity of 6.6 s<sup>-1</sup> mM<sup>-1</sup>, while the relaxivity increases to values of 30-50 s<sup>-1</sup> mM<sup>-1</sup> in the presence of HSA due to the optimized  $\tau_R$  values. The reversible binding results in constantly low concentration of free complexes in the blood stream that can be excreted steadily via the kidneys.

Next to the inner sphere water, which is in direct contact with the paramagnetic center, there can be additional water molecules that contribute to the overall relaxivity. These second sphere water molecules have to reside in close proximity of the complex for a long time, compared to the typical  $\tau_D$  values.<sup>33</sup> In the commonly used Gd-DOTA or Gd-DTPA complexes, this contribution is negligible, however, when the ligands are designed to form hydrogen bonds with water molecules or they bear water-exchangeable protons, this usually

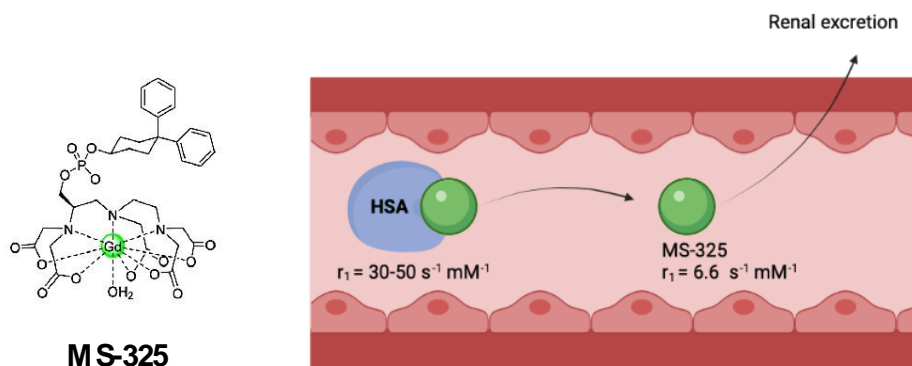


**Figure 1.3.** Molecular structure of MS-325; charges are omitted for clarity and schematic representation of MS-325 as blood pool agent.<sup>15</sup>

leads to a significant increase of the second sphere effect. In complexes, in which one or more of the carboxylate groups is substituted by phosphonate groups, a significant number of second sphere water molecules ( $q_{ss}$ ) can be determined. For phosphonate exchanged DOTA,  $q_{ss}$  increases from 1 to 3.3 upon exchange of 1 or 4 carboxylates, respectively.<sup>34</sup> Another approach is to add molecules with a high number of hydroxylic groups to the backbone of the original ligand and create a well-defined second water sphere. The example of  $\text{Gd}(\text{DOTA-Glc}_{12})(\text{H}_2\text{O})$  impressively shows that this approach can result in  $q_{ss}=8$ , and consequently, a second sphere contribution of 45% to the overall relaxivity.<sup>35</sup>

In contrast to  $T_1$  agents, for  $T_2$  agents the relaxivity is not decreasing with higher magnetic field strength.<sup>7</sup> Especially the trend towards higher magnetic field strength in MRI is more and more evident due to the number of advantages that arise in respect to e.g. spatial resolution and examination times. Therefore,  $T_2$  contrast agents become increasingly attractive, especially for high-field applications. In addition to the low molecular weight complexes, paramagnetic nanoparticles can function as negative contrast agents. Due to the highest effective magnetic moments of all lanthanides,  $\text{Dy}^{3+}$ ,  $\text{Ho}^{3+}$  and  $\text{Tb}^{3+}$  are most suitable for  $T_2$  applications, but also  $\text{Gd}^{3+}$  at higher concentrations and at high magnetic fields can show a significant and predominant  $T_2$ -shortening.<sup>36,37</sup> For paramagnetic complexes the most important parameters governing  $r_2$  are identical with those for  $r_1$ , being  $\tau_M$ ,  $\tau_R$  and  $\tau_D$ , but additionally,  $\Delta\omega$ , which represents the chemical shift difference of the Larmor frequencies of

water protons of Ln-bound water compared to the ones in the bulk water (at infinite distance), plays a role. In contrast to  $T_1$  agents,  $\tau_M$  values for  $T_2$  agents should be significantly longer to enable maximum relaxivity ( $0.1 - 10 \mu\text{s}$ ).<sup>7</sup>

To deliver the highest concentrations of  $\text{Ln}^{3+}$  ions to the site of interest, nanoparticles can be used. These particles can be made of  $\text{Ln}_2\text{O}_3$ ,<sup>38,39</sup>  $\text{LnF}_3$ ,<sup>40</sup>  $\text{NaLaF}_4$ <sup>41</sup> or other insoluble Ln materials such as oxysulphides<sup>42</sup> and phosphates,<sup>43,44</sup> and have the highest possible lanthanide density. The number of Ln-ions that can be delivered with one particle is tremendous, compared to the chelates (up to  $10^6$  ions in a particle of 50-100 nm size). The relaxivity of nanoparticles dispersions, alike the relaxivity of the chelates, consists of an inner sphere and an outer sphere contribution. As only the first lanthanide layer on the surface is relevant for the inner sphere contribution (bulk material is not accessible for water) but the sum of all magnetic moments of the particles is responsible for the outer sphere contribution, the ratio between the two changes with diameter. Especially for larger particles (up to 60 to 80 nm) the outer sphere contribution is largely dominating with respect to the inner sphere contribution. This is useful for *in vivo*  $T_2$ -applications, because due to the toxicity of free lanthanide ions, the particles need to be coated to avoid leaching of free ions,<sup>39</sup> which has a negative effect on the accessibility of the surface ions for water. At particle sizes larger than 60 to 80 nm, the outer sphere model is not applicable anymore and the relaxivities of particle suspensions are not predictable with the herein described conditions. Nevertheless, for nanoparticles up to the abovementioned sizes, the  $r_2$  is proportional to  $B_0^2$  and  $\mu_{\text{eff}}$ ,<sup>4</sup> showing no saturation up to a field strength of 30 T.<sup>45,46</sup> This makes lanthanide containing nanoparticles especially interesting in comparison to iron oxide nanoparticles that also show high potential as negative contrast agents, as the latter experience saturation of the relaxivities at higher magnetic fields.

## **Optical and luminescence characteristics of lanthanides**

Due to their highly interesting and unique optical properties, lanthanides are applied in many fields, where these characteristics can be used. Some of the most prominent examples include lasers, optical filters, phosphors in TV sets, and fluorescent lamps and anti-

counterfeiting inks in euro banknotes. However, in this introduction, the focus will be put on medical application of the optical properties.

Optical imaging is, just as MRI, one of the imaging modalities that does not apply ionizing radiation. Another huge advantage is the ultrahigh sensitivity of this technique, which can detect contrast agents in the low nM concentration range and allow for multichannel detection by applying different lanthanide centers.<sup>8,14,47-49</sup> This sensitivity is several orders of magnitude higher than the one for MRI contrast agents and this is why the agents can be applied or detected at much lower concentrations.<sup>12</sup> Disadvantages compared to MRI are the lower spatial resolution and, most obviously, the reduced penetration depth of visual and NIR light in tissues (approx. 10 cm as a maximum). Nevertheless, lanthanide-containing optical imaging probes display multiple benefits and are highly interesting for specific applications in biomedical analyses and preclinical imaging. One of the most prominent advantages is the relatively long luminescence lifetimes, which allow time-resolved detection, and therefore, minimize the background signal from autofluorescence and scattering from biological tissues. In addition, lanthanide emission spectra show sharp and characteristic emission bands, which are hardly affected by the chemical environment of the lanthanide center and range from UV (Gd) via VIS (Pr, Sm, Eu, Tb, Dy) to the NIR region (Nd, Ho, Er, Tm, Yb) of the electromagnetic spectrum (see Figure 1. 4).<sup>8,50</sup>

There are three different types of transitions in lanthanide complexes. However, ligand to metal charge transfer and  $4f - 5d$  transitions are energetically too high for bio-applications, so that only one applicable transition remains relevant.<sup>51</sup> The aforementioned sharp bands with the long luminescence lifetimes suitable for biomedical imaging predominantly originate from  $f-f$  electron transitions between the  $4f$  orbitals of the  $[Xe] 4f^n$  configuration ( $n = 1$  to  $13$ ) of the  $Ln^{3+}$ -ions, which are formally forbidden by the spin selection rule. These orbitals are well-shielded by the  $5s$  and  $5p$  orbitals, thus the chemical environment does not significantly affect the energetic levels. In addition, it was shown that some  $Ln^{3+}$ -ions are fluorescent ( $\Delta S=0$ ), some are phosphorescent ( $\Delta S>0$ ), and some are both. The  $f-f$  transitions can be divided into magnetic dipole transitions and electric dipole transitions, of which the first ones are parity allowed, while the latter ones are parity forbidden. However, several mechanisms are discussed that relax the rule and result in partially allowed electric dipole transitions, due to e.g., changes of the symmetry in the chemical environment of the

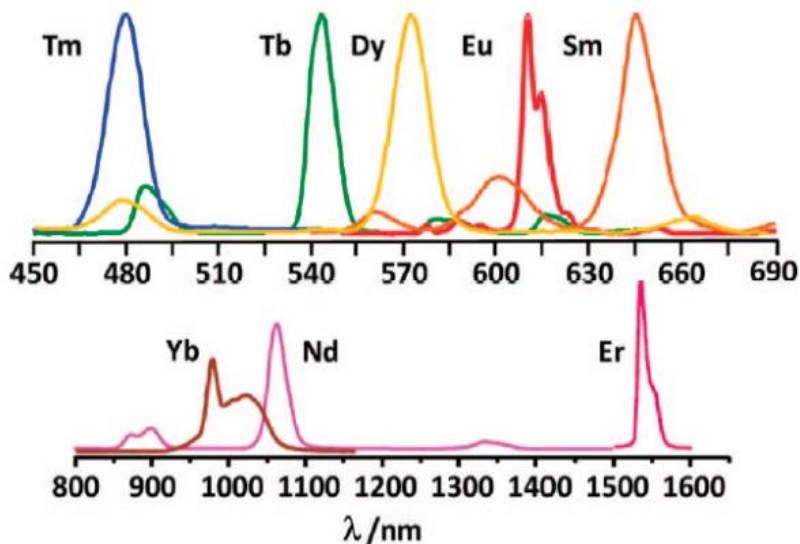


**Figure 1.4.** Luminescence emission spectra of lanthanide tris( $\beta$ -diketonates).<sup>8</sup> 2010 Copyright American Chemical Society.

lanthanide center.<sup>8,50,52</sup> The term induced electric dipole transitions was implemented for this phenomenon, and as a result, electric as well as magnetic dipole transitions contribute to the overall transitions.

Just as the relaxivity ( $r_1$ ) for MRI contrast agents, the quantum yield  $\Phi$  is the parameter that describes the efficacy of an optical imaging agent. The quantum yield is defined as the ratio of the emitted photons divided by the number of the absorbed photons. If only the direct excitation of the 4f-levels of the lanthanide center is considered,  $\Phi_{Ln}$  is called the intrinsic quantum yield. However, as the direct sensitization of the lanthanide ions shows only a very weak absorption, powerful light sources (e.g., lasers) must be used to excite a detectable number of Ln-ions. These powerful light sources are not suitable for biological applications and thus, it becomes obvious that the quantum yield is not the only aspect that defines the performance of an optical imaging agent. The ability to absorb light (molar extinction coefficient  $\epsilon$ ) is equally important to obtain a significant luminescence signal. It must be stressed that the intrinsic quantum yield is highly dependent on the energy gap between the emissive and the receiving state of the luminescent center and thus on the emitted wavelength. The smaller this  $\Delta E$ , the higher the probability of non-radiative deactivation, e.g. by vibrational mechanisms in the coordinated ligands, so that the quantum yields for NIR

emission are generally lower compared to those for shorter wavelengths. Especially, the high energy vibrations of O-H, N-H and C-H bonds are efficiently quenching the radiative mechanisms.<sup>53</sup>

Next to the intrinsic quantum yield  $\Phi_{Ln}$ , the overall quantum yield  $\Phi_{Tot}$  can be considered to give a better understanding of the efficacy of a probe in total. The most obvious difference is that this number also includes indirect excitation of the lanthanide ions. Due to the above-mentioned low absorbance of the lanthanide centers themselves, other excitation pathways are of highest significance for the design of an efficient optical imaging agent. The most important and simplest option is to utilize certain organic moieties in or on the ligands as antenna for the absorption of the excitation energy.<sup>53,54</sup> This process is highly complex and will not be discussed in detail in this chapter, nonetheless, the principle of the antenna effect is displayed in a simplified way in Figure 1.5. The light absorption is achieved via a chromophore in the proximity of the lanthanide center. In the first step, the chromophore itself is excited to the singlet state ( $S_1$ ) by the absorbed photon. The intersystem crossing is the second step that yields the longer-lived triplet state  $T_1$  of the antenna, which is the main donor state for the energy transfer from the antenna to the lanthanide center (step 3). The  $S_1$  state can also function as donor state, but due to the short lifetime, it is less likely to occur. In the fourth and last step the excited lanthanide center emits a photon to return to the ground state. Due to the individual steps and non-radiative relaxation contributions, the wavelength shift from the absorbed light to the emitted light can be significant. This so called Stokes shift, depends on the nature of the antenna as well as the type of lanthanide and is different for every complex.<sup>55</sup>

The overall quantum yield  $\Phi_{Tot}$  consists of contributions of each of the steps described above. As the first step occurs with a 100% probability after absorption of a photon, this step is a factor of 1 and can be omitted, so that  $\Phi_{Tot}$  can be calculated as:

$$\Phi_{Tot} = \Phi_{Ln} \eta_{ISC} \eta_{ET} \quad (1)$$

with  $\eta_{ISC}$  being the efficiency of the intersystem crossing and  $\eta_{ET}$  being the efficiency of the energy transfer from antenna to lanthanide center. These two can be combined to give the overall efficiency of the sensitization  $\eta_{sens}$  and the overall quantum yield:

$$\Phi_{Tot} = \eta_{sens} \Phi_{Ln} \quad (2)$$

The total emission intensity (B = brightness) can thus be calculated as:

$$B = \varepsilon \Phi_{Tot} = \varepsilon \Phi_{Ln} \eta_{ISC} \eta_{ET} \quad (3)$$

with  $\varepsilon$  being the molar extinction coefficient of the probe.

From these considerations it becomes obvious that there are three main parts in the design of a lanthanide based luminescent probe: the lanthanide center itself, the chelate for protection and the antenna, which is usually covalently connected to the chelate. With this knowledge, optimal probes for *in vitro* as well as *in vivo* applications can be designed by tuning either of the main parts. However, multiple aspects with respect to chemical, biochemical and photophysical properties need to be considered in the design to ensure applicable imaging probes.

Chemical requirements are similar to the ones of other lanthanide-based imaging probes and include water solubility, and most importantly, thermodynamic and kinetic stability of the complexes at physiological pH and in biological media. The biochemical requirements strongly depend on the intended application and differ for *in vivo* and *in vitro* purposes. While *in vitro* applications mainly require a highly specific interaction with the intended target and the absence of cytotoxicity, for *in vivo* applications the biodistribution and excretion pathways need to be considered as well. Photophysical properties should be adjusted to result in a high overall brightness B according to equation (3). Thus, the 4 factors in the equation need to be optimized efficiently. In addition, the excitation wavelength of the antenna should be >330 nm to reduce damage to living tissues during irradiation and the luminescence lifetime should be maximal to allow time resolved detection.<sup>12</sup>

Due to the chemical similarity of all lanthanides, the applied luminescent center can be chosen from the whole series without significant changes to the synthetic procedure. Nevertheless, the choice of the luminescent center determines the emission wavelength, the excited state lifetime and the overall luminescence intensity. Unfortunately, these parameters

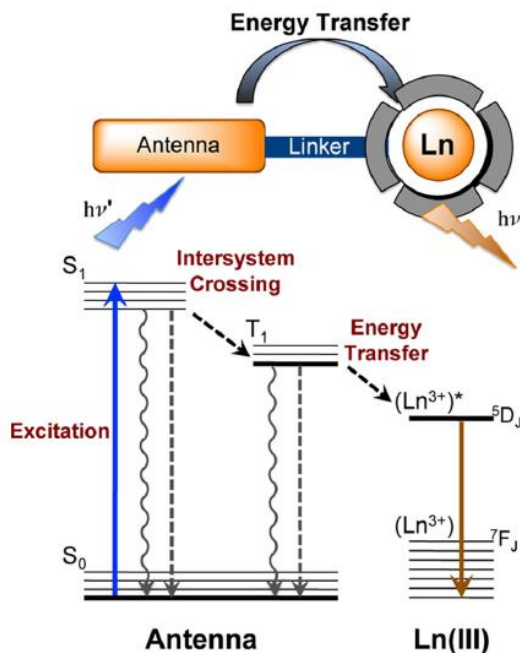


**Figure 1.5.** Schematic illustration of the excitation and emission pathways in a lanthanide complex with an antenna for improved sensitization.<sup>56</sup> 2014 Copyright American Chemical Society.

are not necessarily independent, so that the best compromise needs to be found in respect to the application. For example, Er<sup>3+</sup> is a NIR-emitting lanthanide, which results in large penetration depths (up to 10 cm) due to the low interaction of NIR light with the biological tissues. However, as described above, for a small  $\Delta E$  between excited and ground state, the non-radiative deactivation is more favorable and the intrinsic quantum yield  $\Phi_{Ln}$ , as well as the luminescence lifetime decreases. For most applications, Tb<sup>3+</sup> and Eu<sup>3+</sup>-ions are the lanthanides of choice, as they combine long luminescence lifetimes (up to ms) with strong emissions in the visible range, resulting in a reasonable penetration depth.<sup>53</sup> The most luminescent lanthanide is Gd<sup>3+</sup>, however, due to the emission in the UV range (310 nm) it is not suitable for bioimaging.

Not only the choice of the lanthanide center, but also the ligand has an influence on the observed luminescence intensity. As described above, high energy O-H-vibrations efficiently quench the luminescence of a lanthanide center by non-radiative deactivation. Therefore, the ligand should efficiently avoid direct coordination of water molecules to the lanthanide



center.<sup>8,55</sup> In contrast to the MRI agents, inner sphere water molecules are not favorable for the efficiency of an optical imaging probe. In addition to a low  $q$ -value, the ligand itself should be rigid because vibrations of the N-H and C-H-bonds can also contribute to the quenching of the luminescence. And the last and probably the most important aspect concerning the ligand is the *in vivo* stability against trans-metalation in biological environment. This means that as high as possible thermodynamic stability and kinetic inertness of the complex is required to avoid release of free lanthanide ions and the associated toxicity.<sup>57,58</sup>

As a last part, the antenna should be chosen depending on the type of lanthanide in order to maximize luminescence intensity. This becomes obvious from equation (3) ( $B = \varepsilon\Phi_{Ln}\eta_{ISC}\eta_{ET}$ ) in which  $\varepsilon$ ,  $\eta_{ISC}$  and  $\eta_{ET}$  are mainly dependent on the type of antenna and the position of the energetic levels of  $S_0$ ,  $S_1$  and  $T_1$  in respect to the  $^5D_J$  levels of the  $Ln^{3+}$ -ion. The antenna should have a high  $\varepsilon$  value for the excitation into the  $S_1$ -state (Figure 1.5) to populate the excited state to a significant degree. In addition, the excitation should occur at wavelengths that are not harmful for biological systems ( $\lambda_{exc} > 330$  nm) but on the other hand, the  $S_1$ -state needs to be higher than the  $T_1$ -state for an efficient intersystem crossing, so that the excitation wavelength cannot be too long either. Then again, the  $T_1$ -state should be energetically higher than the Ln-acceptor state ( $^5D_J$ ). The better these energetic levels are adjusted with respect to each other, the higher the luminescence. Generally speaking, each donor level has to be higher than the corresponding acceptor level but sufficiently close for efficient transfers. On the other hand, if the levels are too close, back-transfer can occur by thermal activation, which is unfavorable and reduces the efficiency. Obviously, the defined energy transfer path needs to be favorable over other deactivation pathways, such as fluorescence ( $S_1$ - $S_0$ ) or phosphorescence ( $T_1$ - $S_0$ ) or non-radiative deactivation.<sup>48</sup>

Especially the last energy transfer from the antenna  $T_1$ -state to the lanthanide  $^5D_J$ -state is highly dependent on the distance between the antenna and the lanthanide center.<sup>59</sup> There are two different mechanisms describing this energy transfer. The first one is Förster's mechanism, which is also called dipole-dipole mechanism. The dipole moment of the  $T_1$ -state couples with the dipole moment of the lanthanide 4f orbitals. This mechanism decreases with the 6<sup>th</sup> power of the distance between the donor and acceptor ( $R^{-6}$ , with R being the accdon-distance) and is also involved in Förster-Resonance-Energy-Transfer (FRET) between

an excited luminophore and a second chromophore in close distance. This phenomenon will be discussed further down. The second mechanism is Dexter's mechanism or the exchange mechanism. This mechanism involves a double electron transfer and depends exponentially on the distance of acceptor to donor ( $e^{-R}$ ). Thus, both mechanisms depend highly on the proximity of the antenna to the luminescent center giving a good indication for an optimized design of the luminescent probes.<sup>8,52</sup> Most commonly, the antenna is covalently attached to the chelating ligand (e.g. DOTA or DTPA). To increase the energy transfer efficiency, either a greater number of antennae can be attached to the chelate or the length of the linker can be reduced. The strongest reduction of the linker length is a direct coordination of the antenna directly in the ligand (chelating antenna – see Figure 1.6). These complexes have an increased energy transfer compared to common probes with pending antennae.<sup>60-63</sup>

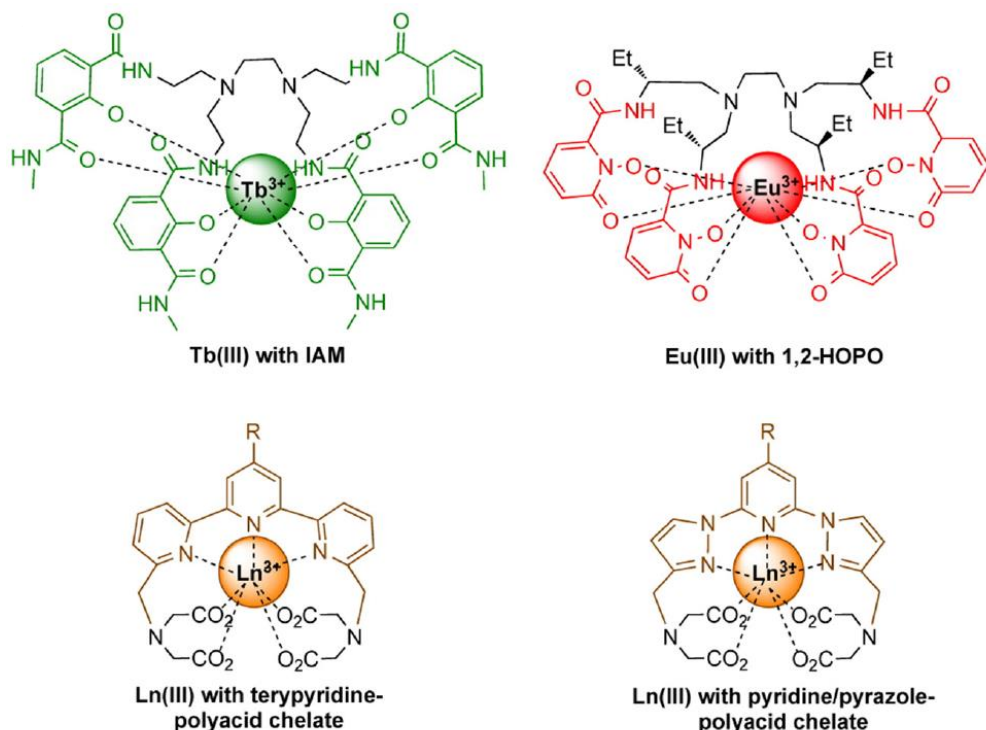


**Figure 1.6.** Examples of recently reported luminescent Ln-complexes with chelating antennae.<sup>56</sup> 2014  
Copyright American Chemical Society.

It is out of the scope of this short summary to describe all applications of lanthanide based optical probes. Multiple comprehensive reviews exist, which summarize the applications and describe the advantages and disadvantages in detail.<sup>8,14,53</sup> However, a short overview of the most common applications with references to more detailed descriptions will be given in the following paragraphs. Due to the above-mentioned options for derivatization and the strong dependence of the luminescence on a number of tunable factors there are different categories of bioimaging agents.

In the first category, targeting groups are covalently connected to the luminescent complex and imaging of biological structures of interest is accomplished by the specific targeting ability of these groups, including e.g., peptides, proteins or nucleic acids. The targeting vectors must present accessible reactive groups and may obviously not lose their activity upon connection to the complexes. The target structures for these types of agents range from cancer cells in small animal imaging to intracellular structures, such as nuclei.

A second category is responsive probes that make use of some of the abovementioned dependencies of the luminescence on specific (and tunable) parameters. These parameters include antenna-lanthanide distance, inner sphere water molecules, change of the antenna by chemical alteration, etc. When any of these parameters change in the presence or absence of the relevant analytes, the luminescence intensity or lifetime of the probe is affected, and this effect can be visualized. Due to the high sensitivity of luminescent probes, the detectable concentrations of the analytes can be very low. Most often, cyclen based agents were designed that specifically and reversibly bind endogenous ions to change the luminescence properties.

In contrast to the aforementioned, lanthanide-centered luminescent probes, the Förster-Resonance-Energy-Transfer (FRET) mechanism can be applied to design another type of analytical probes. Here, the lanthanide center is not directly used as an emitter but rather as a donor for the excitation of another luminophore. For this mechanism to occur, multiple requirements have to be fulfilled. First and most important, the distance of donor and acceptor needs to be short, as the efficiency decreases with the 6<sup>th</sup> power of the distance.<sup>8,52</sup> In addition, the emission spectrum of the donor and the absorption spectrum of the acceptor need to overlap. This mechanism is a non-radiative dipole-dipole mechanism, as already mentioned above and is similar to the antenna-lanthanide energy transfer. As no change in the spins occurs, the transfer is considered a singlet-singlet transfer. This contrasts with the Dexter

mechanism, which occurs at much shorter distances and involves a double electron transfer. The consequence of the FRET-mechanism is a reduction of the luminescence intensity and lifetime of the donor in favor of an acceptor-centered luminescence. Due to the strong dependence on the distance, this type of probe can be used as nano-calipers for the determination of distance changes well below the range that is optically detectable, such as during DNA hybridization and conformational changes or protein interactions and opens a route to investigations of structural changes in biological systems.<sup>64-66</sup>

## **Radioisotopes for medical imaging and therapy**

The use of radioactive compounds in medical applications has a history back to the 1940s, when radioactive iodine was first used in the treatment of adenocarcinoma of the thyroid.<sup>67</sup> However, more developments in the fields of dosimetry, gamma cameras and electronics were necessary to develop reliable and applicable systems for nuclear medicine. Nowadays, the nuclear imaging techniques, such as scintigraphy and especially single photon emission computed tomography (SPECT) and positron emission tomography (PET), are considered important tools in medical diagnosis with a growing number of scans every year. All these imaging techniques require the administration of radioactive tracers in order to detect the radiation that is directly or indirectly emitted by the radioisotopes. Compared to other imaging techniques, radionuclide imaging has the highest sensitivity, which even outperforms optical imaging. In addition, the penetration depth is much larger than for optical imaging. The information gained from nuclear imaging is of mainly metabolic nature because the applied radiotracers are usually radiopharmaceuticals and are therefore metabolically active in order to accumulate at the points of interest. However, no or little anatomic information is gained by these technologies, so that nowadays, PET and SPECT are often combined with X-ray CT (computed tomography) or MRI as these technologies can add the missing anatomical information.<sup>68,69</sup> Where possible, the two imaging modalities are combined in one device to minimize artifacts from movement of the patient. The most common combination is PET/CT; however, it has to be considered that the radiation dose for the patient is increasing significantly due to the CT scan. The main drawbacks of the

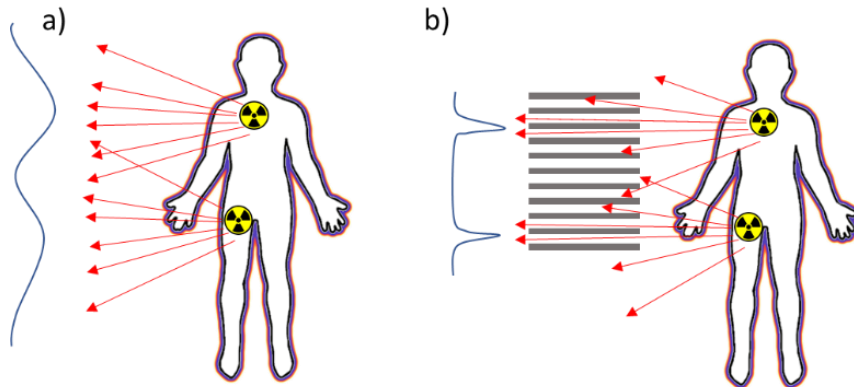


**Figure 1.7:** Collimator principle. Without collimator all emitted photons are detected resulting in low resolution images (a). The collimator absorbs photons that do not travel in the right direction, so that the directional information of the photons is restored and the resolution of the image increases (b).

radionuclide imaging modalities are the use of ionizing radiation, which limits the application to certain patients and diagnoses, as well as the short half-life times of the radiotracers, which increases the demands on logistics of tracers and affects the costs significantly, making PET the most expensive imaging technique at this moment.

Looking at the three imaging modalities mentioned above, it is obvious that scintigraphy is delivering 2D-images, while PET and SPECT are tomographic methods and thus result in 3D-images, displayed as slices along any desired axis of the body. While scintigraphy and SPECT detect  $\gamma$ -rays directly emitted from the tracer, PET is detecting  $\gamma$ -rays that originate from the annihilation of an emitted positron and an electron of the surrounding tissue. These mechanisms result in significant differences of the required imaging systems and consequently in different resolutions, sensitivities and costs. In the following paragraphs these differences will be discussed briefly.

Scintigraphy and SPECT are closely related. The main difference is that scintigraphy is a planar scanning of the patient along one axis and does not consider different angles, while SPECT is taking images from  $360^\circ$  around the patient, converting the individual images into a 3D image. Both systems are equipped with one or more gamma cameras to detect the emitted radiation. In order obtain directional information, the cameras are equipped with collimators. The collimator is filtering  $\gamma$ -photons that are not travelling in the right angle towards the camera (Figure 1.7). This filter significantly increases resolution and is crucial

for successful imaging, however, the number of detectable photons is dramatically reduced by the collimator and the sensitivity is thus decreasing significantly. In the last years, new collimators were developed to reduce this negative effect.<sup>70</sup>

In PET,  $\gamma$ -photons are detected that originate from the annihilation of a positron with an electron. This annihilation process is very characteristic, as it generates two  $\gamma$ -photons with 511 keV energy, which travel in opposite directions. The PET equipment is designed to detect both photons simultaneously and to correlate them. Thus, in the case of PET imaging, no collimator is required because the directional information is given by the detection of the coincidence of photon pairs. The absence of collimators enhances the sensitivity, while the resolution is decent. However, compared to SPECT there is an additional contribution that reduces resolution in PET images. This effect can be found in the pathlength of the positron after emission and before annihilation. Usually, this length is less than 1 mm, however it depends on the emission energy of the positron. It is important to mention that PET equipment, due to the simultaneous 360° detection and the complex electronics is much more expensive than SPECT equipment. In addition, the positron emitting radionuclides usually have shorter half-life times compared to the isotopes that are commonly applied in SPECT imaging (range of minutes compared to hours, respectively (Table 1.1). This short lifetime requires fast inclusion of the radionuclides into the radiopharmaceuticals by either chemical reaction or complexation and fast transport to the examination site in order to retain enough activity for imaging. On the other hand, the short lifetimes of the tracers help to reduce the radiation burden upon administration of the imaging agents to the patient.

The choice of the right radioisotope is influenced by several factors, that significantly determine application range, chemical as well as radiation toxicology, applicability and costs.

**Table 1.1.** Some of the common radionuclides for PET and SPECT imaging.<sup>12</sup>

	Radioisotope	$t_{1/2}$ (min)	Emission type	Energy (MeV)	Typical application
PET	<sup>11</sup> C	20.3 min	$\beta^+$	0.97	Fast metabolic molecules
	<sup>18</sup> F	110 min	$\beta^+$	1.74	Fast metabolic molecules
	<sup>64</sup> Cu	12.7 h	$\beta^+$	0.66	Molecules with slow pharmacokinetics
	<sup>68</sup> Ga	68.1 min	$\beta^+$	1.90	Metal complexes
	<sup>152</sup> Tb	18.5 min			Metal complexes
SPECT	<sup>123</sup> I	13.2 h	$\gamma$	0.16	Functional status of thyroid tissue
	<sup>99m</sup> Tc	6.02 h	$\gamma$	0.14	Macromolecules, liposomes and cells
	<sup>111</sup> In	67.9 h	$\gamma$	0.18	Proteins
	<sup>67</sup> Ga	78.3 h	$\gamma$	0.09 / 0.19	Iron analogue for binding of proteins

The most important ones include the mode of production of the radioisotopes, their half-life times, decay modes and energies of the parent as well as daughter elements.

The mode of production, in combination with the half-life time, is most important for the applicability of a radioisotope in nuclear medicine. Some radioisotopes can be produced in generators in which suitable parent nuclides are immobilized. Upon decay, the daughter nuclides of interest are released and can be eluted for further use. This is the easiest way to generate radionuclides, as it is mobile and does not require sophisticated technology. However, this production mode is limited to elements, which have suitable and long-lived parent nuclides.

Most of the commonly used radionuclides for PET imaging are produced in cyclotrons. This mode of production requires a cyclotron close to the examination location, in order to reduce transportation time. In addition, cyclotrons are expensive equipment and increase the costs for the tracers. Nevertheless, the two most commonly applied PET radionuclides,  $^{11}\text{C}$  and  $^{18}\text{F}$  are produced in cyclotrons by bombarding nitrogen with protons or neon atoms with deuterons, respectively.<sup>71,72</sup> An alternative production strategy for  $^{18}\text{F}$  is the irradiation of  $^{18}\text{O}$ .<sup>73</sup> After production, the radionuclides are incorporated in the radiopharmaceuticals by fast chemical reactions, such as electrophilic and nucleophilic substitutions for methylation and fluorination reactions. This whole process should be finished within a narrow timeframe (3-4 half-lives) to ensure sufficient activity levels.

Compared to the PET tracers, the most commonly used SPECT radionuclide ( $^{99\text{m}}\text{Tc}$ ) can be extracted from a generator containing immobilized  $^{99}\text{MoO}_4^{2-}$ . These generators can easily be shipped and produce high amounts of  $^{99\text{m}}\text{Tc}$  for an extended time (approx. 1 week), due to the long half-life of the parent nuclide  $^{99}\text{Mo}$  (approx. 66 h). Technetium in contrast to the above-mentioned elements is not covalently connected to radiopharmaceuticals but can be complexed with suitable ligands. However, before complexation, the  $^{99\text{m}}\text{TcO}_4^{2-}$  needs to be reduced to  $^{99\text{m}}\text{Tc}^{4+}$ . Nevertheless, the comparably simple logistics and the lower costs, in combination with a wide applicability and easy handling make this radionuclide the first choice. With its assistance many millions of scintigraphy and SPECT scans are performed annually, making this nuclide the most commonly applied nuclear imaging agent in the world. Therefore, the annual demand of  $^{99\text{m}}\text{Tc}$  and consequently  $^{99}\text{Mo}$ , as the parent nuclide, is high and a stable supply has to be assured, due to the half-life of only 66 h for  $^{99}\text{Mo}$ .

Multiple ways of production are discussed, however, up to now, only the neutron induced fission of  $^{235}\text{U}$  in nuclear reactors is able to satisfy the high demands.<sup>74</sup>

All the above discussed radionuclides are well suitable for nuclear imaging with different advantages and limitations, however, due to the short half-lives and the comparably low radiation energies, they cannot be applied for therapy. This is, where radioisotopes of lanthanides can show significant advantages. Radioisotopes of lanthanides that are relevant for medical imaging are summarized in Table 1.2. The decay mode suggests that several of them are also relevant for therapy, as they either decay by  $\alpha$  or  $\beta^-$  decay, in addition to the decay mode relevant for imaging ( $\gamma$  or  $\beta^+$ ). Moreover, most half-life times are significantly longer than the ones for the abovementioned radionuclides.

Obviously, the earlier described characteristics of the lanthanides apply equally for radioisotopes, and therefore, the chemical properties are nearly the same for all the radioisotopes, including the trivalent binding and the complexation behavior. Thus, it is a simple exercise to exchange one element for another, and herewith, introduce different nuclear properties. In addition, as described in the sections above, lanthanides can be used for other imaging modalities as well, so that there might be options to combine two imaging modalities in one agent.<sup>75</sup> The use of lanthanides in multimodal imaging will be discussed further down in this introduction.

A promising candidate for a combined imaging and therapy was found in  $^{177}\text{Lu}$ . For the imaging and treatment of neuroendocrine tumors, the radionuclide was complexed in DOTA-Tyr3-Octreotate, where the peptide acts as a targeting vector.<sup>76</sup>  $^{177}\text{Lu}$  has a half-life time of 6.7 d, which is much longer than the commonly used PET and SPECT tracers and it has a

**Table 1.2.** Physical characteristics of radio-lanthanides applied for nuclear imaging and therapy.<sup>12</sup>

Isotope	$t_{1/2}$	Decay	$E_\alpha$ (MeV)	$E_\beta$ (MeV)	$E_\gamma$ (keV)	Application
$^{177}\text{Lu}$	6.7 h	$\gamma, \beta^-$		0.13	113, 208	SPECT, therapy
$^{149}\text{Tb}$	4.1 h	$\alpha, \beta^+$	3.97	0.73	165, 352, 389, 652	PET, therapy
$^{152}\text{Tb}$	17.5 h	$\gamma, \beta^+$		1.08	271, 344, 586, 789	PET
$^{155}\text{Tb}$	5.3 d	$\gamma, \text{EC}$			87, 105, 180, 262	SPECT
$^{161}\text{Tb}$	6.9 d	$\gamma, \beta^-$		0.15	49	SPECT, therapy
$^{167}\text{Tm}$	9.3 d	$\gamma, \text{EC}$			208	SPECT
$^{169}\text{Yb}$	32.0 d	$\gamma, \text{EC}$			93	SPECT, therapy
$^{141}\text{Ce}$	32.5 d	$\gamma, \beta^-$		0.43, 0.58	145	SPECT, therapy
$^{134}\text{La}$	6.4 m	$\gamma, \beta^+$		0.76	605	PET
$^{153}\text{Sm}$	46.3 h	$\gamma, \beta^-$		0.71	103	SPECT, therapy
$^{157}\text{Dy}$	8.1 h	$\gamma$			326	SPECT
$^{147}\text{Gd}$	1.6 d	$\gamma, \text{EC}$			229	SPECT
$^{166}\text{Ho}$	26.8 h	$\gamma, \beta^-$		0.71	81	SPECT, therapy



$\beta$ -decay that can be utilized for therapy. In addition, the long half-life is favorable for pharmacokinetic studies and helps to gain knowledge on the faith of the therapeutic agents. This was also shown to be advantageous for dosimetric evaluations when compared to “silent” radiotherapeutics, where only theoretical calculations can be used to determine the safe radiation dose. Currently,  $^{177}\text{Lu}$  can only be produced in nuclear reactors and there are only a few that provide the material to hospitals, so that the supply is not optimal. New production routes are currently investigated in order to optimize the availability of  $^{177}\text{Lu}$  for medical applications.

Terbium is another interesting lanthanide for nuclear imaging. It has multiple radioisotopes (see Table 1.2) with different application fields, from SPECT and PET imaging to therapy. In this respect,  $^{149}\text{Tb}$  is currently in the focus as an alternative to other  $\alpha$ -emitting therapeutics. It is especially interesting due to the unique combination with  $\beta^+$ -emission, which allows for PET imaging.  $^{149}\text{Tb}$  does not have any  $\alpha$ -emitting daughters, so that there is no risk of uncontrolled  $\alpha$ -emission from the daughter nuclides, which is an additional benefit. The other relevant isotopes of Tb ( $^{152}\text{Tb}$ ,  $^{155}\text{Tb}$ ,  $^{161}\text{Tb}$ ) also show interesting properties. While  $^{152}\text{Tb}$  and  $^{155}\text{Tb}$  can be applied for imaging purposes only,  $^{161}\text{Tb}$ , which can be produced by neutron bombardment of enriched  $^{160}\text{Gd}$  targets, was proposed as an alternative for  $^{177}\text{Lu}$  for combined imaging and therapeutic applications.<sup>77</sup> Although both,  $^{177}\text{Lu}$  and  $^{161}\text{Tb}$  have similar half-lives and comparable  $\beta$ -energies, the Tb isotope has proven more efficient in tumor treatment, compared to Lu. This is attributed to the largely increased number of Auger electrons that are emitted during the  $^{161}\text{Tb}$  decay. Auger electrons induce short-range damage to the surrounding tissue, efficiently dealing lethal damage to the cell by

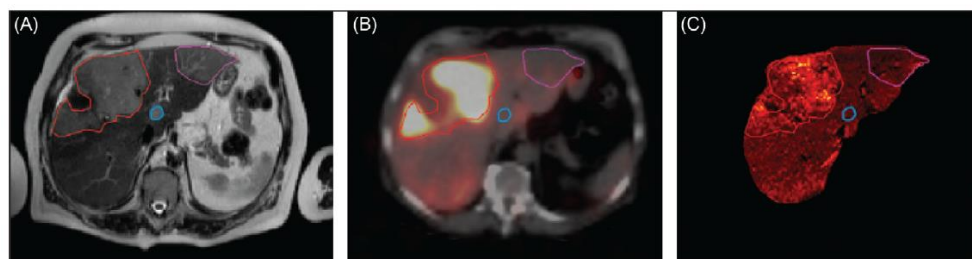


**Figure 1.8.** (A) Multimodal imaging of liver metastases: T2-weighted image of several liver metastases (outlined); (B) Distribution of  $^{166}\text{Ho}$ -poly(L-lactic acid) microspheres after radioembolization as detected by SPECT-CT (C) and detected by T2\*-weighted MRI.<sup>80</sup> 2012 Copyright Elsevier.

e.g., double stranded DNA break. The advantage of the chemical similarity was proven in studies, where radiolabeling of DOTA-decorated antibodies was performed under identical conditions for Lu and Tb and resulted in comparable high specific activities.<sup>78,79</sup>

Due to the high magnetic moment and the  $\gamma$ -emission,  $^{166}\text{Ho}$  is a suitable candidate for the combination of MRI with gamma imaging (scintigraphy or SPECT). The  $\beta$ -decay is suitable for therapeutic applications, so that this radionuclide is interesting for multimodal imaging in combination with therapy.  $^{166}\text{Ho}$  can be produced from  $^{165}\text{Ho}$  by neutron activation in a nuclear reactor. An advantage of this rather soft activation method is that organic functions can survive the activation, as it was shown on the example of PEGylated Ho-containing nanoparticles.<sup>81</sup> It was shown that particles, containing activated Ho can be used for radioembolization of unresectable liver tumors. In this application the direct combination of imaging and therapy is of high value, because the administered radiation dose at each individual location can be determined with MRI or  $\gamma$ -camera, as can be seen from Figure 1.8.<sup>82,83</sup>

While administration of radioactive lanthanide tracers and therapeutics into the body (internal radiotherapy) is still in developing stage, application of external ionizing radiation (e.g., X-rays,  $\gamma$ -rays or proton beams) to treat diseased tissues is the currently applied in the clinics (external radiotherapy). At borderline of internal and external radiotherapy, there is neutron capture therapy (NCT), which involves the delivery of non-radioactive material to the tissue of interest, followed by its irradiation with a neutron beam to produce the radiotherapeutics *in vivo*. This application relies on materials with large neutron capture cross sections, compared to the elements that are commonly present in biological tissues. Commonly used NCT agents are  $^{10}\text{B}$  containing compounds, such as borates.<sup>84</sup> The success of the treatment is highly dependent on the accumulation of the agents in the diseased tissue. Therefore, the boron-containing moieties are often connected to specific targeting vectors. Nevertheless, the uptake in the region of interest cannot be monitored with boron because there is no medical imaging modality that can detect it. Therefore, some agents were additionally equipped with Gd-DOTA moieties in order to track them with MRI.<sup>85,86</sup> This strategy allows for quantification of boron deposition at the site of interest and consequently a personalized determination of the radiation flux and time to ensure the best outcome of the treatment with minimal side effects. In addition, two isotopes of Gd have large neutron capture cross sections themselves, with  $^{157}\text{Gd}$  having the largest one of all stable isotopes (255000 barn, which is

65 times more than  $^{10}\text{B}$ ).<sup>87</sup> The formed  $^{158}\text{Gd}^*$  emits internal conversion electrons, Auger electrons and characteristic X-rays. This emission portfolio is not the most suitable for NCT, as the emitted X- or  $\gamma$ -rays have a large pathlength in tissue and do not deposit the energy locally at the point of interest. On the other hand, Auger electrons have an extremely short pathlength, so that the emitting Gd center needs to be located close to vital parts of the cell (DNA, mitochondria etc.) in order to cause lethal damage. In contrast,  $^{10}\text{B}$  undergoes nuclear fission after neutron capture and releases an  $\alpha$ -particle and a recoiling Li atom (Figure 1.9). Both particles have a pathlength which is in the range of a cell diameter, so that the energy deposition is local but an accurate location of boron directly at the vital organelles is not required. The advantage of  $^{10}\text{B}$  in therapeutic behavior overcompensates the lower neutron capture cross section, so that target concentrations for  $^{10}\text{B}$  are 10-30  $\mu\text{g}$  per g of tumor mass, while  $^{157}\text{Gd}$  has a 50-200  $\mu\text{g}$  per g target range for successful NCT.<sup>88</sup> However, it has to be mentioned that the atomic mass of Gd is more than 15 times larger than that of boron, so that the absolute numbers in moles are still lower for Gd. Currently, NCT is not a widely applied therapeutic approach, despite the interesting possibilities and the increased safety that it offers. This is mainly due to the suboptimal design of the NCT agents and the need to accumulate sufficient amounts in the desired location with high tissue to blood ratios. Further research in this respect will probably open doors for further applications of lanthanides in NCT agents.

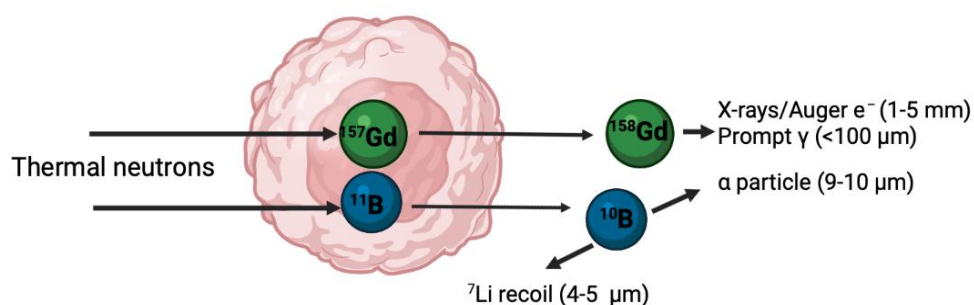


**Figure 1.9.** Schematic representation of the neutron capture reaction for boron and gadolinium nuclei, accumulated in tumor tissue during neutron capture therapy.

## Concerns on the toxicity of lanthanide-based agents

In the early 1960, when the industrial application of lanthanides increased due to the availability of pure and comparably cheap lanthanides, the first concerns were raised in respect to their safety and toxicity. Although, medical applications of lanthanides were not even close to realization at that time, detailed animal studies were conducted to determine toxicological parameters ( $LD_{50}$  values) of different lanthanide salts and different administration routes.<sup>89</sup> From these studies, it became evident that any intravenous administration of free lanthanide ions is connected to a severe toxicology.  $LD_{50}$  values of lanthanides are typically  $<0.2 \text{ mmol kg}^{-1}$ , which is around the same concentration of  $Gd^{3+}$  that is typically administered for a standard contrast-enhanced MRI scan ( $0.1 - 0.3 \text{ mmol kg}^{-1}$ ). As the other imaging modalities are much more sensitive towards the applied contrast agents and thus the applied concentrations are orders of magnitude lower, the toxicity issue nowadays is most prominent and best investigated for MRI contrast agents.

Free lanthanide ions *in vivo* are mainly deposited in the bones, liver and lymphatic system, where they are retained for an extended time and can cause serious long-term effects.<sup>57,90,91</sup> In addition, lanthanide ions can substitute bivalent metal centers in proteins and enzymes, rendering them inactive and thus affecting biochemical processes all over the organism.

In contrast agents for MRI, the paramagnetic lanthanide ions (mainly  $Gd^{3+}$ ) are confined by chelating ligands, in order to reduce the interaction of the ions with the biological environment. Several ligands were proposed, showing high kinetic and thermodynamic stability of the resulting complexes to avoid leaching of free lanthanide ions and transmetalation by endogenous metal ions.<sup>92</sup> From the introduction of the first MRI contrast agents until 2006, these complexes had a reputation to be absolutely safe. However, in 2006, the occurrence of a serious illness, called nephrogenic systemic fibrosis (NSF) was attributed to the application of Gd-DTPA-bisamide (Omniscan<sup>®</sup>) in patients with impaired renal function.<sup>57,89</sup> It showed that this illness is caused by an accumulation of free gadolinium ions over a long time, but the exact mechanism is still not understood. In addition, other contrast agents, such as Gd-DOTA (Dotarem<sup>®</sup>) did not show this phenomenon due to higher kinetic inertness of the complex.

Starting from 2014, other incidents came to light that were attributed to complexes of linear chelates (DTPA-type ligands) in Gd-containing MRI contrast agents. It was found that these compounds accumulate in the brain of patients, even if they did not display any impairment of their renal function.<sup>17,91</sup> The presence of Gd in the brain was confirmed by a significant brightening of the globi pallidi and dentate nuclei in MRI brain scans as well as by mass spectrometry. This issue caused serious concerns in respect to the linear chelates and intensive investigations were started, which resulted in a position paper of the European Medicines Agency (EMA), which was published on November 23<sup>rd</sup>, 2017 under reference EMA/625317/2017 and led to the suspension of most linear MRI contrast agents. The individual agents that were investigated are summarized in Table 1.3. However, in the document, the EMA also stressed, that the found accumulation of Gd in the brain was so far never attributed to any neurological or other adverse effects.

In general, there were several 100 million contrast enhanced MRI scans performed over the last 30 years, of which only 0.03% gave rise to severe adverse effects. Considering these numbers, lanthanide-based MRI contrast agents can still be considered safe and the risk-benefit-ratio is favorable in many cases. Nevertheless, the recent observations and concerns show, that the stability of the complexes along with a fast excretion are of highest importance for the safety of lanthanide-containing agents for medical imaging. The current understanding is, that DOTA-analogues are the most stable and thus safest complexes.

**Table 1.3.** Recommendations of the EMA for the different types of contrast agents as published in EMA/625317/2017.

Product	Type (formulation)	Recommendation
Artirem / Dotarem ( <i>gadoteric acid</i> )	macrocyclic (i.v.)	maintain
Artirem / Dotarem ( <i>gadoteric acid</i> )	macrocyclic (intra-articular)	maintain
Gadovist ( <i>gadobutrol</i> )	macrocyclic (i.v.)	maintain
Magnevist ( <i>gadopentetic acid</i> )	linear (intra-articular)	maintain
Magnevist ( <i>gadopentetic acid</i> )	linear (i.v.)	suspend
Multihance ( <i>gadobenic acid</i> )	linear (i.v.)	restrict use to liver scans
Omniscan ( <i>gadodiamide</i> )	linear (i.v.)	suspend
Optimark ( <i>gadoversetamide</i> )	linear (i.v.)	suspend
Primovist ( <i>gadoxetic acid</i> )	linear (i.v.)	maintain
Prohance ( <i>gadoteridol</i> )	macrocyclic (i.v.)	maintain

## Recent developments and Outlook

Clinically applied lanthanide-containing contrast agents for MRI are often composed of small complexes, such as Gd-DOTA for magnetic resonance imaging. However, to further increase the performance, even towards molecular imaging, which is defined as *in vivo* characterization/measurement of events at a (sub)cellular level,<sup>49,93</sup> larger compounds with a higher payload of lanthanide ions seem attractive, as the contribution of each ion sums up to an extremely high overall performance per compound. For this reason, lanthanide containing nanoparticulate systems are increasingly interesting for scientists all over the world and a wide variety of different nanosystems were published in scientific literature in the last decade. The nature of the particles ranges from organic to inorganic and from porous to solid particles of different shapes and sizes.<sup>94-97</sup>

The simplest synthetic strategy is the connection of small molecules to the surface of a carrier, in order to increase the number of lanthanide centers per unit. However, this strategy often involves significant efforts and does not necessarily contribute to the performance of the individual lanthanide ion. Therefore, several smart particle designs were described, that combine high lanthanide payloads with the increased performance due to the special characteristics of particulate systems.

In MRI, it is obvious to design  $T_2$  contrast agents as paramagnetic nanoparticles, due to the strong magnetization that they experience in external magnetic fields. With high lanthanide concentrations, especially when Ho or Dy with their high magnetic moments are used, these particles show extremely high  $r_2$ -values that do not saturate up to very high external magnetic field strength (above 20 T).<sup>7</sup> The  $r_2/r_1$ -ratios are very high, making these materials suitable for  $T_2$ -weighted imaging. However, there are particulate systems in MRI that have a significant effect on  $T_1$ , thus show a significant  $r_1$ . For this purpose, polymeric particles or porous materials with a fast water exchange from the inside of the particle to the bulk are interesting candidates. In case the  $r_2/r_1$ -ratio is in the range of 1-10, the materials can even serve as bimodal  $T_1/T_2$  contrast agents, which are applicable for both imaging principles. Relaxivities can be optimized by adjusting particle size, shape and composition but in addition the target magnetic field ( $B_0$ ) has to be considered. This is important for the  $r_2/r_1$ -ratio, because  $r_1$  and  $r_2$  are developing in different directions with increasing magnetic field, shifting the ratio towards higher values. Prominent examples are Gd-loaded zeolites, which

show a  $r_2/r_1$ -ratio of approx. 3 at 7.5 T, 25 °C and a pH dependence that even makes these materials responsive agents.<sup>98</sup> However, also silica particles and hydrogels were reported for the encapsulation of Gd-complexes to obtain bimodal  $T_1/T_2$  contrast agents.<sup>99,100</sup>

Next to the pure accumulation of properties that small complexes or ions already show, the inclusion of lanthanides in particulate systems can even induce additional properties, that cannot be exploited in small molecule compounds. This becomes evident when luminescent lanthanide probes are considered. While small luminescent lanthanide complexes consist of distinct parts with individual function (lanthanide ion, chelate, antenna - for details see above), luminescent lanthanide-containing nanoparticles are typically host/guest-particles of other elements that are doped with luminescent lanthanide ions, most commonly Eu and Tb for visual light emission. However, other lanthanides can be used to change the emission spectrum as needed for the intended application. Multiple synthetic routes towards lanthanide doped nanoparticles are discussed and the obtained materials display interesting properties, including high quantum yields, even without the presence of an antenna, which is required in luminescent complexes. Especially interesting for medical imaging are particles that show upconversion luminescence, meaning that long wavelengths can be used to sensitize the lanthanide centered luminescence. Because of the option to use low energy visible or near IR light, the excitation with UV light can be avoided and the damage to the tissue is significantly reduced. In addition, the penetration depth of these types of light is much longer than for UV light, so that deeper regions of interest can be reached.<sup>101-103</sup>

Luminescent nanoparticles display interesting properties for optical imaging and again, the option to design dual imaging probes is at hands. This goal can be achieved by simply grafting other reporter units (such as Gd-DOTA units) to the surface of the particles or by introducing magnetic or radioactive elements into the particle's interior. Again, zeolite systems show interesting MRI/optical bimodal properties. But also, solid and mesoporous  $Gd_2O_3$ -particles, doped with Eu were proposed as dual MRI-optical probes.<sup>42</sup>

Next to these interesting options in designing dual or even multimodal imaging probes, particulate probes also show superior *in vivo* behavior. Since tumor tissue is growing fast, the blood vessels are often not as well developed as in healthy tissue. This leads to the possibility that particles can escape from the bloodstream and extravasate into the surrounding tissue, where they are retained and tend to accumulate. This phenomenon is known as the enhanced permeability and retention (EPR) effect and can be considered a

passive targeting of particles towards tumors with leaky vasculature.<sup>104</sup> To further enhance the specificity, the surface of particles can be decorated with functional groups. Especially, targeting vectors are important to optimize the biodistribution. With this active targeting, particles are selectively delivered to the site of interest and even the uptake into cells can be improved. One prominent example for a targeting vector is the cyclic peptide c(RGDyK), which selectively targets  $\alpha_v\beta_3$  integrin receptors and subsequently leads to internalization into the cell.<sup>105</sup> As the receptors are overexpressed on many tumor cells, this targeting vector can be used in tumor imaging. With this increased specificity, particulate imaging probes open the doors for molecular imaging due to the high payloads of lanthanide ions that can selectively be delivered to the site of interest.

Next to the opportunity to elegantly combine different imaging modalities in one probe, lanthanides offer the option to combine imaging and therapy, as was already briefly described in the section on radioisotopes. This combination of diagnostic and therapeutic properties is often referred to as theranostics.<sup>106</sup> The concept of theranostic agents is not defined further and can thus combine small molecule compounds as well as particulate systems with different reporter units as well as therapeutic approaches ranging from chemotherapy and gene therapy to hyperthermia and photodynamic therapy and as described earlier, ionizing radiation can be used for therapy as well. But all theranostic agents display the same superior properties that separate imaging agents and therapeutic drugs cannot match. The most important one is the direct feedback on delivered doses of therapeutics to the site of interest. This can help to better estimate the right doses and to personalize the treatment, based on the response given by the imaging part and consequently improve the result of the therapy.

## **Summary**

The versatile properties of lanthanides and their current applications in medical imaging are described in this introduction. In summary, lanthanides show interesting properties for several medical imaging techniques and offer additional benefits compared to other possible elements, especially in the combination of two or more imaging modalities in small complexes as well as nanoparticulate systems and in the field of theranostic applications. The chemical similarity of all lanthanides makes them easily exchangeable in synthetic



procedures without affecting the results and yields. In addition, the exchange of one lanthanide for another one in an imaging probe, does not significantly modify the *in vivo* characteristics.

Nevertheless, the described concerns on toxicity due to brain deposition and long-term effects are serious and further research needs to be performed in order to make lanthanide containing agents as safe as possible. For this purpose, multiple aspects must be considered. The biodistribution and residence time *in vivo* need to be optimized, as well as the stability of the compounds against leaching of free lanthanide ions. More improvements of the efficiency by a smarter design of the probes and a better understanding of the parameters governing the efficiency will further reduce the applied doses. Many interesting approaches were proposed to overcome these issues; however, they were not introduced in clinical applications so far.

## Outline of the thesis

This thesis is dedicated to the exploration of the versatility of lanthanides in systems ranging from small-molecular complexes (chapters 2 and 3) to nanoconstructs (chapters 4 and 5) designed for medical applications.

Understanding of molecular dynamics in the Ln-complexes forms an important research line towards design of contrast agents for MRI. Therefore, the aspects of rotation of carboxylic groups involved in the chelating of lanthanides in DOTA-complexes were investigated in chapter 2. The data of the  $^{17}\text{O}$ -NMR measurements was compared with the DFT calculations. The trend found along the lanthanide series leads to a better understanding of the dynamics of DOTA-complexes and their impact on the stability and performance for contrast enhancement in MRI.

In the following chapter, the Tb-DOTA-complexes were investigated on their applicability for the optical imaging after conjugation to the calix[4]arene platforms, which additionally served as antennae for the sensitization of the lanthanide ions. The final optical performance appeared to be determined by the micelle formation due to the differences in polarity of the upper and lower rims of the DOTA-decorated calix[4]arenes. This work is a continuation of the research that was previously performed in the group, where calix[4]arenes

were used as platforms for paramagnetic Gd-DOTA units.<sup>104-106</sup> The current findings, described in chapter 3, give insight into the potential of calix[4]arenes to serve as building blocks for combined MRI/optical imaging probes.

The multimodality approach was further implemented using nanozeolite LTL, where another luminescent lanthanide Eu was used in combination with paramagnetic Gd to design an MRI/optical imaging probe (chapter 4). An advantageous structural feature of porous LTL-nanoparticles is the presence of big and small cavities in the aluminosilicate framework that can be used for the incorporation of lanthanides by a simple ion-exchange procedure. Loading of luminescent Eu-ions into the small cages and paramagnetic Gd-ions in the large channels has resulted in a dual imaging probe. Thereby, the access of water to the lanthanide-ions is the key principle: in the small cages, the entry of water is excluded, which is favorable for the luminescence to occur, while in the big cages, the vast water-exchange results in an exceptionally high longitudinal relaxivity. At a later stage, a closer investigation of the mechanisms governing the relaxivity of Gd-loaded LTL revealed a prototropic water-exchange being responsible for the vast water-exchange as well as the pH responsiveness of the system.<sup>107</sup>

Besides the multimodal options, nanosystems offer the solution to the low-sensitivity issues by delivering high-payloads to the site of interest. From this point of view, solid lanthanide nanoparticles are even more interesting than porous nanomaterials. However, for *in vivo* applications the quality requirements are high. This implies the need for synthetic procedures leading to an easy access to well-defined uniform nanoparticles. A novel, microwave-assisted, synthetic procedure for solid, spherical lanthanide nanoparticles is presented in chapter 5.

## References

1. Kumari, A.; Panda, R.; Jha, M.; Kumar, J.; Lee, J. *Miner. Eng.* **2015**, 79.
2. von Welsbach, C. A. *Justus Liebigs Ann. Chem.* **1907**, 351, (1-3), 458-466.
3. Mosander, C. G. *J. Prak. Chem.* **1843**, 30, (1), 276-292.
4. v. Welsbach, C. A. *Monatsh. Chem. Verw. Teile Anderer Wiss.* **1885**, 6, (1), 477-491.
5. Shannon, R. *Acta Cryst. Section A* **1976**, 32, (5), 751-767.
6. Peters, J. A.; Djanashvili, K.; Geraldès, C. F. G. C.; Platas-Iglesias, C. *Coord. Chem. Rev.* **2020**, 406, 213146.
7. Norek, M.; Peters, J. A. *Prog. Nucl. Magn. Reson. Spectrosc.* **2011**, 59, (1), 64-82.
8. Bünzli, J.-C. G. *Chem. Rev.* **2010**, 110, (5), 2729-2755.
9. Bünzli, J.-C. G. *Coord. Chem. Rev.* **2015**, 293-294, 19-47.
10. Kim, E.; Osseo-Asare, K. *Hydrometallurgy* **2012**, 113-114, 67-78.
11. Bottrill, M.; Kwok, L.; Long, N. J. *Chem. Soc. Rev.* **2006**, 35, (6), 557-571.
12. Peters, J. A.; Djanashvili, K.; Geraldès, C. F. G. C., 8.13 - Imaging With Lanthanides. In *Comprehensive Supramolecular Chemistry II*, Atwood, J. L., Ed. Elsevier: Oxford, 2017; pp 261-293.
13. Teo, R. D.; Termini, J.; Gray, H. B. *J. Med. Chem.* **2016**, 59, (13), 6012-6024.
14. Bünzli, J.-C. G. *J. Lumín.* **2016**, 170, 866-878.
15. Caravan, P.; Ellison, J. J.; McMurry, T. J.; Lauffer, R. B. *Chem. Rev.* **1999**, 99, (9), 2293-2352.
16. Runge, V. M.; Ai, T.; Hao, D.; Hu, X. *Invest. Radiol.* **2011**, 46, (12).
17. Guo, B. J.; Yang, Z. L.; Zhang, L. J. *Front. Mol. Neurosci.* **2018**, 11, (335).
18. Geraldès, C. F.; Laurent, S., *Contr. Med. Mol. Imag.* **2009**, 4 (1), 1-23.
19. Delangre, S.; Vuong, Q. L.; Po, C.; Gallez, B.; Gossuin, Y. *J. Magn. Res.* **2016**, 265, 99-107.
20. Vonken, E.-j. P. A.; Schär, M.; Yu, J.; Bakker, C. J. G.; Stuber, M. *J. Magn. Res. Imaging*, **2013**, 38, (2), 344-357.
21. Merbach, A. E.; Helm, L.; Tóth, É., *The Chemistry of Contrast Agents in Medical Magnetic Resonance Imaging*. 2nd Edition ed.; John Wiley & Sons, Ltd: 2013.
22. Helm, L. *Prog. Nucl. Magn. Reson. Spectrosc.* **2006**, 49, (1), 45-64.
23. Aime, S.; Calabi, L.; Cavallotti, C.; Gianolio, E.; Giovenzana, G. B.; Losi, P.; Maiocchi, A.; Palmisano, G.; Sisti, M. *Inorg. Chem.* **2004**, 43, (24), 7588-7590.
24. Baranyai, Z.; Uggeri, F.; Giovenzana, G. B.; Bényei, A.; Brücher, E.; Aime, S. *Chem. Eur. J.* **2009**, 15, (7), 1696-1705.
25. Balogh, E.; Mato-Iglesias, M.; Platas-Iglesias, C.; Tóth, É.; Djanashvili, K.; Peters, J. A.; de Blas, A.; Rodríguez-Blas, T. *Inorg. Chem.* **2006**, 45, (21), 8719-8728.
26. Aime, S.; Botta, M.; Fasano, M.; Terreno, E. *Acc. Chem. Res.* **1999**, 32, (11), 941-949.
27. Laurent, S.; Vander Elst, L.; Botteman, F.; Muller, R. N. *Eur. J. Inorg. Chem.* **2008**, 2008, (28), 4369-4379.
28. Xue, S.; Qiao, J.; Jiang, J.; Hubbard, K.; White, N.; Wei, L.; Li, S.; Liu, Z.-R.; Yang, J. *J. Med. Res. Rev.* **2014**, 34, (5), 1070-1099.
29. Granato, L.; Laurent, S.; Vander Elst, L.; Djanashvili, K.; Peters, J. A.; Muller, R. N. *Contrast Media & Molecular Imaging* **2011**, 6, (6), 482-491.

30. Helm, L. *Future Med. Chem.* **2010**, 2, (3), 385-96.
31. Caravan, P.; Farrar, C. T.; Frullano, L.; Uppal, R. *Contrast Med. Mol. Imaging* **2009**, 4, (2), 89-100.
32. McMurry, T. J.; Parmelee, D. J.; Sajiki, H.; Scott, D. M.; Ouellet, H. S.; Walovitch, R. C.; Tyeklár, Z.; Dumas, S.; Bernard, P.; Nadler, S.; Midelfort, K.; Greenfield, M.; Troughton, J.; Lauffer, R. B. *J. Med. Chem.* **2002**, 45, (16), 3465-3474.
33. Botta, M. *Eur. J. Inorg. Chem.* **2000**, 2000, (3), 399-407.
34. Elhabiri, M.; Abada, S.; Sy, M.; Nonat, A.; Choquet, P.; Esteban-Gómez, D.; Cassino, C.; Platas-Iglesias, C.; Botta, M.; Charbonnière, L. *J. Chem. Eur. J.* **2015**, 21, (17), 6535-6546.
35. Fulton, D. A.; Elemento, E. M.; Aime, S.; Chaabane, L.; Botta, M.; Parker, D. *Chem. Commun.* **2006**, (10), 1064-1066.
36. Hu, F.; Zhao, Y. S. *Nanoscale* **2012**, 4, (20), 6235-6243.
37. Shin, T.-H.; Choi, J.-s.; Yun, S.; Kim, I.-S.; Song, H.-T.; Kim, Y.; Park, K. I.; Cheon, J. *ACS Nano* **2014**, 8, (4), 3393-3401.
38. Zhang, W.; Martinelli, J.; Mayer, F.; Bonnet, C. S.; Szeremeta, F.; Djanashvili, K. *RSC Advances* **2015**, 5, (85), 69861-69869.
39. Bridot, J.-L.; Faure, A.-C.; Laurent, S.; Rivière, C.; Billotey, C.; Hiba, B.; Janier, M.; Jossierand, V.; Coll, J.-L.; Vander Elst, L.; Muller, R.; Roux, S.; Perriat, P.; Tillement, O. *J. Am. Chem. Soc.* **2007**, 129, (16), 5076-5084.
40. Evanics, F.; Diamente, P. R.; van Veggel, F. C. J. M.; Stanisz, G. J.; Prosser, R. S. *Chem. Mater.* **2006**, 18, (10), 2499-2505.
41. Jin, X.; Fang, F.; Liu, J.; Jiang, C.; Han, X.; Song, Z.; Chen, J.; Sun, G.; Lei, H.; Lu, L. *Nanoscale* **2015**, 7, (38), 15680-15688.
42. Osseni, S. A.; Lechevallier, S.; Verelst, M.; Perriat, P.; Dexpert-Ghys, J.; Neumeyer, D.; Garcia, R.; Mayer, F.; Djanashvili, K.; Peters, J. A.; Magdeleine, E.; Gros-Dagnac, H.; Celsis, P.; Mauricot, R. *Nanoscale* **2014**, 6, (1), 555-564.
43. Hifumi, H.; Yamaoka, S.; Tanimoto, A.; Citterio, D.; Suzuki, K. *J. Am. Chem. Soc.* **2006**, 128, (47), 15090-15091.
44. Frangville, C.; Gallois, M.; Li, Y.; Nguyen, H. H.; Lauth-de Viguerie, N.; Talham, D. R.; Mingotaud, C.; Marty, J.-D. *Nanoscale* **2016**, 8, (7), 4252-4259.
45. Norek, M.; Kampert, E.; Zeitler, U.; Peters, J. A. *Journal of the American Chemical Society* **2008**, 130, (15), 5335-5340.
46. Vuong, Q. L.; Van Doorslaer, S.; Bridot, J.-L.; Argante, C.; Alejandro, G.; Hermann, R.; Disch, S.; Mattea, C.; Stapf, S.; Gossuin, Y. *Magn. Reson. Mater. Phys., Biol. Med.* **2012**, 25, (6), 467-478.
47. Heffern, M. C.; Matosziuk, L. M.; Meade, T. J. *Chem. Rev.* **2014**, 114, (8), 4496-4539.
48. Montgomery, C. P.; Murray, B. S.; New, E. J.; Pal, R.; Parker, D. *Acc. Chem. Res.* **2009**, 42, (7), 925-937.
49. Weissleder, R.; Ntziachristos, V. *Nature Medicine* **2003**, 9, (1), 123-128.
50. Chow, C. Y.; Eliseeva, S. V.; Trivedi, E. R.; Nguyen, T. N.; Kampf, J. W.; Petoud, S.; Pecoraro, V. L. *J. Am. Chem. Soc.* **2016**, 138, (15), 5100-5109.
51. Bünzli, J.-C. G. *Acc. Chem. Res.* **2006**, 39, (1), 53-61.
52. Bünzli, J.-C. G.; Piguet, C. *Chem. Soc. Rev.* **2005**, 34, (12), 1048-1077.
53. Eliseeva, S. V.; Bünzli, J.-C. G. *Chem. Soc. Rev.* **2010**, 39, (1), 189-227.
54. Weissman, S. I. *The Journal of Chemical Physics* **1942**, 10, (4), 214-217.

55. Parker, D.; Williams, J. A. G. *J. Chem. Soc., Dalton Trans.* **1996**, (18), 3613-3628.
56. Heffern, M. C.; Matosziuk, L. M.; Meade, T. J., *Chem Rev* **2014**, 114 (8), 4496-539.
57. Ramalho, J.; Semelka, R. C.; Ramalho, M.; Nunes, R. H.; AlObaidy, M.; Castillo, M. *Am. J. Neuroradiol.* **2016**, 37, (7), 1192-1198.
58. Idée, J.-M.; Port, M.; Robic, C.; Medina, C.; Sabatou, M.; Corot, C. *Journal of Magnetic Resonance Imaging* **2009**, 30, (6), 1249-1258.
59. Lacerda, S.; Bonnet, C. S.; Pallier, A.; Villette, S.; Foucher, F.; Westall, F.; Buron, F.; Suzenet, F.; Pichon, C.; Petoud, S.; Tóth, É. *Small* **2013**, 9, (16), 2662-2666.
60. Parker, D. *Chem. Soc. Rev.* **2004**, 33, (3), 156-165.
61. Moore, E. G.; Samuel, A. P. S.; Raymond, K. N. *Acc. Chem. Res.* **2009**, 42, (4), 542-552.
62. Yuan, J.; Wang, G. *J. Fluoresc.* **2005**, 15, (4), 559-568.
63. Yuan, J.; Tan, M.; Wang, G. *J. Lumin.* **2004**, 106, (2), 91-101.
64. Selvin, P. R. *Nature Structural Biology* **2000**, 7, (9), 730-734.
65. Torelli, S.; Imbert, D.; Cantuel, M.; Bernardinelli, G.; Delahaye, S.; Hauser, A.; Bünzli, J.-C. G.; Piguet, C. *Chem. Eur. J.* **2005**, 11, (11), 3228-3242.
66. Imbert, D.; Cantuel, M.; Bünzli, J.-C. G.; Bernardinelli, G.; Piguet, C. *J. Am. Chem. Soc.* **2003**, 125, (51), 15698-15699.
67. Seidlin, S. M.; Marinelli, L. D.; Oshry, E. *Journal of the American Medical Association* **1946**, 132, (14), 838-847.
68. Huang, C.; Song, T.; Mukherji, S. K.; Zhang, L.; Lu, J.; Chen, X.; Xian, J. *J. Comput. Assist. Tomogr.* **2020**, 44, (4), 540-545.
69. Quick, H. H. *J. Magn. Res. Imaging* **2014**, 39, (2), 243-258.
70. Beekman, F. J.; McElroy, D. P.; Berger, F.; Gambhir, S. S.; Hoffman, E. J.; Cherry, S. R. *Eur. J. Nucl. Med. Mol. Imag.* **2002**, 29, (7), 933-938.
71. Scott, P. J. H. *Angew. Chem. Int. Ed.* **2009**, 48, (33), 6001-6004.
72. Adam, M. J.; Wilbur, D. S. *Chem. Soc. Rev.* **2005**, 34, (2), 153-163.
73. Vinken, R.; Schmidt, B.; Schäffer, A. *J. Label. Compd. Radiopharm.* **2002**, 45, (14), 1253-1263.
74. Wolterbeek, B.; Kloosterman, J. L.; Lathouwers, D.; Rohde, M.; Winkelman, A.; Frima, L.; Wols, F. *J. Radioanal. Nucl. Chem.* **2014**, 302, (2), 773-779.
75. Rösch, F.; Forssell-Aronsson, E. *Met. Ions Biol. Syst.* **2004**, 42, 77-108.
76. Hippeläinen, E.; Tenhunen, M.; Mäenpää, H.; Sohlberg, A. *EJNMMI Res* **2016**, 6, (1), 16-16.
77. Müller, C.; Zhernosekov, K.; Köster, U.; Johnston, K.; Dorrer, H.; Hohn, A.; van der Walt, N. T.; Türlér, A.; Schibli, R. *J. Nucl. Med.* **2012**, 53, (12), 1951-1959.
78. Grünberg, J.; Lindenblatt, D.; Dorrer, H.; Cohrs, S.; Zhernosekov, K.; Köster, U.; Türlér, A.; Fischer, E.; Schibli, R. *Eur. J. Nucl. Med. Mol. Imag.* **2014**, 41, (10), 1907-1915.
79. Lehenberger, S.; Barkhausen, C.; Cohrs, S.; Fischer, E.; Grünberg, J.; Hohn, A.; Köster, U.; Schibli, R.; Türlér, A.; Zhernosekov, K. *Nucl. Med. Biol.* **2011**, 38, (6), 917-24.
80. Smits, M. L. J.; Nijssen, J. F. W.; van den Bosch, M. A. A. J.; Lam, M. G. E. H.; Vente, M. A. D.; Mali, W. P. T. M.; van het Schip, A. D.; Zonnenberg, B. A., *Lancet Oncol.* **2012**, 13, 1025-1034.

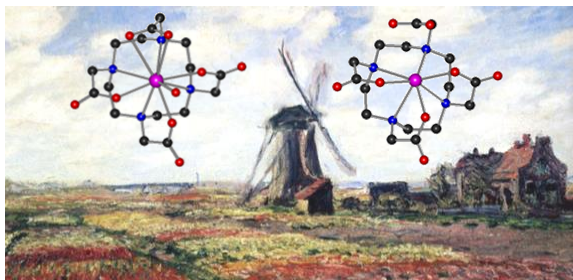
81. Martinelli, J.; Denkova, A. G.; Arranja, A.; Terpstra, B. E.; Zhang, W.; Djanashvili, K. *Bioconj. Chem.* **2016**, 27, (2), 446-456.
82. Smits, M.; Nijsen, J.; van den Bosch, M.; Lam, M.; Vente, M.; Huijbregts, J.; van het Schip, A.; Elschot, M.; Bult, W.; de Jong, H.; Meulenhoff, P.; Zonnenberg, B. *J. Exp. Clin. Cancer Res.* **2010**, 29, (1), 70.
83. Smits, M. L. J.; Nijsen, J. F. W.; van den Bosch, M. A. A. J.; Lam, M. G. E. H.; Vente, M. A. D.; Mali, W. P. T. M.; van het Schip, A. D.; Zonnenberg, B. A. *The Lancet Oncology* **2012**, 13, (10), 1025-1034.
84. Barth, R. F.; Coderre, J. A.; Vicente, M. G. H.; Blue, T. E. *Clin. Cancer. Res.* **2005**, 11, (11), 3987.
85. Putri Fauzia, R.; Denkova, A. G.; Djanashvili, K. *Inorganics* **2019**, 7, (5), 59.
86. Deagostino, A.; Protti, N.; Alberti, D.; Boggio, P.; Bortolussi, S.; Altieri, S.; Crich, S. G. *Future Medicinal Chemistry* **2016**, 8, (8), 899-917.
87. Salt, C.; Lennox, A. J.; Takagaki, M.; Maguire, J. A.; Hosmane, N. S. *Russ. Chem. Bull.* **2004**, 53, (9), 1871-1888.
88. Le, U. M.; Cui, Z. *Int. J. Pharmaceut.* **2006**, 312, (1), 105-112.
89. Haley, T. J. *J. Pharm. Sci.* **1965**, 54, (5), 663-670.
90. Hao, D.; Ai, T.; Goerner, F.; Hu, X.; Runge, V. M.; Tweedle, M. *J. Magn. Reson. Imaging* **2012**, 36, (5), 1060-71.
91. Turyanskaya, A.; Rauwolf, M.; Pichler, V.; Simon, R.; Burghammer, M.; Fox, O. J. L.; Sawhney, K.; Hofstaetter, J. G.; Roschger, A.; Roschger, P.; Wobrauschek, P.; Streli, C. *Sci. Rep.* **2020**, 10, (1), 6301.
92. Kanal, E.; Tweedle, M. F. *Radiology* **2015**, 275, (3), 630-4.
93. Weissleder, R.; Mahmood, U. *Radiology* **2001**, 219, (2), 316-333.
94. Accardo, A.; Tesaro, D.; Aloj, L.; Pedone, C.; Morelli, G. *Coord. Chem. Rev.* **2009**, 253, (17), 2193-2213.
95. L. Villaraza, A. J.; Bumb, A.; Brechbiel, M. W. *Chemical Reviews* **2010**, 110, (5), 2921-2959.
96. Ferreira, M. F.; Gonçalves, J.; Mousavi, B.; Prata, M. I. M.; Rodrigues, S. P. J.; Calle, D.; López-Larrubia, P.; Cerdan, S.; Rodrigues, T. B.; Ferreira, P. M.; Helm, L.; Martins, J. A.; Geraldés, C. F. G. C. *Dalton Trans.* **2015**, 44, (9), 4016-4031.
97. Peters, J. A.; Djanashvili, K. *Eur. J. Inorg. Chem.* **2012**, 2012, (12), 1961-1974.
98. Zhang, W.; Peters, J. A.; Mayer, F.; Helm, L.; Djanashvili, K. *The Journal of Physical Chemistry C* **2015**, 119, (9), 5080-5089.
99. Wartenberg, N.; Fries, P.; Raccurt, O.; Guillermo, A.; Imbert, D.; Mazzanti, M. *Chem. Eur. J.* **2013**, 19, (22), 6980-6983.
100. Callewaert, M.; Roullin, V. G.; Cadiou, C.; Millart, E.; Van Gulik, L.; Andry, M. C.; Portefaix, C.; Hoeffel, C.; Laurent, S.; Elst, L. V.; Muller, R.; Molinari, M.; Chuburu, F. *J. Mater. Chem. B* **2014**, 2, (37), 6397-6405.
101. Haase, M.; Schäfer, H. *Angew. Chem. Int. Ed.* **2011**, 50, (26), 5808-5829.
102. Mandl, G. A.; Cooper, D. R.; Hirsch, T.; Seuntjens, J.; Capobianco, J. A. *Methods and Appl. in Fluoresc.* **2019**, 7, (1), 012004.
103. DaCosta, M. V.; Doughan, S.; Han, Y.; Krull, U. J. *Analytica Chimica Acta* **2014**, 832, 1-33.
104. Torchilin, V. *Adv. Drug Del. Rev.* **2011**, 63, (3), 131-135.
105. Ren, L.; Chen, S.; Li, H.; Zhang, Z.; Ye, C.; Liu, M.; Zhou, X. *Nanoscale* **2015**, 7, (30), 12843-12850.

106. Kelkar, S. S.; Reineke, T. M. *Bioconj. Chem.* **2011**, 22, (10), 1879-1903.
107. Schühle, D. T.; Schatz, J.; Laurent, S.; Vander Elst, L.; Muller, R. N.; Stuart, M. C. A.; Peters, J. A. *Chem. Eur. J.* **2009**, 15, (13), 3290-3296.
108. Schühle, D. T.; Polasek, M.; Lukes, I.; Chauvin, T.; Toth, E.; Schatz, J.; Hanefeld, U.; Stuart, M. C. A.; Peters, J. A. *Dalton Trans.* **2010**, 39, (1), 185-191.
109. Schühle, D. T.; van Rijn, P.; Laurent, S.; Vander Elst, L.; Muller, R. N.; Stuart, M. C. A.; Schatz, J.; Peters, J. A. *Chem. Commun.* **2010**, 46, (24), 4399-4401.
110. Zhang, W.; Peters, J. A.; Mayer, F.; Helm, L.; Djanashvili, K. *J. Phys. Chem. C* **2015**, 119, 5080-5089.

---

# <sup>17</sup>O NMR and DFT Study of the Dynamics of the Carboxylate Groups in DOTA Complexes of Lanthanides in Aqueous Solution

# 2





## Introduction

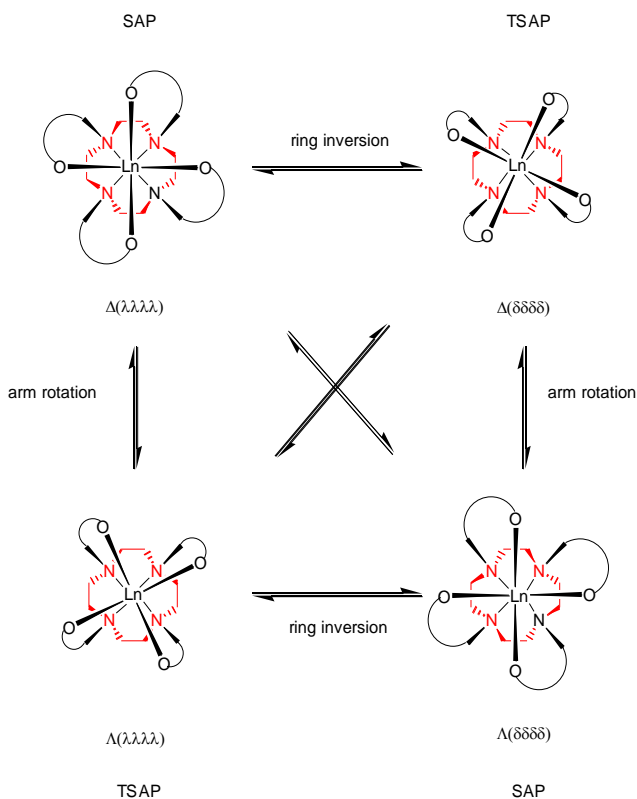
The macrocyclic compound DOTA (DOTA = 1,4,7,10-tetraazacyclododecane-1,4,7,10-tetraacetate) forms complexes with lanthanide ions with high thermodynamic stability and kinetic inertness with respect to the release of the metal ion.<sup>1,2</sup> Consequently, these complexes have found widespread use in diagnostic and therapeutic medicine. Notably,  $[\text{Gd}(\text{DOTA})(\text{H}_2\text{O})]^-$  is being successfully applied as a contrast agent in magnetic resonance imaging (MRI).<sup>3-5</sup> The contrast enhancement is achieved by the increase of the longitudinal relaxation rate of water protons in the vicinity of the paramagnetic complex. The efficiency of a contrast agent is usually expressed by its relaxivity (the relaxation rate enhancement in  $\text{s}^{-1}$  per mM concentration of  $\text{Gd}^{3+}$ ), which is determined by several parameters including the electronic relaxation rate of  $\text{Gd}^{3+}$ , the rotational dynamics of the complex, and the exchange rate of the  $\text{Gd}^{3+}$  coordinated water molecule.

Currently, a great deal of research is devoted to molecular imaging applications of MRI.<sup>6,7</sup> In this case, the low intrinsic sensitivity of this technique is often a limitation, and therefore, relatively large local concentrations of a contrast agent are required to obtain an observable contrast enhancement. This may be achieved by employing targeted agents that can deliver multiple  $\text{Gd}^{3+}$ -chelates to the sites of interest. Obviously, it is important that each of these  $\text{Gd}^{3+}$  chelates has optimal relaxivity. For the rational design of MRI contrast agents with optimal relaxivity, detailed understanding of the structural parameters controlling the relaxivity is indispensable.

The DOTA ligand is known to bind  $\text{Ln}^{3+}$  ions octadentately through its 4 N atoms and an O-atom of each of the 4 carboxylate functions.<sup>8-11</sup> The ethylene groups of the macrocycle adopt two different gauche orientations ( $\lambda$  or  $\delta$ ), whereas the pendant acetate arms are twisted around the  $\text{Ln}^{3+}$  ion in two orientations,  $\Lambda$  and  $\Delta$ . In solution two diastereomeric forms,  $\Delta(\delta\delta\delta\delta)/\Lambda(\lambda\lambda\lambda\lambda)$  and  $\Delta(\lambda\lambda\lambda\lambda)/\Lambda(\delta\delta\delta\delta)$ , occur, which differ in the mutual orientation of the parallel planes formed by the Ln-bound N- and O-atoms (see Scheme 2.1). The twist angles between these planes are about  $+40^\circ$  and  $-24^\circ$  corresponding to square antiprismatic (SAP, often labeled M) and twisted square antiprismatic (TSAP, often labeled m) coordination geometries, respectively. The ratio of SAP/TSAP changes along the lanthanide series: La-DOTA occurs predominantly in the TSAP form, whereas for Yb-DOTA the SAP form predominates. A hydration equilibrium is superimposed on this conformational equilibrium

to give sets of both 8- and 9-coordinated species. The 9-coordinate species predominate for Ln = La to Er, whereas the 8-coordinate Ln-complexes have only been observed for the heavier lanthanides (Er→Lu) and then exclusively in the TSAP geometry.<sup>9</sup> Both the SAP and TSAP isomers of [Sc(DOTA)]<sup>-</sup> are known to exist in solution as 8-coordinate species.

With the use of variable temperature <sup>13</sup>C NMR on [Nd(DOTA)]<sup>-</sup> and <sup>1</sup>H EXSY on [Yb(DOTA)]<sup>-</sup>, it has been shown that the four isomers of the 9-coordinated species all interconvert. Based on extensive variable temperature and pressure NMR studies, a semi-quantitative energy diagram for the various rearrangements in Ln-DOTA complexes has been proposed.<sup>9</sup>



**Scheme 2.1.** Schematic representation of the conformational isomers of Ln-DOTA complexes. Two sets occur: 8-coordinated and 9-coordinated; in the latter, a water molecule caps the O<sub>4</sub> plane. The SAP forms have not been observed for the 8-coordinated complexes.

The exchange rate of water molecules between the Ln-DOTA complexes and the bulk has been shown to be significantly higher for the TSAP than for the SAP form.<sup>12-16</sup> For [Gd(DOTA)(H<sub>2</sub>O)]<sup>-</sup>, the overall water exchange rate is  $4.1 \times 10^6 \text{ s}^{-1}$ ,<sup>17</sup> whereas the interconversion rates of the various forms of the DOTA ligand are several orders of magnitude lower.<sup>9,11</sup>

A question that remains to be answered is whether the carboxylate groups are immobilized or rotating in the Ln-DOTA complexes. Therefore, we here evaluate the rates of interconversion of the carboxylate oxygen atoms in Ln-DOTA complexes, using <sup>17</sup>O NMR and density functional theory (DFT) calculations. Previously, Purgel *et al.* have reported DFT calculations on SAP and TSAP isomers of [Eu(DOTA)(H<sub>2</sub>O)]<sup>-</sup> and [Lu(DOTA)]<sup>-</sup>.<sup>18</sup> In order to get some insight into the effect of the decrease of the ionic radius on the carboxylate rotation we first performed similar calculations on various isomers of DOTA complexes with selected Ln<sup>3+</sup> ions along the lanthanide series from La<sup>3+</sup> to Lu<sup>3+</sup>. For comparison Sc<sup>3+</sup>, a rare earth with a significantly smaller ionic radius than the lanthanides, was included in this study. Next, these optimal structures were used to model the transition state of the carboxylate rotation. The rotation rates obtained are compared with the results of a variable temperature <sup>17</sup>O NMR study on Ln-DOTA complexes with <sup>17</sup>O-enriched carboxylate functions. Finally, the results are discussed in view of the known rates of hydration and isomerization of Ln-DOTA complexes.

## Results and Discussion

**Computation of molecular geometries and conformational energies.** Aiming to obtain a deeper understanding of the conformational properties of the Ln<sup>3+</sup> and Sc<sup>3+</sup> complexes of DOTA we have performed full geometry optimizations of the [Ln(DOTA)(H<sub>2</sub>O)]<sup>-</sup> (Ln = La, Nd, Sm, Tb or Ho), [Ln(DOTA)]<sup>-</sup> (Ln = Tm or Lu) and [Sc(DOTA)]<sup>-</sup> systems at the B3LYP level. As expected, these calculations provide the SAP and TSAP isomers as minimum energy conformations. The main geometrical parameters calculated for the Nd<sup>3+</sup>, Tm<sup>3+</sup> and Sc<sup>3+</sup> complexes are compared to the experimental data obtained from X-ray diffraction in Table 2.1<sup>19</sup> (for the Cartesian coordinates of all geometries obtained from computations see Table S1 in the supporting material in

**Table 2.1.** Geometrical parameters of experimental (X-ray) and calculated structures for the two isomers of [Nd(DOTA)(H<sub>2</sub>O)]<sup>-</sup>, [Tm(DOTA)]<sup>-</sup> and [Sc(DOTA)]<sup>-</sup> complexes.<sup>a</sup>

	[Nd(DOTA)(H <sub>2</sub> O)] <sup>-</sup>			[Tm(DOTA)] <sup>-</sup>			[Sc(DOTA)] <sup>-</sup>		
	SAP	SAP	TSAP <sup>b</sup>	SAP <sup>b</sup>	TSAP	TSAP	SAP	SAP	TSAP <sup>b</sup>
	calc	exp	calc	calc	calc	exp	calc	exp	calc
Ln-N	2.833	2.704	2.864	2.700	2.733	2.529	2.637	2.446	2.685
Ln-O	2.433	2.416	2.436	2.268	2.267	2.280	2.101	2.154	2.098
Ln-O <sub>w</sub>	2.631	2.508	2.622	–	–	–	–	–	–
ω <sup>c</sup>	37.6	37.8	-24.9	39.4	-26.3	-24.4	41.2	41.2	-28.2
Ln-P <sub>O</sub> <sup>d</sup>	0.587	0.684	0.643	0.748	0.796	1.064	0.765	1.007	0.785
Ln-P <sub>N</sub> <sup>e</sup>	1.837	1.676	1.907	1.666	1.740	1.466	1.596	1.327	1.689
P <sub>O</sub> -P <sub>N</sub> <sup>f</sup>	2.424	2.360	2.551	2.414	2.631	2.530	2.360	2.334	2.474

<sup>a</sup> Distances (Å); The average values of bond distances to the oxygen atoms of the P<sub>O</sub> (Ln-O) and P<sub>N</sub> (Ln-N) planes are reported; O<sub>w</sub>, oxygen atom of the inner-sphere water molecule. <sup>b</sup> No experimental data available. <sup>c</sup> Mean twist angle (°) of the upper and lower planes. <sup>d</sup> Distance between the lanthanide and the least-squares plane defined by the coordinated oxygen atoms, P<sub>O</sub>. <sup>e</sup> Distance between the lanthanide and the least-squares plane defined by the nitrogen atoms, P<sub>N</sub>. <sup>f</sup> Distance between the centroids of the P<sub>O</sub> and P<sub>N</sub> planes.

literature<sup>20</sup>). The distances between the metal ions and the donor atoms of the ligand decrease along the lanthanide series, as usually observed for Ln<sup>3+</sup> complexes as a consequence of the lanthanide contraction.<sup>21</sup> The average Ln-O distances obtained from DFT calculations are in excellent agreement with the experimental values. The coordination polyhedron around the lanthanide ion may be considered to be comprised of two virtually parallel pseudo planes: the four amine nitrogen atoms define the lower plane (P<sub>N</sub>), while the four oxygen atoms coordinated to the metal ion define the upper plane (P<sub>O</sub>). The mean twist angles of these parallel planes (ω) are also in very good agreement with the experimental values. As observed previously for related systems,<sup>18</sup> the main discrepancy between the experimental and calculated geometries arises from the Ln-N distances. Indeed, the optimized geometries present substantially longer Ln-N bond distances than the solid state structures, which is also reflected in the Ln-P<sub>N</sub> and Ln-P<sub>O</sub> values. This can be partially ascribed, in the case of Ln<sup>3+</sup> complexes, to the fact that the large-core effective core potential (ECPs) usually provide bond distances that are 0.02-0.07 Å longer than the experimental ones.<sup>22,23</sup>

To test the effect of the solvent on the geometries of these complexes we have performed geometry optimizations of [La(DOTA)(H<sub>2</sub>O)]<sup>-</sup> and [Lu(DOTA)]<sup>-</sup> in aqueous solution by using a polarizable continuum model (PCM). Our results show that the inclusion of solvent

effects results in a relatively important shortening of the Ln-N bond distances (about 0.03-0.07 Å), while the Ln-O bonds are only slightly increased (< 0.04 Å). However, it is well known that geometry optimizations in solution based on the PCM model suffer from convergence problems such as slow convergence, no convergence, or convergence to higher energetic conformations.<sup>24-26</sup> The main goal of this work is to study the exchange between coordinated and non-coordinated oxygen atoms of acetate groups in Ln<sup>3+</sup>-DOTA complexes, which requires the characterization of energy minima and transition states by using frequency analysis. Geometry optimizations of the transition states involved in this exchange process suffered from convergence difficulties. Thus, in the following we will focus on the geometries of the different complexes optimized in the gas phase, even when they are expected to possess considerably long Ln-N distances in comparison to experimental data.

The relative populations of the TSAP and SAP conformations of Ln<sup>3+</sup> and Sc<sup>3+</sup> complexes of DOTA have been studied in detail by using NMR spectroscopy.<sup>9</sup> One can easily derive relative free energies from the populations of the two isomers using the formula  $\Delta G^\circ = -RT \cdot \ln K$ . The experimental evidence shows that the abundance of the TSAP isomer is progressively decreasing moving to the right across the lanthanide series.<sup>8-11</sup> Our calculations indeed predict a stabilization of the SAP isomer upon decreasing the ionic radius of the metal ion, in good agreement with the experimental results (Figure 2.1). Furthermore, our calculations predict a slight stabilization of the TSAP isomer for the heaviest lanthanides, in good agreement with the experimental trend. This stabilization of the TSAP form is most likely due to a change of the coordination number from 9 to 8 along the lanthanide series as a result of the expulsion of the inner sphere water molecule upon going to the smallest lanthanides (Tm-Lu). It must be pointed out that a hydration equilibrium is superimposed on the conformational equilibrium between SAP and TSAP isomers for the heaviest lanthanides (Tm-Lu), with both 8- and 9-coordinated species being observed for the TSAP forms.<sup>9</sup> However, only 8-coordinated species were considered in our calculations for the Tm<sup>3+</sup> and Lu<sup>3+</sup> complexes to avoid difficulties associated to the calculation of relative energies between species involved in a hydration equilibrium (i.e. standard state correction<sup>27</sup> and basis set superposition errors<sup>28,29</sup>). While being a relatively crude model, our calculations reproduce fairly well the experimental trend observed for the free energies between SAP and TSAP forms. Furthermore, the quantitative agreement between the experimental and calculated

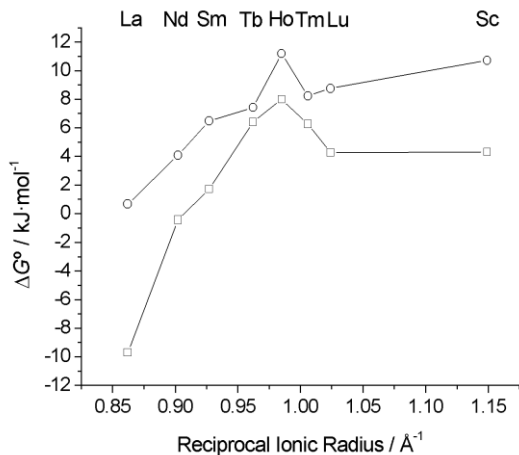


**Figure 2.1.** Experimental (□) and calculated (○) relative free energies for the SAP ⇌ TSAP equilibrium in [Ln(DOTA)(H<sub>2</sub>O)]<sup>-</sup> (Ln = La-Ho), [Ln(DOTA)]<sup>-</sup> (Ln = Tm, Lu) and [Sc(DOTA)]<sup>-</sup> complexes versus the reciprocal ionic radius of the metal ion. Positive free energies indicate that the SAP isomer is more stable than the TSAP one.

data is reasonably good, with differences between them of 10.5 kJ·mol<sup>-1</sup> for La and 0.8 – 6.3 kJ·mol<sup>-1</sup> for the Nd-Lu and Sc complexes (Table 2.2). Thus, we conclude that our computational approach reproduces fairly well the structures and energetics of Ln<sup>3+</sup> and Sc<sup>3+</sup> DOTA complexes.

**Exchange between bound and unbound oxygen atoms of acetate groups.** The exchange between the coordinated and non coordinated O-atoms of acetate groups was investigated for the [Ln(DOTA)(H<sub>2</sub>O)]<sup>-</sup> (Ln = La, Nd or Sm), [Ln(DOTA)]<sup>-</sup> (Ln = Tm or Lu) and [Sc(DOTA)]<sup>-</sup> systems. Additional calculations were also performed for the SAP isomers of [Ln(DOTA)(H<sub>2</sub>O)]<sup>-</sup> complexes (Ln = Tm, Lu), for which the experimental

**Table 2.2.** Relative free energies (ΔG°) for the SAP ⇌ TSAP equilibrium in [Ln(DOTA)(H<sub>2</sub>O)]<sup>-</sup> (Ln = La, Nd, Sm), [Ln(DOTA)]<sup>-</sup> (Ln = Tm, Lu) and [Sc(DOTA)]<sup>-</sup> complexes (kJ·mol<sup>-1</sup>).<sup>a</sup>

Ln	La	Nd	Sm	Tm	Lu	Sc
ΔG° <sub>calc</sub>	0.67	4.10	6.49	8.25	8.75	10.72
ΔG° <sub>exp</sub>	-9.71	-0.42	1.72	6.28	4.27	4.31

<sup>a</sup> Relative free energies are defined as ΔG° = G°<sub>TSAP</sub> - G°<sub>SAP</sub>; Note that the actual values of the complex free energies are negative, and therefore a positive relative free energy indicates that the SAP isomer is more stable than the TSAP one.

evidence points to the presence of a coordinated water molecule.<sup>9</sup> However, in the latter cases attempts to model the carboxylate rotation process failed, geometry optimizations of the relevant transition states (TSs) leading to molecular geometries where an unbound carboxylate unit was involved in strong hydrogen-bonding interaction with the coordinated water molecule. For the remaining systems, the investigated exchange between bound and unbound oxygen atoms of acetate groups involves a rotation of the N-C-C-O dihedral angles of acetate groups, leading to a TS in which the distances between the O-atoms of the acetate involved in the rotation process and the lanthanide ion are considerably longer than in the reactant. Figure 2.2 shows the representative cases of energy minima and TSs for the SAP isomers of  $\text{La}^{3+}$  and  $\text{Lu}^{3+}$  complexes. According to our calculations, the rotation of the carboxylate group for the largest  $\text{Ln}^{3+}$  ions does not require a full decoordination of the pendant arm, which in the transition state binds to the metal ion in a nearly symmetrical bidentate fashion. This situation is observed for both the SAP and TSAP isomers, the distances between the  $\text{Ln}^{3+}$  ion and the O-atoms of the bidentate acetate group in the TS amounting to 2.73 and 2.86 Å for the TSAP isomer of the  $\text{La}^{3+}$  complex. The formation of the TS requires an important deformation of the metal coordination environment (Figure 2.2).

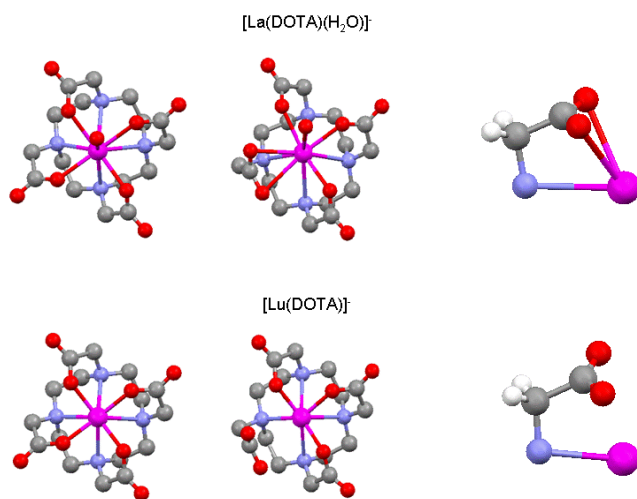


**Figure 2.2.** Structures of the energy minima for the SAP isomers of  $[\text{La}(\text{DOTA})(\text{H}_2\text{O})]^-$  and  $[\text{Lu}(\text{DOTA})]^-$  complexes (left) and the TSs of the carboxylate rotation (center). The right column shows expansions around the rotating carboxylate of the TSs. In the TS, the  $\text{Ln-O}$  distances are 2.9 and 3.2 Å for La and Lu, respectively.

In TSs, the distances of the  $\text{Ln}^{3+}$  ion to O-atoms of the acetate group undergoing the rotation process gradually increase along the lanthanide series, reaching values of 3.23 and 3.26 Å (SAP), and 3.68 and 3.74 Å (TSAP) for the  $\text{Lu}^{3+}$  complexes. Thus, the interaction of the rotating carboxylate group and the  $\text{Ln}^{3+}$  ion in the TS is weakened as the ionic radius of the  $\text{Ln}^{3+}$  ions decreases, being in fact fully decoordinated in the case of the smallest lanthanides and  $\text{Sc}^{3+}$ . This results in smaller changes of the remaining bond distances of the metal coordination environment for the small lanthanides going from the ground to the TS (Figure 2.2).

The activation free energies for the carboxylate rotation process show a steady increase along the lanthanide series from  $\text{La}^{3+}$  to  $\text{Lu}^{3+}$  (Table 2.3 and Figure 2.3), with values of  $\sim 75$   $\text{kJ}\cdot\text{mol}^{-1}$  for  $\text{La}^{3+}$  and  $\sim 126$   $\text{kJ}\cdot\text{mol}^{-1}$  for  $\text{Lu}^{3+}$ . This can be attributed to i) the decrease in space for the coordination of the oxygen atoms of the rotating carboxylate in the TS, and ii) the increasing charge density of the metal ion. A slight decrease of the activation free energies for the rotation of the carboxylate group is predicted upon decreasing the ionic radius of the metal ion from  $\text{Lu}^{3+}$  to  $\text{Sc}^{3+}$ . This effect can be explained by the stabilization of the 7-coordinate transition state in the  $\text{Sc}^{3+}$  analogue due to the smaller size of the metal ion. The activation energies calculated in the gas phase are slightly higher for the SAP isomers than for the TSAP forms.

Single point energy calculations in aqueous solution (PCM model) were performed at all critical points to evaluate the effects of the solvent in the energy barriers involved in the carboxylate rotation process. Our results show that the inclusion of solvent effects has a relatively small impact in the calculated free energy values, which decrease by  $\sim 8$ -21  $\text{kJ}\cdot\text{mol}^{-1}$  in solution with respect to the gas-phase (Table 2.3). The lower energy barriers calculated in solution are probably the result of a more efficient solvation of the carboxylate

**Table 2.3.** Computed free energies of transition states (TS) involved in the carboxylate rotation process of SAP and TSAP isomers of  $[\text{Ln}(\text{DOTA})(\text{H}_2\text{O})]^-$  ( $\text{Ln} = \text{La-Sm}$ ),  $[\text{Ln}(\text{DOTA})]^-$  ( $\text{Ln} = \text{Tm, Lu}$ ) and  $[\text{Sc}(\text{DOTA})]^-$  complexes (in  $\text{kJ}\cdot\text{mol}^{-1}$ ) relative to those of the corresponding energy minima.

		La	Nd	Sm	Tm	Lu	Sc
SAP	gas-phase	78.7	92.1	100.1	133.1	136.1	126.0
	solution	70.8	80.4	92.5	119.3	122.3	106.8
TSAP	gas-phase	76.2	87.1	90.9	124.8	126.9	117.6
	solution	70.3	83.3	92.1		110.0	99.6



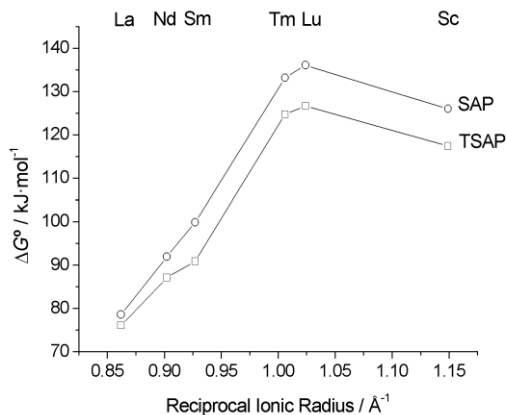


**Figure 2.3.** Activation free energies from DFT calculations performed in the gas-phase for the carboxylate rotation process in SAP (○) and TSAP (□) isomers of  $[\text{Ln}(\text{DOTA})(\text{H}_2\text{O})]^-$  (Ln = La-Sm),  $[\text{Ln}(\text{DOTA})]^-$  (Ln = Tm, Lu) and  $[\text{Sc}(\text{DOTA})]^-$  complexes.

group undergoing the rotation process in the transition state in comparison to the ground state. This effect is magnified on proceeding to the right across the series due to the complete decoordination of the acetate pendant in the transition state. The free energy barriers for the carboxylate rotation process calculated for the SAP and TSAP isomers in aqueous solution are very similar, differing by less than  $12.6 \text{ kJ}\cdot\text{mol}^{-1}$ .

**Variable temperature  $^{17}\text{O}$  NMR measurements.** With the aim to verify the conclusions of the computations with experimental evidence, variable temperature  $^{17}\text{O}$  NMR measurements were performed on Ln- and Sc-DOTA complexes with about 2%  $^{17}\text{O}$ -enriched carboxylate functions. The  $^{17}\text{O}$ -enriched ligand was obtained by heating the acid in 2%  $^{17}\text{O}$ -enriched water at 363 K for 18 h, followed by lyophilization and subsequent formation of the corresponding lanthanide complex. All samples had a small excess of free ligand ( $\leq 5 \text{ mol } \%$ ), which has a single resonance for the carboxylate groups at 278 ppm at pH 6.3 and 298 K and at 18.8 T.

Separate  $^{17}\text{O}$  resonances were observed for Ln-DOTA and the free ligand, demonstrating that the exchange between complex and free ligand is slow on the NMR time scale, as should be expected. The spectra of the diamagnetic La-DOTA complex showed a single carboxylate  $^{17}\text{O}$  resonance at 295-302 ppm between 25 and 147 °C, and at magnetic fields of 7.0, 9.4, and 18.8 T. Apparently, the exchange between the two carboxylate  $^{17}\text{O}$  resonances is rapid on the

NMR timescale under the conditions applied. The linewidths of these resonances decreased significantly upon increase of the temperature (see Figure 2.4), which might be ascribed to the decrease of the rotational correlation time and the associated enhancement of the quadrupole relaxation time, which is the predominant <sup>17</sup>O NMR relaxation mechanism of diamagnetic compounds in the absence of exchange.<sup>30</sup> In addition there might be a decrease in linewidth due to a decrease of exchange broadening.

The <sup>17</sup>O NMR spectra of the paramagnetic Pr- and Sm-DOTA complexes and that of the diamagnetic Lu- and Sc-DOTA complexes each displayed two resonances of equal intensities (see Figures 2.4 and 2.5). One of the resonances of Lu-DOTA and the resonance of free DOTA are superimposed. The carboxylate <sup>17</sup>O resonances for Sc(DOTA)<sup>-</sup> almost coincided; an asymmetric signal was observed that could be deconvoluted into two Lorentzian peaks of equal intensity. No resonances could be observed for the DOTA complexes of heavier paramagnetic Ln<sup>3+</sup> ions (Dy<sup>3+</sup>, Ho<sup>3+</sup>, and Yb<sup>3+</sup>), probably due to excessive line broadening as a result of their relatively large effective magnetic moments. In a later study, Fusaro *et al.* investigated Gd(DOTA)<sup>-</sup> by <sup>17</sup>O-NMR spectroscopy and were able to observe the <sup>17</sup>O NMR signal of the unbound carboxylate oxygen at a 212 ppm, which is in good agreement with the

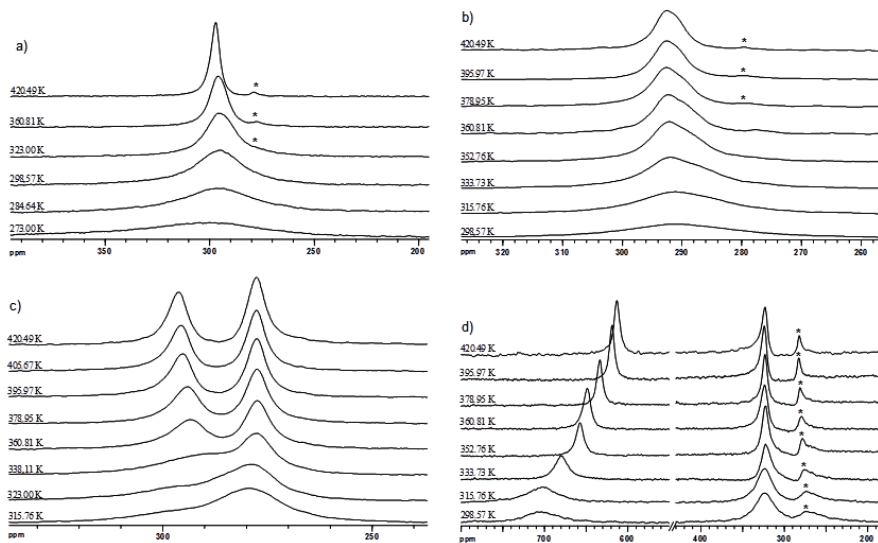


**Figure 2.4.** <sup>17</sup>O NMR spectra of La(DOTA)<sup>-</sup> (a), Sc(DOTA)<sup>-</sup> (b), Lu(DOTA)<sup>-</sup> (c) and Pr(DOTA)<sup>-</sup> (d) at 18.8 T and different temperatures. The linewidths of the signals are clearly decreasing with temperature. The resonance of the excess free DOTA-ligand is indicated with an asterisk. Numbers on the left indicate the temperature at which the spectrum was taken.

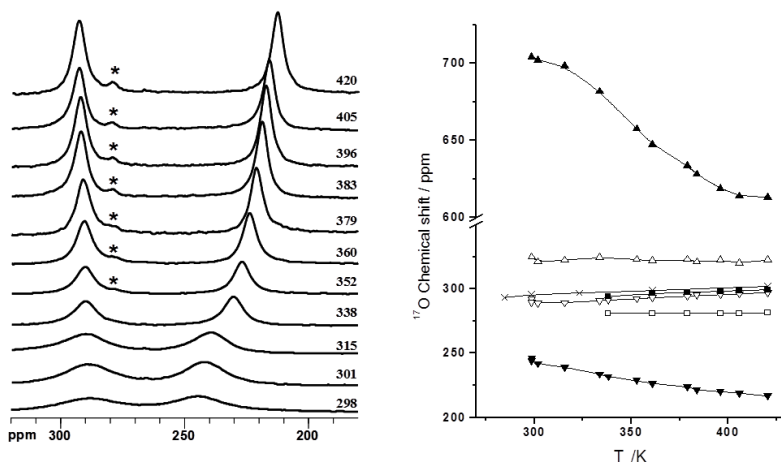


**Figure 2.5.** a)  $^{17}\text{O}$  NMR spectra of  $\text{Sm}(\text{DOTA})^-$  at 18.8 T at different temperatures (K). The linewidth of the signal is clearly decreasing with the temperature. The resonance for the excess free ligand is indicated with an asterisk. b)  $^{17}\text{O}$  chemical shifts of the carboxylate oxygens in  $\text{Ln}(\text{DOTA})^-$  complexes as a function of temperature. Crosses, Ln = La (averaged signal for Ln-bound and unbound O); up triangles, Ln = Pr; down triangles Ln = Sm; squares, Ln = Lu. The chemical shifts for Ln-bound O-atoms are marked with filled symbols and those for Ln-unbound O-atoms with open symbols. The curves are guides to the eyes.

calculations and estimations presented in the same work. Surprisingly, the unbound oxygen is almost unaffected by the paramagnetic effects of the Gd-center.<sup>31</sup>

The assignments of the here observed  $^{17}\text{O}$  resonances in the spectra for Pr- and Sm-DOTA were made on the basis of the temperature behavior of their chemical shifts. For one of the two signals for each of these complexes, the chemical shift was almost constant, whereas the other showed a relatively large temperature dependence (see Figure 2.5b). The  $^{17}\text{O}$  chemical shifts of these paramagnetic complexes consist of diamagnetic and paramagnetic contributions. The former shifts can be approximated by interpolation of the shifts of the diamagnetic  $\text{La}^{3+}$  and  $\text{Lu}^{3+}$  complexes. Hence, these shift contributions are about 270-300 ppm. The paramagnetic lanthanide induced shifts of Ln-bound O-atoms are known to be mainly of contact origin<sup>32</sup> and this shift contribution is proportional to  $T^{-1}$ . The induced shifts of the unbound O-atoms are usually negligible with respect to those of bound ones, which explains the difference in magnitude of the temperature dependence of the chemical shifts of those oxygens. The sign and the magnitude of the contact shift contribution is dependent on the  $\text{Ln}^{3+}$  ion in question.<sup>32</sup> It is known that the contact shifts of isostructural Pr and Sm

complexes have a ratio of -13.2, which is in agreement with the large difference in the chemical shifts observed for the Ln-bound O-atoms of the Pr- and Sm-DOTA complexes as well as with the opposite direction of the location of the resonances with respect to those of the corresponding diamagnetic La- and Lu-complexes. Since the diamagnetic shift contributions have a relatively small temperature dependence, the temperature dependence of the overall shifts are dominated by the temperature dependence of the contact shift and obviously, the overall chemical shifts of the Ln-bound O-atoms in Pr and Sm-DOTA move in opposite directions upon increase of the temperature.

Once again, the linewidth of these resonances decreases upon increase of the temperature (see Figures 2.4, 2.5, and Table 2.4). No coalescence of the two carboxylate <sup>17</sup>O resonances

**Table 2.4.** Summary of the linewidths (in Hz) of the resonances for M-DOTA (M = Sc, La, Pr, Sm, Lu) at different temperatures and magnetic fields.

		18.8 T								
		shift <sup>a</sup>	Temperature [K]							
		in Hz	315.8	323.0	333.7	360.8	379.0	396.0	405.7	420.5
Sc	Ln-O-C=O	32034	5409	- <sup>b</sup>	3991	2370	2080	1662	- <sup>b</sup>	1494
	Ln-O-C=O									
La	Ln-O-C=O	32764	- <sup>b</sup>	5393	- <sup>b</sup>	2930	- <sup>b</sup>	- <sup>b</sup>	- <sup>b</sup>	1389
	Ln-O-C=O									
Pr	Ln-O-C=O	66537	15592	- <sup>b</sup>	5700	3075	2205	1997	2395	2597
	Ln-O-C=O	34987	7594	- <sup>b</sup>	4089	3080	2303	2102	2583	2576
Sm	Ln-O-C=O	23512	5074	- <sup>b</sup>	3361	2011	1795	1565	1533	1646
	Ln-O-C=O	32244	6474	- <sup>b</sup>	4230	2364	2066	1855	1806	1834
Lu	Ln-O-C=O	30519	6192	4910	3843	2162	1880	1591	1497	1443
	Ln-O-C=O	32474	6456	7071	7379	3235	2435	1862	1726	1584
		4.7 T								
		shift <sup>c</sup>	Temperature [K]							
		in Hz	314.0	321.6	330.2	346.1	372.0	392.8	403.2	417.2
Sm	Ln-O-C=O	5754	5594	4852	3460	2971	1946	1750	1817	1732
	Ln-O-C=O	7856	6562	5427	3994	3426	2301	2122	1955	2054
Pr	Ln-O-C=O	16541	6776	4725	3836	2323	2182	1868	1922	1999
	Ln-O-C=O	8719	7878	5593	4637	3038	2521	2156	2248	2351

<sup>a</sup> at 420.5 K <sup>b</sup> not determined <sup>c</sup> at 417.2 K

**Table 2.5.**  $^{17}\text{O}$  NMR chemical shifts of carboxylate resonances of the various  $\text{Ln}(\text{DOTA})^-$  complexes at 298 K and 18.8 T in ppm.

Ln	Sc	La	Pr	Sm	Lu
$\text{Ln}-\text{O}-\text{C}=\text{O}$	291.6	295.7 <sup>a</sup>	704.2	244.2	282.5
$\text{Ln}-\text{O}-\text{C}=\text{O}$	283.7		324.9	289.5	300.9

<sup>a</sup>Averaged resonance observed.

was observed for these complexes up to the highest temperatures investigated (420 K). Upon heating the samples, initially even a decrease of linewidths was observed (see also discussion of the transverse relaxation rates below). Only at the highest temperatures investigated, the resonances of Pr-DOTA (> 390 K) and Sm-DOTA (> 400 K) started to broaden again.

The  $^{17}\text{O}$  NMR chemical shifts of the carboxylate resonances of various  $\text{Ln}(\text{DOTA})^-$  complexes are compiled in Table 2.5. All these complexes occur as two diastereomeric forms in aqueous solution<sup>9</sup> and therefore theoretically two pairs of resonances should be found. This is clearly not observed and the following explanations are possible: (i) the exchange between diastereomeric forms is fast on the  $^{17}\text{O}$  NMR timescale; (ii) the chemical shift difference between the SAP and the TSAP forms is small compared to the line width of the peaks; (iii) the amount of the minor form is much smaller than that of the major form. The latter explanation is unlikely, since it is known that the SAP and TSAP forms both occur in substantial amounts in aqueous samples of Pr- and Sm-DOTA.<sup>8-10</sup>

The observation of separate resonances for both oxygens in a carboxylate is rather uncommon. Generally, only a single averaged  $^{17}\text{O}$  NMR signal is observed in aqueous samples of uncomplexed carboxylic acids and carboxylates at 250-260 ppm, due to intermolecular proton transfer and electron delocalization, respectively.<sup>33</sup> Separate signals may appear for carboxylic acids in DMSO solution at about 175 and 340 ppm, where the proton exchange rate is strongly reduced by hydrogen bonding effects.<sup>33</sup>

The transverse relaxation rates ( $1/T_{2\text{obs}}$ ) of the various Ln-DOTA complexes were evaluated from the linewidths and are depicted as a function of the temperature in Figure 2.6 (see also Table 2.4). The observed relaxation rates for slow and fast exchange between the carboxylate oxygen atoms on the NMR timescale can be approximated by eqs 1 and 2, respectively.<sup>34-36</sup>

$$\frac{1}{T_{2obs,A}} = \frac{1}{T_{2A}} + \frac{1}{\tau_M}; \quad \frac{1}{T_{2obs,B}} = \frac{1}{T_{2B}} + \frac{1}{\tau_M} \quad (1)$$

$$\frac{1}{T_{2obs}} = \frac{0.5}{T_{2A}} + \frac{0.5}{T_{2B}} + 0.5 \tau_M \Delta\omega_{AB}^2 \quad (2)$$

$$\frac{1}{T_{2,X}} = \frac{1}{T_{2,X}^{298}} \exp \left[ \frac{E_A}{R} \left( \frac{1}{T} - \frac{1}{298.15} \right) \right] \quad X = A, B \quad (3)$$

$$\tau_M = \frac{298.15 \cdot \tau_M^{298}}{T} \exp \left[ \frac{\Delta H^\ddagger}{R} \left( \frac{1}{T} - \frac{1}{298.15} \right) \right] \quad (4)$$

Here, A and B denote the free and the bound states of the carboxylate O-atoms,  $\tau_M$  is the residence time of the nucleus in each of these states,  $\Delta\omega_{AB}$  is the difference in their resonance frequencies in  $\text{rad s}^{-1}$ ,  $1/T_{2A}$  and  $1/T_{2B}$  are their intrinsic transverse relaxation rates,  $\Delta H^\ddagger$  is the enthalpy of activation,  $E_A$  and  $E_B$  are the activation energies associated with relaxation rates of A and B, and the symbols labeled with 298 represent values of parameters at 298.15 K.  $1/T_{2A}$  and  $1/T_{2B}$  are governed by the quadrupolar mechanism and are proportional to  $\tau_R$ . The investigated complexes of paramagnetic lanthanides have dipolar and scalar contributions as well, which all are proportional to electronic relaxation rates, which are not very sensitive to temperature. Hence overall,  $1/T_{2A}$  and  $1/T_{2B}$  of these complexes decrease upon increase of the temperature.

The exchange of the carboxylate oxygens is slow for Lu- and Sc-DOTA and fast for La-DOTA under all conditions applied. If it is assumed that the chemical shift difference  $\Delta\omega_{AB}$  is about the same for these compounds, it can be concluded that  $\tau_M$  is larger for Lu and Sc

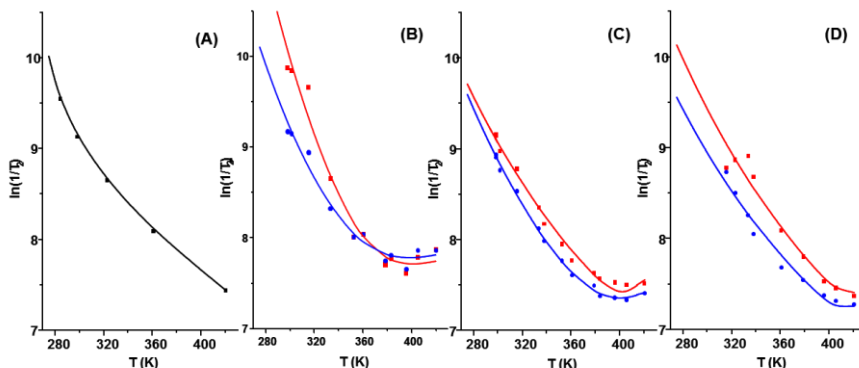


**Figure 2.6.** Transverse relaxation rates of the different Ln-DOTA complexes as function of the temperature at 18.8 T. Ln = La (A), Pr (B), Sm (C), Lu (D). The curves were calculated with the best-fit parameters (see Table 6) of fitting of the experimental data with eqs 2-4 (curve A) or eqs 1,3,4 (curves B-D), see text.

**Table 2.6.** Parameters obtained from least-squares fits  $^{17}\text{O}$  NMR transverse relaxation rates of carboxylate resonances of the various  $\text{Ln}(\text{DOTA})^-$  complexes at variable temperature and 18.8 T.

Ln	$\tau_{\text{M}}^{298}$ (s)	$\Delta H^\ddagger$ <sup>a</sup> (kJ·mol <sup>-1</sup> )	$1/T_{2,\text{A}}^{298}$ (10 <sup>3</sup> s <sup>-1</sup> )	$E_{\text{A}}$ (kJ·mol <sup>-1</sup> )	$1/T_{2,\text{B}}^{298}$ (10 <sup>3</sup> s <sup>-1</sup> )	$E_{\text{B}}$ (kJ·mol <sup>-1</sup> )
La	$(1.7 \pm 0.1) \times 10^{-5}$	73.51	$86 \pm 0.8^{\text{b}}$	$13.9 \pm 0.1^{\text{b}}$	$8.65 \pm 0.08^{\text{b}}$	$13.8 \pm 0.1^{\text{b}}$
Pr	$(1.9 \pm 0.2) \times 10^{-3}$	84.8	$23.0 \pm 2.1$	$36.0 \pm 2.7$	$10.2 \pm 0.9$	$25.6 \pm 2.6$
Sm	$(1.2 \pm 0.2) \times 10^{+2}$	94.3	$9.0 \pm 0.3$	$17.6 \pm 0.6$	$7.2 \pm 0.2$	$17.0 \pm 0.6$
Lu	$(3.9 \pm 1.6) \times 10^{+4}$	135.8	$12.9 \pm 1.4$	$19.3 \pm 1.6$	$8.0 \pm 0.9$	$16.7 \pm 1.6$

<sup>a</sup>Fixed during fitting. Value obtained from DFT computations. The weighted average of the various conformers of the Ln under study was used. The value for Pr was estimated by interpolation of those computed for the other lanthanides. <sup>b</sup>Fast exchange, value for averaged signal.

than for La. For the complexes with slow exchange, the observed relaxation rates initially decrease upon increase of the temperature, because under those conditions the decrease of the relaxation rates  $1/T_{2\text{A}}$  and  $1/T_{2\text{B}}$  dominates. At higher temperatures, the effect of the decrease of  $\tau_{\text{M}}$  gains in importance and then the observed relaxation rates start to increase again. The position of the minima in Figure 2.6 and the shape of the curves suggest that the  $\tau_{\text{M}}$  values of these complexes increase in the order Pr-DOTA < Sm-DOTA < Lu-DOTA.

Attempts to fit the observed transverse relaxation rates with eqs 1 and 2 and single-exponential Eyring type equations to deal with the temperature dependences of the intrinsic relaxation rates and  $\tau_{\text{M}}$  (see eqs 3 and 4) gave good fits, but unfortunately, the obtained best-fit parameters were meaningless because the parameters are strongly correlated and their standard deviations were larger than their values. However, if  $\Delta H^\ddagger$  was fixed at the values obtained from the DFT calculations, excellent fits were obtained. The best-fit-values are compiled in Table 2.6 and Figure 2.6 displays the curves calculated with them. For Sc-DOTA the resonances could only be separated by deconvolution, which resulted in inaccurate linewidths and therefore, these data were not included in the fittings. The results obtained from the fittings must be taken with some care i) since they are substantially affected by the  $\Delta H^\ddagger$  values fixed during the fitting procedure, and ii) the computed  $\Delta H^\ddagger$  values were obtained with a relatively crude computational approach, and thus they might be not very accurate. However, the large differences in the value of  $\tau_{\text{M}}^{298}$  among the lanthanides dramatically show the effect of the ionic radius on the rotation rate of the carboxylate function.

**Effect of addition of Co<sup>2+</sup>.** With the aim to change the NMR time scale of the carboxylate oxygen exchange of the diamagnetic Ln- and Sc-DOTA complexes by increasing  $\Delta\omega_{AB}$ , CoCl<sub>2</sub> was added stepwise to the samples. Because of the kinetic inertness of Ln- and Sc-DOTA complexes, transmetallation of the complexes with Co<sup>2+</sup> will be

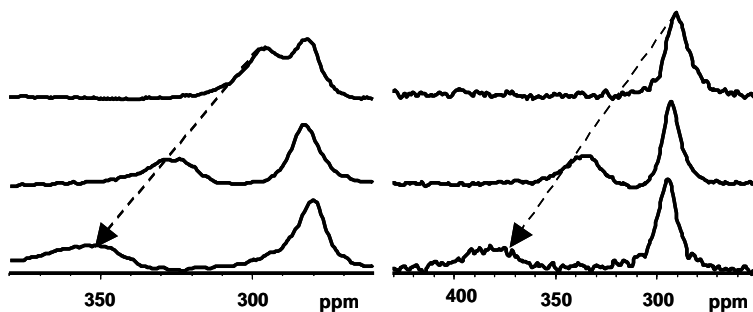


**Figure 2.7.** <sup>17</sup>O NMR spectra of Lu-DOTA (left) and Sc-DOTA (right) at 7T and 368 K taken after the addition of 0, 10 and 15 mol% of CoCl<sub>2</sub> (top to bottom, respectively). The signal with the largest Co<sup>2+</sup> induced shift and line broadening is assigned to the carboxylate oxygen that is not bound to Lu<sup>3+</sup> or Sc<sup>3+</sup>.

negligible. Co<sup>2+</sup> was selected because we expected that, due to its lower charge, it coordinates relatively weakly with carboxylate oxygens of Ln- and Sc-DOTA. The first portion of CoCl<sub>2</sub> was complexed by the small excess of free ligand ( $\leq 5$  mol %) present in the samples, as reflected by the disappearance of its resonance due to severe broadening. After that, the almost coinciding free carboxylate O-resonances of Lu- and Sc-DOTA showed an increasing chemical shift and linewidth with increase of the molar ratio Co<sup>2+</sup>/M-DOTA (M = Lu, Sc; see Figure 2.7), whereas the chemical shift and linewidth of the bound oxygen atoms were almost unaffected. These findings indicate that the exchange between the adduct of Co<sup>2+</sup> and M-DOTA and free M-DOTA (M = Lu, Sc) is rapid on the <sup>17</sup>O NMR time scale. For La-DOTA, however, a shift and broadening of the averaged carboxylate <sup>17</sup>O signal was observed, whereas the exchange between the La-bound and unbound carboxylate oxygen atoms remained fast on the <sup>17</sup>O NMR time scale upon addition of Co<sup>2+</sup>. The difference in behavior between La- and Lu- or Sc-DOTA in these experiments suggests that the exchange between the two oxygen atoms in each carboxylate group is much faster for La than for Lu and Sc,



which again is in agreement with the results of the DFT calculations and the  $\tau_M^{298}$  values reported in Table 2.6.

## Conclusions

DFT computations predict that the mechanism and the rate of rotation of carboxylate oxygens in complexes of DOTA with  $\text{Ln}^{3+}$  and  $\text{Sc}^{3+}$  ions are strongly dependent on the radius of the central metal ion. For the larger metal ions, the rotation takes place via a transition state in which the carboxylate function is bound to the metal ion in a nearly symmetrical bidentate fashion with Ln-O distances that are somewhat elongated compared to the reactant. In the complexes of the smaller metal ions ( $\text{Lu}^{3+}$ ,  $\text{Sc}^{3+}$ ), such a transition state would be sterically very crowded and then a pathway via decoordination of the carboxylate oxygen is preferred. The activation free energies computed for the rotation process increase along the lanthanide series from about 75 to 125 and 135  $\text{kJ}\cdot\text{mol}^{-1}$  for the SAP and TSAP isomers, respectively. Although the accuracy of these values remains uncertain and should be probably tested against high level ab initio calculations, our results are consistent with the results of a variable temperature  $^{17}\text{O}$  NMR study on these systems. Thanks to the relatively slow rotation of the carboxylate group and the increased shift dispersion in paramagnetic systems, separate resonances were observed for the  $\text{Ln}^{3+}$ -bound and free carboxylate oxygen nuclei, except in La-DOTA, where the exchange of these oxygen atoms was rapid on the NMR time scale.

The activation free energies for the presently studied carboxylate rotation process are considerably higher than that for the exchange between Ln-bound water and bulk water for  $[\text{Ln}(\text{DOTA})(\text{H}_2\text{O})]^-$  complexes and for the SAP/TSAP rearrangement. For example for  $[\text{Eu}(\text{DOTA})(\text{H}_2\text{O})]^-$ ,  $\Delta G_{306}^\ddagger$  has been determined to be about 35  $\text{kJ}\cdot\text{mol}^{-1}$  for the water exchange and 63  $\text{kJ}\cdot\text{mol}^{-1}$  for the conformational rearrangement.<sup>9,37</sup> Consequently, the corresponding rates are much faster than the rate of rotation of the carboxylate groups and it is very likely that these processes are taking place independently of each other.

## Experimental details

**Materials.** H<sub>4</sub>DOTA was obtained from Chematech, 21000 Dijon, France, CoCl<sub>2</sub>, ScCl<sub>3</sub>, and LnCl<sub>3</sub> (as hydrates) were purchased from Sigma-Aldrich, St. Louis, MO 63103, USA. These chemicals were used as obtained. Water was purified with a Milli-Q system.

### Synthesis of <sup>17</sup>O enriched H<sub>4</sub>DOTA and preparation of metal complexes thereof.

H<sub>4</sub>DOTA (1 g, 2.47 mmol) was stirred in 4 mL of water. After 10 min 1 mL of <sup>17</sup>O enriched water (10% <sup>17</sup>O) and 1 drop of concentrated HCl (36%) were added. The resulting slurry was heated at 90 °C for 18 h under stirring and then cooled to room temperature. Finally, the product was freeze dried to obtain the <sup>17</sup>O enriched H<sub>4</sub>DOTA as a white powder (920 mg, 2.28 mmol, 92%). The degree of enrichment was determined by ESI-MS. The <sup>1</sup>H and <sup>13</sup>C NMR spectra were identical to those of the starting material.

The metal complexes were prepared by mixing solutions of the <sup>17</sup>O enriched H<sub>4</sub>DOTA (120 mg, 0.29 mmol) in 3 mL of water and the appropriate metal chloride (0.26 mmol, 95 mol%) in 0.5 mL of water. The pH was maintained at 5 by adding NaOH (0.1 M) with a Metrohm Dosimeter 665. After the consumption of NaOH had stopped the solution was stirred for another 3 h and then freeze dried to result in the product as a powder. <sup>1</sup>H and <sup>13</sup>C NMR spectra of the complexes were identical with those of authentic samples of the known compounds, apart from the resonances of the small excess of free ligand (≤ 5 %). The number of Ln-DOTA complexes in the various samples was determined by quantitative <sup>1</sup>H NMR measured in the presence of weighted amounts of *tert*-butanol.

A typical sample for NMR measurements was prepared by dissolving 0.12 mmol of the concerning metal-DOTA complex in 0.5 mL of D<sub>2</sub>O. The pH was adjusted to 6.3 by adding either a DCl or a NaOD solution in D<sub>2</sub>O, followed by a filtration over a hydrophilic Nylon syringe filter (0.2 μm). For the measurements in 10 mm sapphire tubes, larger samples were prepared by dissolving 0.6 mmol of the compounds in 2 mL of D<sub>2</sub>O, adjusting the pH and filtering in the same way. Measurements with CoCl<sub>2</sub> were done at 300 MHz in 5 mm NMR tubes. The samples were prepared by adding portions of an aqueous CoCl<sub>2</sub> solution (0.12 mmol in 0.1 mL) to Ln(DOTA)- or Sc(DOTA)- samples.

**Physical methods.** NMR spectra were measured on a Bruker Avance 200, Varian Inova-Unity 300, Bruker Avance 400 or a Bruker Avance 800 spectrometer. On Avance 200 and

800 spectrometers, spectra were measured in the temperature range of 25-147 °C using closed 10 mm sapphire sample tubes under pressurized argon (~10 bar).<sup>37</sup> Peak positions in the <sup>17</sup>O NMR spectra were measured with respect to the resonance of the solvent (D<sub>2</sub>O). Linewidths and integrals of NMR signals were obtained by fitting Lorentzian functions to the experimental spectra using the NMRICMA program<sup>39</sup> for MATLAB. The adjustable parameters are the resonance frequency, intensity, line width, baseline, and phasing. All other fittings of the experimental data were performed using the computer program Micromath Scientist co version 2.0 (Salt Lake City, UT).

**Computational details.** All calculations were performed using hybrid DFT with the restricted B3LYP exchange-correlation functional,<sup>40,41</sup> and the Gaussian 09 package (Revision A.02).<sup>42</sup> On the grounds of previous investigations on related Ln<sup>3+</sup> complexes,<sup>18,43</sup> full geometry optimizations of the [Ln(DOTA)(H<sub>2</sub>O)]<sup>-</sup> (Ln = La, Nd, Sm, Tb or Ho) and [Ln(DOTA)]<sup>-</sup> (Ln = Tm or Lu) systems were performed in the gas phase by using the effective core potential (ECP) of Dolg *et al.* and the related [5s4p3d] GTO valence basis set for the lanthanides,<sup>44</sup> and the 6 31G(d) basis set for C, H, N and O atoms. This ECP includes 46+4fn electrons in the core, leaving the outermost 11 electrons to be treated explicitly. The use of large core ECPs has been justified by the fact that 4f orbitals do not significantly contribute to bonding due to their limited radial extension as compared to the 5d and 6s shells.<sup>45,46</sup> In the case of the [Sc(DOTA)]<sup>-</sup> system, the standard 6 31G(d) basis set was used for all atoms (including Sc). No symmetry constraints have been imposed during the optimizations. The default values for the integration grid (“fine”) and the SCF energy convergence criteria (10<sup>-6</sup>) were used. The stationary points found on the potential energy surfaces as a result of the geometry optimizations have been tested to represent energy minima rather than saddle points via frequency analysis. The relative free energies of the SAP and TSAP conformations were calculated at the same computational level and they include non-potential-energy contributions (zero-point energies and thermal terms) obtained through frequency analysis.

The exchange between coordinated and non-coordinated oxygen atoms of acetate groups of DOTA was investigated by means of the synchronous transit-guided quasi-Newton method.<sup>47,48</sup> The nature of the saddle points was characterized by frequency analysis. The free energy barriers include non-potential energy contributions obtained from frequency calculations. To evaluate the bulk solvent effects on the activation barriers, single point

energy calculations were performed in aqueous solution at all critical points on the geometries optimized in the gas phase. Solvent effects were evaluated by using the polarizable continuum model (PCM), in which the solute cavity is built as an envelope of spheres centered on atoms or atomic groups with appropriate radii. In particular, we used the integral equation formalism (IEFPCM) variant as implemented in Gaussian 09.<sup>49</sup>

## References

1. Desreux, J. F. *Inorg. Chem.* **1980**, 19, (5), 1319-1324.
2. Wang, X.; Jin, T.; Comblin, V.; Lopez-Mut, A.; Merciny, E.; Desreux, J. F. *Inorg. Chem.* **1992**, 31, (6), 1095-1099.
3. Merbach, A. E.; Tóth, É., *The chemistry of contrast agents in medical magnetic resonance imaging*. John Wiley & Sons, Ltd: Chichester (UK), 2001.
4. Caravan, P.; Ellison, J. J.; McMurry, T. J.; Lauffer, R. B. *Chemical Reviews* **1999**, 99, (9), 2293-2352.
5. Terreno, E.; Delli Castelli, D.; Viale, A.; Aime, S. *Chem. Rev.* **2010**, 110, (5), 3019-3042.
6. Aime, S.; Delli Castelli, D.; Geninatti Crich, S.; Gianolio, E.; Terreno, E. *Acc. Chem. Res.* **2009**, 42, (7), 822-831.
7. Caravan, P. *Chem. Soc. Rev.* **2006**, 35, (6), 512-523.
8. Aime, S.; Botta, M.; Ermondi, G. *Inorg. Chem.* **1992**, 31, (21), 4291-4299.
9. Aime, S.; Botta, M.; Fasano, M.; Marques, M. P. M.; Geraldes, C. F. G. C.; Pubanz, D.; Merbach, A. E. *Inorg. Chem.* **1997**, 36, (10), 2059-2068.
10. Hoeft, S.; Roth, K. *Chemische Berichte* **1993**, 126, (4), 869-873.
11. Jacques, V.; Desreux, J. F. *Inorg. Chem.* **1994**, 33, (18), 4048-4053.
12. Aime, S.; Barge, A.; Botta, M.; De Sousa, A. S.; Parker, D. *Angew. Chem. Int. Ed.* **1998**, 37, (19), 2673-2675.
13. Dunand, F. A.; Aime, S.; Merbach, A. E. *J. Am. Chem. Soc.* **2000**, 122, (7), 1506-1512.
14. Dunand, F. A.; Dickins, R. S.; Parker, D.; Merbach, A. E. *Chem. Eur. J.* **2001**, 7, (23), 5160-5167.
15. Woods, M.; Aime, S.; Botta, M.; Howard, J. A. K.; Moloney, J. M.; Navet, M.; Parker, D.; Port, M.; Rousseaux, O. *J. Am. Chem. Soc.* **2000**, 122, (40), 9781-9792.
16. Zhang, S.; Kovacs, Z.; Burgess, S.; Aime, S.; Terreno, E.; Sherry, A. D. *Chem. Eur. J.* **2001**, 7, (1), 288-296.
17. Powell, D. H.; Dhubhghaill, O. M. N.; Pubanz, D.; Helm, L.; Lebedev, Y. S.; Schlaepfer, W.; Merbach, A. E. *J. Am. Chem. Soc.* **1996**, 118, (39), 9333-9346.
18. Purgel, M. I.; Baranyai, Z.; de Blas, A. s.; Rodríguez-Blas, T.; Bányai, I. n.; Platas-Iglesias, C.; Tóth, I. *Inorg. Chem.* **2010**, 49, (9), 4370-4382.
19. Benetollo, F.; Bombieri, G.; Calabi, L.; Aime, S.; Botta, M. *Inorg. Chem.* **2002**, 42, (1), 148-157.
20. Mayer, F.; Platas-Iglesias, C.; Helm, L.; Peters, J. A.; Djanashvili, K. *Inorg. Chem.* **2011**, 51, (1), 170-178.
21. Seitz, M.; Oliver, A. G.; Raymond, K. N. *J. Am. Chem. Soc.* **2007**, 129, (36), 11153-11160.
22. Buzko, V.; Sukhno, I.; Buzko, M. *J. Mol. Struct.: THEOCHEM* **2009**, 894, (1-3), 75-79.
23. Heiberg, H.; Gropen, O.; Laerdahl, J. K.; Swang, O.; Wahlgren, U. *Theor. Chem. Acc.* **2003**, 110, (3), 118-125.
24. Cosentino, U.; Pitea, D.; Moro, G.; Barone, V.; Villa, A.; Muller, R. N.; Botteman, F. *Theor. Chem. Acc.* **2004**, 111, (2-6), 204-209.
25. Li, H.; Jensen, J. H. *J. Comput. Chem.* **2004**, 25, (12), 1449-1462.

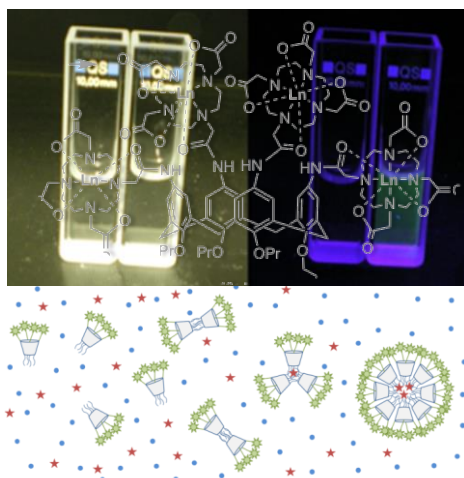
26. Tsushima, S.; Yang, T.; Mochizuki, Y.; Okamoto, Y. *Chem. Phys. Lett.* **2003**, 375, (1–2), 204-212.
27. Bryantsev, V. S.; Diallo, M. S.; Goddard III, W. A. *J. Phys. Chem. B* **2008**, 112, (32), 9709-9719.
28. Dinescu, A.; Clark, A. E. *J. Phys. Chem. A* **2008**, 112, (44), 11198-11206.
29. Kvamme, B.; Wander, M. C. F.; Clark, A. E. *Int. J. Quantum Chem.* **2009**, 109, (11), 2474-2481.
30. Gerothanassis, I. P. *Prog. Nucl. Magn. Reson. Spectrosc.* **2010**, 56, (2), 95-197.
31. Fussaro, L.; Casella G.; Bagno, A. *Chem. Eur. J.* **2015**, 21, 1955-1960.
32. Peters, J. A.; Huskens, J.; Raber, D. J. *Prog. Nucl. Magn. Reson. Spectrosc.* **1996**, 28, (3–4), 283-350.
33. Theodorou, V.; Troganis, A. N.; Gerothanassis, I. P. *Tetrahedron Lett.* **2004**, 45, (10), 2243-2245.
34. Leigh Jr, J. S. *J. Magn. Reson.* **1971**, 4, (3), 308-311.
35. McLaughlin, A. C.; Leigh Jr, J. S. *J. Magn. Res.* **1973**, 9, (2), 296-304.
36. Swift, T. J.; Connick, R. E. *J. Chem. Phys.* **1962**, 37, (2), 307-320.
37. Micskei, K.; Helm, L.; Brucher, E.; Merbach, A. E. *Inorg. Chem.* **1993**, 32, (18), 3844-3850.
38. Cusanelli, A.; Frey, U.; Richens, D. T.; Merbach, A. E. *J. Am. Chem. Soc.* **1996**, 118, (22), 5265-5271.
39. Helm, L. *NMRica*, 3.1.5; EPFL: Lausanne, Switzerland, 2003.
40. Becke, A. D. *J. Chem. Phys.* **1993**, 98, (7), 5648-5652.
41. Lee, C.; Yang, W.; Parr, R. G. *Phys. Rev. B* **1988**, 37, (2), 785-789.
42. Frisch, M. J.; Trucks, G. W.; Schlegel, H. B.; Scuseria, G. E.; Robb, M. A.; Cheeseman, J. R.; Scalmani, G.; Barone, V.; Mennucci, B.; Petersson, G. A.; Nakatsuji, H.; Caricato, M.; Li, X.; Hratchian, H. P.; Izmaylov, A. F.; Bloino, J.; Zheng, G.; Sonnenberg, J. L.; Hada, M.; Ehara, M.; Toyota, K.; Fukuda, R.; Hasegawa, J.; Ishida, M.; Nakajima, T.; Honda, Y.; Kitao, O.; Nakai, H.; Vreven, T.; Montgomery, J., J. A.; Peralta, J. E.; Ogliaro, F.; Bearpark, M.; Heyd, J. J.; Brothers, E.; Kudin, K. N.; Staroverov, V. N.; Kobayashi, R.; Normand, J.; Raghavachari, K.; Rendell, A.; Burant, J. C.; Iyengar, S. S.; Tomasi, J.; Cossi, M.; Rega, N.; Millam, N. J.; Klene, M.; Knox, J. E.; Cross, J. B.; Bakken, V.; Adamo, C.; Jaramillo, J.; Gomperts, R.; Stratmann, R. E.; Yazyev, O.; Austin, A. J.; Cammi, R.; Pomelli, C.; Ochterski, J. W.; Martin, R. L.; Morokuma, K.; Zakrzewski, V. G.; Voth, G. A.; Salvador, P.; Dannenberg, J. J.; Dapprich, S.; Daniels, A. D.; Farkas, Ö.; Foresman, J. B.; Ortiz, J. V.; Cioslowski, J.; Fox, D. J. *Gaussian 09*, Revision A.02; Gaussian, Inc., Wallingford CT, 2009.
43. Regueiro-Figueroa, M.; Esteban-Gómez, D.; de Blas, A.; Rodríguez-Blas, T.; Platas-Iglesias, C. *Eur. J. Inorg. Chem.* **2010**, 2010, (23), 3586-3595.
44. Dolg, M.; Stoll, H.; Savin, A.; Preuss, H. *Theoret. Chim. Acta* **1989**, 75, (3), 173-194.
45. Eisenstein, O.; Maron, L. *J. Organomet. Chem.* **2002**, 647, (1–2), 190-197.
46. Maron, L.; Eisenstein, O. *J. Phys. Chem. A* **2000**, 104, (30), 7140-7143.
47. Peng, C.; Ayala, P. Y.; Schlegel, H. B.; Frisch, M. J. *J. Comput. Chem.* **1996**, 17, (1), 49-56.
48. Peng, C. Y.; Schlegel, H. B. *Isr. J. Chem.* **1993**, 33, (4), 449-454.
49. Tomasi, J.; Mennucci, B.; Cammi, R. *Chem. Rev.* **2005**, 105, (8), 2999-3094.



---

# Luminescence Properties of Self-Aggregating Tb<sup>III</sup>-DOTA- Functionalized Calix[4]arenes

# 3



---

The contents of this chapter have been published in:

F. Mayer, S. Tiruvadi Krishnan, D.T. Schühle, S.V. Eliseeva, S. Petoud, É. Tóth, K. Djanashvili *Frontiers in Chemistry*, **2018**, *6*, 1-9



## Introduction

Calix[4]arenes were initially proposed as artificial enzyme mimics in the late 70s<sup>1</sup> and today represent versatile building blocks with potential for application in industrial, technical and biomedical fields, ranging from wastewater treatment<sup>2</sup> to medical imaging.<sup>3,4</sup> The multifunctional constitution of calix[4]arenes consists of four phenol moieties forming a cup-shaped structure with an upper and a lower rim. Functionalization of the rims can be done in accordance with the desired properties, including solubility, amphiphilicity, and metal complexation characteristics. The calixarene core is a synthetic backbone that ideally can play an active role in various applications. One example is represented by artificial ion-channels, where the hydrophobic channel-like cavity is of high importance for ion translocation through the membrane.<sup>5</sup> Enzyme mimics are also thought to benefit from this basket that resembles hydrophobic pockets in enzymes and serves for positioning of the substrate.<sup>6,7</sup> Despite those exciting examples, most often calix[4]arenes are simply used as platforms to attach the groups of interest in a predetermined spatial arrangement,<sup>8</sup> which downgrades the core to a mere steric support without further function. Especially, calix[4]arene derivatives intended for medical applications often lack active participation of the core structure itself.

We have been interested in designing imaging agents based on calix[4]arenes for a long time. In the context of contrast agent development for magnetic resonance imaging (MRI), the upper rim of the core structure was decorated with four DOTA (1,4,7,10-tetraazacyclododecane-1,4,7,10-tetraacetate) chelating ligands to provide stable complexation of paramagnetic Gd<sup>III</sup> ions. The Ln<sup>III</sup> complexes of these calix[4]arenes **1** and **2** (Figure 3.1) are amphiphilic molecules with a very polar upper rim and an apolar lower rim, tuneable depending on the alkylation of the phenolic OH-groups.

This amphiphilic nature confers them high water solubility due to micelle formation in polar solvents and also opens the possibility for labelling lipid bilayers. Complexes **1**<sup>9</sup> and **2**<sup>10</sup> exhibit high longitudinal proton relaxivities  $r_1$  (expressed in s<sup>-1</sup>mM<sup>-1</sup> of Gd<sup>III</sup>), especially when they form micelles, interact with human serum albumin or are incorporated in lipid bilayers.

The four chelating units of calix[4]arenes **1** and **2** can also be complexed with luminescent Ln<sup>III</sup> ions to design optical probes. Eventually, the combination of Gd<sup>III</sup> and

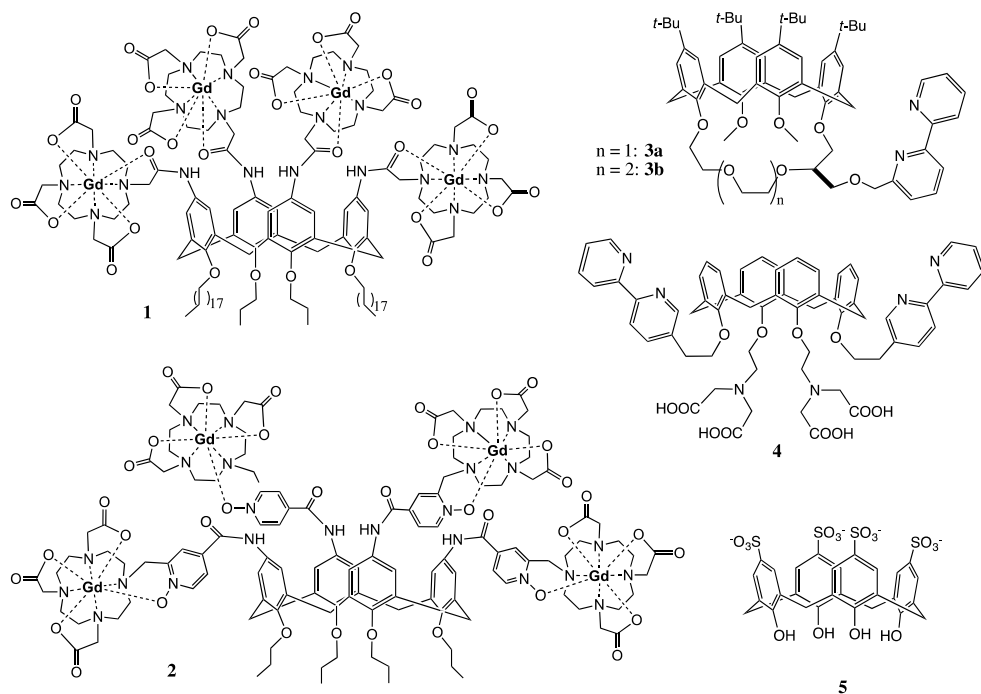


**Figure 3.1.** Examples of calix[4]arenes designed for imaging applications.

luminescent  $\text{Ln}^{\text{III}}$  complexes within the same molecular platform could lead to dual MRI/optical imaging probes. To use calix[4]arenes as optical imaging agents, the sensitisation of the  $\text{Ln}^{\text{III}}$  ions has to be ensured. Usually, this is done by surrounding the  $\text{Ln}^{\text{III}}$  ions with appropriate aromatic chromophoric units that are able to efficiently absorb the excitation energy and transfer it to the lanthanide ion.<sup>11</sup> An alternative strategy is to exploit the intermolecular energy transfer from an antenna incorporated in e.g. a micellar interior to the  $\text{Ln}^{\text{III}}$  ion ( $\text{Ln} = \text{Tb}$  or  $\text{Eu}$ ).<sup>12,13</sup>

A few literature examples indicate the potential of calix[4]arene derived compounds for optical imaging in combination with lanthanides.<sup>14,15</sup> Fischer et al. designed calix[4]arenes **3** and **4** (Figure 3.1) functionalized with bipyridyl moieties in the lower rim which participate in the complexation of  $\text{Ln}^{\text{III}}$  ions ( $\text{Ln}^{\text{III}} = \text{Eu}^{\text{III}}, \text{Tb}^{\text{III}}$ ) and are at the same time responsible for the excitation of the luminescent centre.<sup>16</sup> This architecture limits the number of lanthanide-binding sites to one, thus eliminating the great advantage of calix[4]arenes to deliver several active centres per molecule. In addition, the poor water solubility of these apolar compounds hampers thorough investigation of the luminescence properties and strongly limits biological

applicability. In another example, calix[4]arene **5** containing p-sulfonate groups was found to exhibit fluorescence upon complexation with Tb<sup>III</sup> at pH > 10.8.<sup>17</sup> The unexpected optical properties of this simple water soluble calix[4]arene were explained by a sandwich structure. The Tb<sup>III</sup> ion is between two complexing molecules which provide eight coordinating oxygens and push away potential hydration water molecules. However, none of these systems ensure sufficiently stable metal complexation appropriate for biological use.

In the objective of adapting our DOTA-derivative calix[4]arene platform designed for MRI purposes<sup>10</sup> to lanthanide luminescence, we have functionalized one site of the lower rim with a phthalimide chromophore while the three other sites bear propyl-groups (DOTA-calix-3OPr-OPht, Figure 3.2, **11a**). Keeping in mind the aggregation tendency of the functionalized calix[4]arenes and the literature examples showing that a direct coordination of the antenna to the luminescent centre is not always an absolute requirement,<sup>18</sup> we hypothesised that lower rim conjugation with a phthalimide moiety could be sufficient to sensitize Tb-luminescence. The aggregation and the photophysical properties of the Tb<sup>III</sup> complex have been studied in comparison to the Tb<sup>III</sup>-DOTA-calix-4OPr analogue (Figure 3.2, **12b**) with four propyl residues at the lower rim. We show that aggregation has a strong impact on the luminescence behaviour. In addition, our data provide a piece of evidence of the variability in the values of the critical micelle concentration depending on the experimental technique.

## Results and discussion

The synthetic routes of both compounds **12a** and **12b** are presented in Figure 3.2. In the first step, the hydroxyl groups on the lower rim of calix[4]arene **6** are alkylated to yield either three (**7a**) or four (**7b**) O-propyl functionalized calix[4]arenes. In the former case, the remaining OH-group was used for conjugation with propylphthalimide (**8a**). In the next step, the t-butyl groups on the upper rim were substituted with nitro-groups, which were subsequently reduced to amines to yield compounds **10a** and **10b**.<sup>19</sup> The following amide coupling with tris-tert-butoxycarbonylmethyl-10-carboxymethyl-1,4,7,10-tetraazacyclododecane resulted in ligands **11a** and **11b**, which after deprotection and purification by prep-

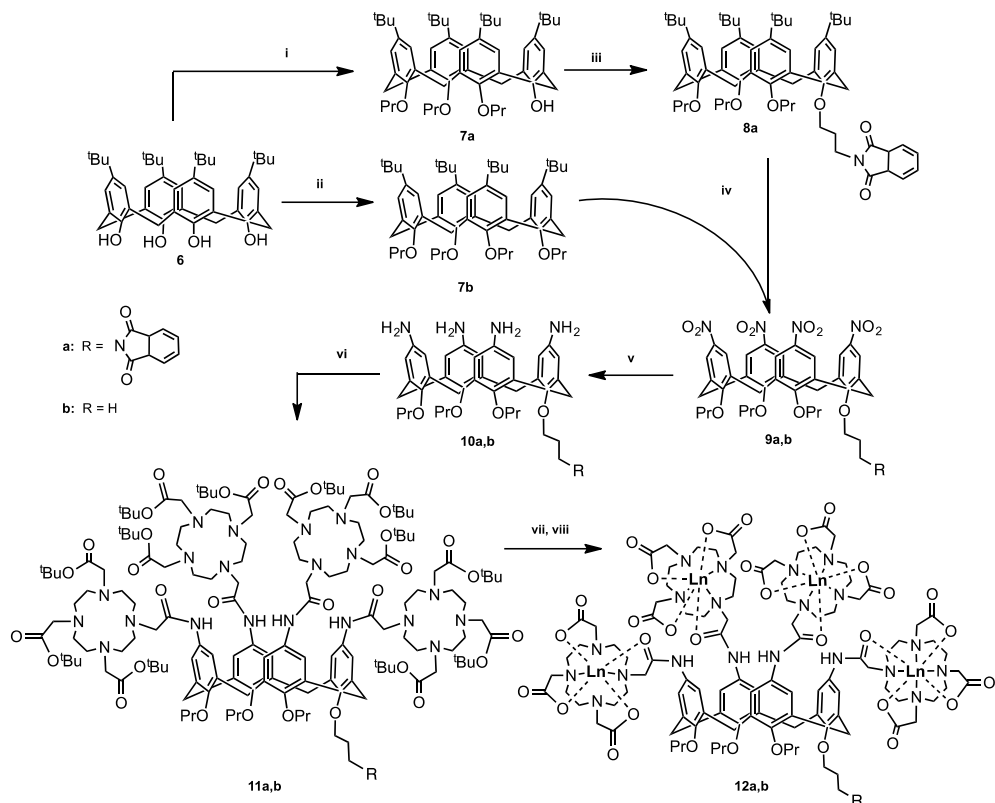


**Figure 3.2.** Synthetic pathway for compounds **12a** and **12b**: i) DMF, Ba(OH)<sub>2</sub>, BaO, propylbromide, RT, 1 day; ii) DMF, NaH, propylbromide, RT, 5 days (Gutsche and Lin, 1986); iii) DMF, NaH, N-(3-bromo)propylphthalimide, RT, 5 days;(Lalor et al., 2007) iv) a) CH<sub>2</sub>Cl<sub>2</sub>, AcOH, HNO<sub>3</sub>, 0 °C, 4 h;(Kelderman et al., 1992) v) MeOH, hydrazine, Raney-Ni, reflux, 6.5 h(Klimentová and Vojtíšek, 2007); vi) CH<sub>3</sub>CN, tris-*tert*-butoxycarbonylmethyl-10-carboxymethyl-1,4,7,10-tetraazacyclododecane (tris-*t*Bu-DOTA), Hünig's base, hydroxybenzotriazole, EDC, RT, 36h; vii) CH<sub>2</sub>Cl<sub>2</sub>, TFA; viii) TbCl<sub>3</sub>, H<sub>2</sub>O, pH 5.5.

HPLC were analyzed and complexed with Tb<sup>III</sup> ions. The obtained complexes **12a** and **12b** were characterized by ESI-HRMS (see Figure 3.3) and investigated with respect to their aggregation behaviour as well as their luminescent properties in a qualitative and quantitative ways.

In order to assess the role of the calix[4]arene skeleton and of the phthalimide chromophore, the luminescence excitation and emission spectra of Tb<sup>III</sup>-DOTA-calix-3OPr-Ophth (**12a**) and Tb<sup>III</sup>-DOTA-calix-4Opr (**12b**) were recorded and compared to those of Tb<sup>III</sup>-DOTA. Both Tb-**12a** and Tb-**12b** under excitation at 290 nm exhibit characteristic green

emission with four main bands due to  $^5D_4 \rightarrow ^7F_J$  ( $J = 6-3$ ) transitions, while the reference compound Tb<sup>III</sup>-DOTA under the same experimental conditions did not show detectable luminescence signal (Figures 3.4A and B). Upon monitoring emission at 545 nm excitation spectra of both Tb-**12a** and Tb-**12b** present broad bands in the UV range up to 315 nm. On the other hand, Tb<sup>III</sup>-DOTA does not exhibit pronounced transitions in this range. Therefore, in Tb-**12a** and Tb-**12b** characteristic green Tb<sup>III</sup>-emission could be sensitized through “antenna effect” via organic ligands, i.e. functionalized calix[4]arene cores. Interestingly, the maximum luminescence intensity of the two calix[4]arene-complexes shows a dramatically different variation with increasing concentration of the solutions. At concentrations up to approximately 0.1 mM, there is no difference in their luminescence intensities, which remain equally strong for both compounds with a linear correlation to the concentration (Figure 3.4C and 3.5 right).

Upon further increase of the concentration, the luminescence enhancement becomes non-linear. At 1 mM concentration, the emission intensity is two times higher for Tb-**12b** compared to Tb-**12a**. While the luminescence intensity of Tb-**12b** is still increasing above this concentration, that of Tb-**12a** goes through a maximum at 0.5 mM and then slightly decreases. Likewise, a maximum luminescence intensity is found for Tb-**12b** above the concentration of 5 mM (Figure 3.5 right).

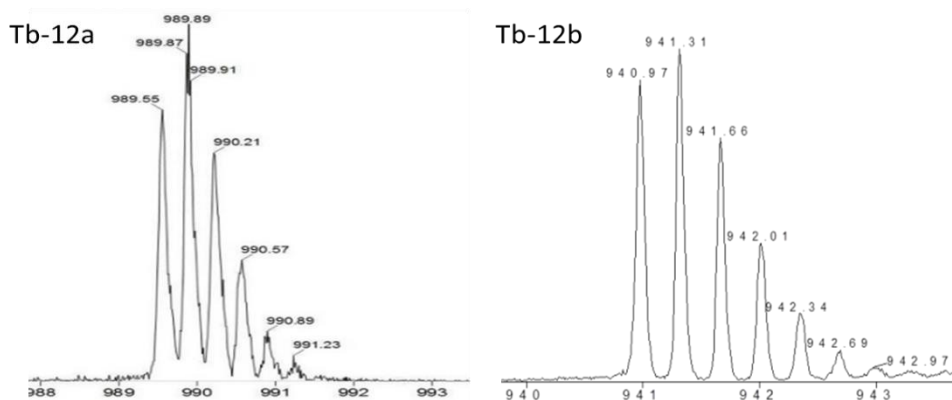


**Figure 3.3.** ESI-HRMS of Tb-12a (left) and Tb-12b (right). Expansion of the  $[M+3H]^{3+}$  peak to show the isotopic pattern of Tb.

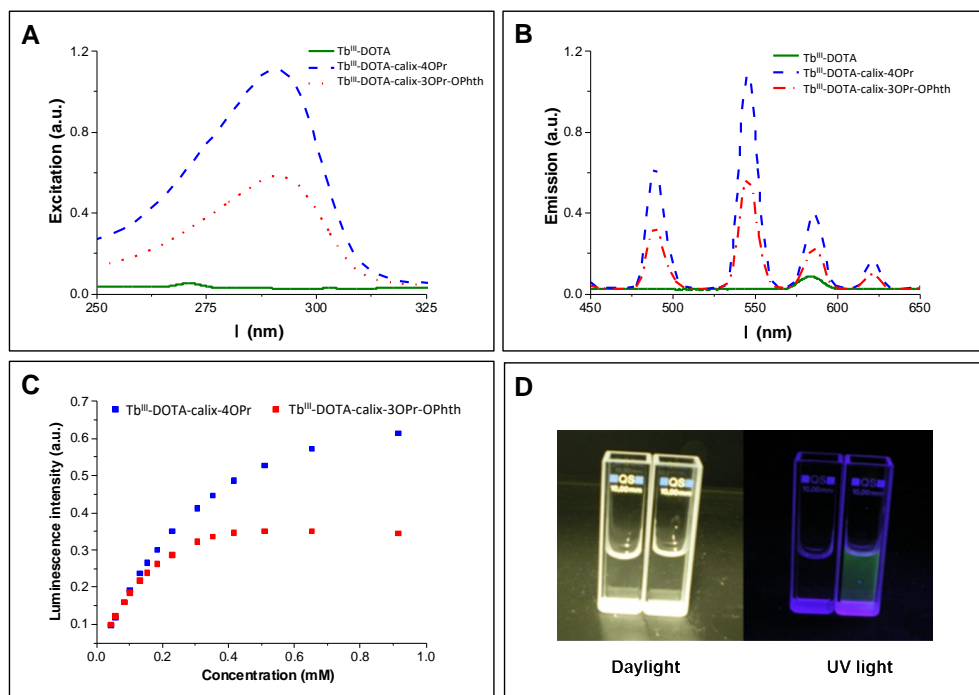


**Figure 3.4.** (A) Excitation ( $\lambda_{Em} = 545$  nm) and (B) emission ( $\lambda_{Ex} = 290$  nm) spectra of Tb<sup>III</sup>-DOTA, Tb-12a and Tb-12b at a Tb<sup>III</sup> concentration of 3.68 mM (corresponding to a calix[4]arene concentration of 0.92 mM). The two little signals at 272 nm (excitation) and 580 nm (emission) in the Tb<sup>III</sup>-DOTA spectra are artefacts from light scattering (double wavelength of excitation); (C) The dependence of relative luminescence intensities normalized to the same initial value vs the concentration of Tb-12a and Tb-12b; (D) Photographic images of Tb<sup>III</sup>-DOTA (left cuvette) and Tb-12a (right cuvette) under daylight and UV-irradiation.

To further quantify the photophysical properties, the excitation and emission spectra of Tb<sup>III</sup>-complexes of calix[4]arenes **12a** and **12b** were acquired in the solid state and at different concentrations in solution (Figure 3.6 right and Table 3.1). It should be noted that in the emission spectra of **12a** and **12b** the crystal-field splitting of Tb<sup>III</sup>  $^5D_4 \rightarrow ^7F_J$  ( $J = 6-3$ ) transitions is very similar for the samples in the solid state and solutions of different concentrations reflecting indirectly that the coordination environment around the Tb<sup>III</sup> ions remains the same upon such variations. The absolute quantum yields upon ligands excitation ( $Q_{Tb}^l$ ) and observed luminescence lifetimes ( $\tau_{obs}$ ) upon monitoring Tb<sup>III</sup> emission at 545 nm were also determined (Table 3.1). When comparing the values of  $\tau_{obs}$  and  $Q_{Tb}^l$  for Tb-12a and Tb-12b in solution, the presence of the phthalimide chromophore in the molecule has

essentially no effect on these parameters. This can be likely rationalized by the fact that the distance between the phthalimide and the Tb<sup>III</sup> centre is too long (> 15 Å) for an efficient energy transfer.<sup>20</sup> In contrast, in amorphous solid state the orientation of the molecules is random and the phthalimide units can be located closer to the Tb<sup>III</sup>-DOTA moieties, making non-covalent energy transfer and Tb<sup>III</sup> sensitization through this way possible.<sup>21</sup> Quantum yield values of Tb-**12a** and Tb-**12b** in the solid state are higher by 7.5 and 2.7 times, respectively, compared to these in 0.2 mM solutions, while lifetimes are lower by 25-30 %. Such behaviour points out that in the solid state non-radiative processes are minimized and/or sensitization efficiencies are improved. Higher increase of the  $Q_{Tb}^L$  value in the case of Tb-**12a** compared to the Tb-**12b** might be caused by an appearance of an additional sensitization pathway. Indeed, if we assume that the main energy transfer mechanism is of Förster type (dipole-dipole), the sensitization efficiency depends significantly on distance and is proportional to  $(r_{Tb-L})^{-6}$ . Thus, small changes in the distance between the chromophore and Tb<sup>III</sup> ion may have significant effects on the sensitization efficiency. This is also reflected in 3.1-times higher quantum yield value for Tb-**12a** compared to Tb-**12b** while observed luminescence lifetimes are the same for both complexes (Table 3.1). Moreover, slight broadening and red-shifting of the excitation band is observed for Tb-**12a** vs Tb-**12b** that can indicate that other lower-energy levels are involved in the sensitization of the former complex (Figure 3.6, left). Since this extra shoulder, only present in the solid-state excitation spectrum, overlaps with one of the UV-absorption peaks of the phthalimide moiety (Figure 3.7), it may indicate that in the solid state the phthalimide group can indeed participate in the sensitisation

**Table 3.1.** Photo-physical parameters of Tb<sup>III</sup> complexes in the solid state and aqueous solutions at 298 K.<sup>a</sup>

Compound	State/Solvent	c[mM]	$\tau_{obs}$ [ms]	$Q_{Tb}^L$ [%]
Tb- <b>12a</b>	Solid	-	1.2(1) <sup>b</sup>	5.87(9)
	H <sub>2</sub> O	0.04	1.52(1)	0.78(7)
		0.2	1.51(1)	0.65(1)
		2	0.83(5)	0.51(2)
Tb- <b>12b</b>	Solid	-	1.2(1) <sup>b</sup>	1.89(3)
	H <sub>2</sub> O	0.2	1.6(1)	0.71(3)
		2	0.79(5)	0.38(6)

<sup>a</sup>Under excitation at 300 nm. Standard deviations ( $2\sigma$ ) are given between parentheses; Estimated relative errors:  $\tau_{obs}$ ,  $\pm 5\%$ ;  $Q_{Tb}^L$ ,  $\pm 10\%$ . <sup>b</sup>The longest values are presented. Luminescence decay curves were best fitted by biexponential functions, the impact of the second short-lived lifetime value (0.17-0.22 ms) was only 5-6%.

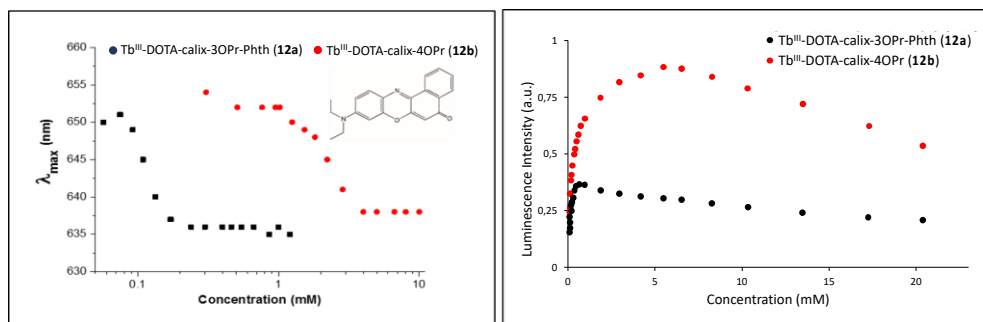


**Figure 3.5.** Left: Determination of the *cmc* for Tb-12a (black) and Tb-12b (red) via the fluorescence emission wavelength of Nile red ( $\lambda_{\text{ex}}=550$  nm). Right: Luminescence intensity of Tb-12a and Tb-12b at 545nm in dependence of the concentration.

of the Tb<sup>III</sup> luminescence. In addition, the quantum yield values confirm the trend that was observed qualitatively for solutions with different concentrations (Figure 3.4C vs Table 3.1): they increase upon dilution evidencing a non-linear correlation between the luminescence intensity and the concentration of the investigated compounds. Concentration of the solutions has also an effect on luminescence lifetimes. It should be noted here that for all solutions luminescence decay curves could be best fitted by mono-exponential functions reflecting the presence of only one type of emissive Tb<sup>III</sup>-containing species. The values of  $\tau_{\text{obs}}$  increase by 1.8-2.0 times when going from 2 mM to 0.2 mM solutions, i.e., following the same trend as absolute quantum yield values.

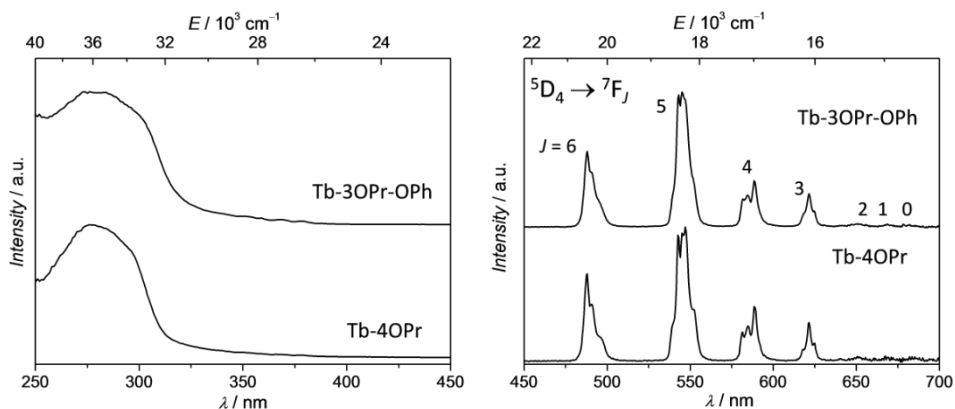


**Figure 3.6.** Left: Excitation spectra of Tb-12a (up) and Tb-12b (down) determined at the maximum Tb-emission ( $\lambda_{\text{em}}=545$  nm); Right: Emission spectra of the Tb compounds after excitation at  $\lambda_{\text{ex}}=300$  nm. All spectra were taken from solid state materials at room temperature.



To get a hint about the possible reasons of such changes of luminescent parameters, we have investigated the aggregation of the complexes in details. It has been previously described that the DOTA-functionalized calix[4]arene (Gd-**12b**) is highly amphiphilic and tends to aggregate in aqueous solution. At concentrations above 0.21 mM, they form micelles with a hydrodynamic radius of 2.2 nm and a narrow size distribution.<sup>9</sup> This critical micelle concentration (cmc) was determined for the Gd<sup>III</sup> complex by measuring the water proton relaxation rates as a function of the concentration.

In the current study, the aggregation was demonstrated by using Nile red, a dye exhibiting fluorescence changes in the emission maximum upon changes in the chemical environment. In the samples containing Nile red and increasing concentrations of the Tb<sup>III</sup> complexes **12a** and **12b**, the fluorescence emissions undergo strong blue-shifts and intensity increase, which can be associated with a decreasing hydrophilicity and polarity of the environment (Figure 3.5). Indeed, as the amphiphilic calix[4]arene complexes aggregate to micelles, the Nile red will enter the internal micellar core and will experience a more hydrophobic environment. From this experiment, the critical micelle concentrations of Tb<sup>III</sup>-DOTA-calix-3OPr-OPht (Tb-**12a**) and Tb<sup>III</sup>-DOTA-calix-4OPr (Tb-**12b**) were determined to be 0.12 and 2.3 mM, respectively (Figure 3.5 left). Obviously, the presence of phthalimide dramatically increases the hydrophobicity of the lower rim forcing the molecules to aggregate at lower concentrations and thus leads to a lower cmc. Interestingly, the determined cmc values correlate nicely with the maxima of the concentration dependent luminescence

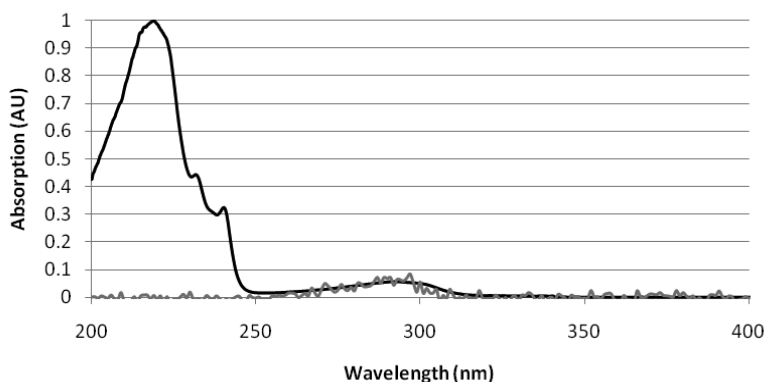


**Figure 3.7.** UV/Vis absorption spectrum of N-(3-bromopropyl) phthalimide (black) and the excitation spectrum of Tb-**12a** (grey) in solid state at room temperature ( $\lambda_{em}=540$  nm).

intensities (Figure 3.5), which are around 0.35 and 1.6 mM for Tb-**12a** and Tb-**12b**, respectively. This evidences that aggregation of the calix[4]arenes leads to a significant decrease in the intensity of Tb<sup>III</sup> luminescence. As the aromatic systems come closer to each other, non-radiative energy transfer from the excited  $\pi$ -systems becomes more likely which reduces luminescence quantum yields of the aggregated complexes. As a result, decreased quantum yields and shorter luminescence lifetimes are observed.

Surprisingly, the cmc value previously determined by relaxometric measurements for the Gd-**12b** analogue (0.21 mM) is significantly lower than cmc found in the Nile red experiment for Tb-**12b** (2.3 mM). It is very unlikely that this is due to the different ions complexed in the DOTA chelates, as lanthanides in general have very similar chemical properties. Furthermore, Gd and Tb are neighbours in the lanthanide series thus have similar ionic radii (difference  $\sim 0.1$  Å) and identical charge. The almost one order of magnitude difference in *cmc* can rather be explained by the different experimental methods applied for its determination. The relaxometric method used in the case of the paramagnetic analogue Gd<sup>III</sup>-**12b** is based on the effect of the rotational motion on the  $r_1$  relaxivity (longitudinal relaxation rate expressed in  $\text{mM}^{-1}\text{s}^{-1}$  of Gd<sup>III</sup>). Indeed, at medium fields, the relaxivity increases with the increasing rotational correlation time,  $\tau_R$  (slower motion) of the complex. While  $\tau_R$  already changes when as few as two molecules start interacting (Figure

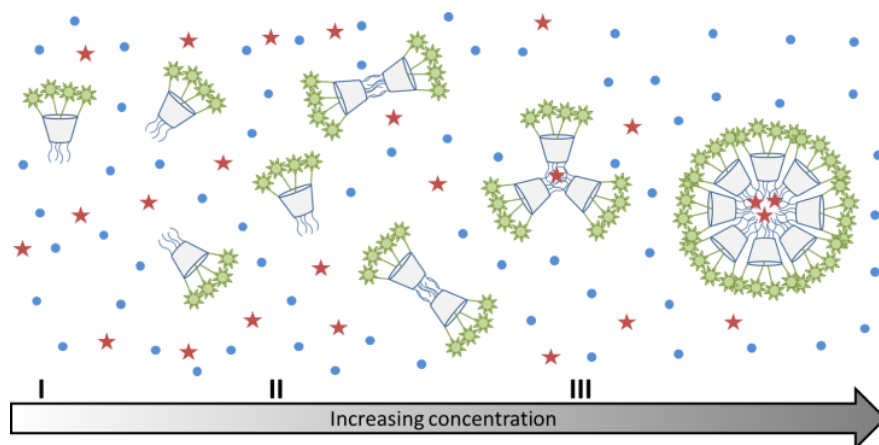


**Figure 3.8.** Schematic representation of the aggregation behavior of calix[4]arenes **12a** and **12b** with increasing concentration. The red stars indicate the location of Nile red, which can only enter the micelles, when there is a sufficiently large hydrophobic space.

3.8, II), the creation of noticeable hydrophobic compartments in micelles leading to an observable change in the fluorescence of the dye only starts at a higher degree of aggregation, when several amphiphilic molecules aggregate (Figure 3.8, III). Therefore, the *cmc* determined by the fluorescence method using Nile red is significantly higher than the one obtained via relaxivity measurements. Previous studies have already pointed out that the *cmc* value obtained can be dependent on the nature of the physical parameter monitored to assess the aggregation and that pre-micellar aggregation is often responsible for anomalies of various physical parameters.<sup>22,23</sup>

It is interesting to note that the concentration dependent luminescence intensities of Tb-**12b** (Figure 3.4C and 3.5 right) start to show a deviation from linearity at ~0.25 mM concentration, which corresponds to the *cmc* determined from the relaxivity method for the Gd<sup>III</sup> analogue. These results nicely demonstrate that micelle formation is not a sharp transition, but it expands over a concentration range that might cover more than an order of magnitude. As the various techniques used to determine the critical micelle concentration sense different physical parameters, they might lead to method-dependent *cmc* values.

Upon aggregation of the functionalized calix[4]arenes, the hydrophilic Tb<sup>III</sup>-DOTA moieties on the upper rim will always face the aqueous phase. The lifetimes observed for the aggregated state (0.83 and 0.79 ms) are smaller than those measured for the monomers (1.51 and 1.60 ms) of **12a** and **12b**, respectively. This points to a better protection of the Tb<sup>III</sup> ion from non-radiative deactivations in the case of the monomers. An increase of Tb-luminescence lifetimes occurs upon exclusion of water molecules from the first coordination sphere of the metal ion.<sup>24,25</sup> In our case, a possible explanation of the shortening of luminescence lifetimes found for the micellar Tb<sup>III</sup>-DOTA-functionalized calix[4]arenes could be an enhanced cross-relaxation between Tb<sup>III</sup>-ions and the formation of a more defined second coordination sphere around the micelle consisting of water molecules clustered via hydrogen bonds.

## Conclusions

In summary, we have synthesized the first luminescent lanthanide complex based on a calix[4]arene platform with sufficient stability due to the presence of four DOTA chelating units for potential biological use. We have evidenced for this prototype Tb<sup>III</sup> probe that the calix[4]arene backbone is actively participating to the excitation process of the Tb<sup>III</sup>-centred luminescence, while the chromophore introduced on the rim opposite to the lanthanide chelate is localized too far to provide efficient sensitization. The substitution pattern of the lower rim dictates the aggregation phenomena observed in aqueous solution and can be exploited to tailor the physical-chemical properties of the compound. This micellar aggregation of the calix[4]arene derivatives has a strong impact on their luminescence properties. Upon increasing the complex concentration, the luminescence intensities linearly increase up to the range where micellar aggregation starts to occur, and then they decline. Taking into account these peculiar properties, the future perspectives of the described systems may be based on the complexation of both luminescent Ln<sup>III</sup> and paramagnetic Gd<sup>III</sup> ions within the same molecule. This in turn, could yield dual MR/optical probes in a straightforward manner rendering the calix[4]arene backbone a valuable building block for the design of imaging probes.

## Experimental details

### General

All reagents and anhydrous solvents used during the synthesis were of commercial quality. 5,11,17,23-Tetra-(*t*-butyl)-25-hydroxy-26,27,28-tripropoxy-calix[4]arene (**6**) was prepared according to the literature (Gutsche and Iqbal, 1990). The lower rim of the calix[4]arene backbone was modified in accordance to the described procedures for the propylation (**7a,b**) of the hydroxylic groups,<sup>26</sup> as well as condensation of one of the hydroxyls (**8a**) with *N*-(3-bromo)propylphthalimide.<sup>19</sup> The steps, preceding the final conjugation with the DOTA-units<sup>9</sup> (included nitration (**9a,b**) of the upper rim of the calix[4]arene backbone<sup>27</sup> followed by the reduction (**10a,b**) of the nitro groups to the amines.<sup>28</sup> <sup>1</sup>H NMR spectra were recorded at 25 °C on Bruker Avance-400 spectrometer operating at 400.13 MHz and analyzed using Bruker™ TopSpin 2.1 software. The chemical shifts are reported in δ (ppm) using

tetramethylsilane (TMS) as an internal reference. Ultra-filtration was performed with a Millipore stirred cell using an Amicon cellulose acetate membrane. All HPLC measurements were carried out on a Shimadzu LC-20 system consisting out of an LC-20AT pump, Sil-20A HT autosampler, CTO-20AC column oven, SPD-M20A PDA detector, CBM-20A controller and a Waters Fraction Collector III; data processing was carried out using Shimadzu Lab Solutions. Both analytical and preparative methods were carried out operating at 40 °C using eluents A: H<sub>2</sub>O (95%), AcCN (5%), TFA (0.1%) and B: H<sub>2</sub>O (5%), AcCN (95%), TFA (0.1%). Mobile phase gradient started with 75% A and 25% B, after 18 min followed by a change linear to 58% A and 42% B, after 2 min a change linear to 100% B, which was hold for 0.5 min and then chanced back to starting conditions stabilized for 3.5 min. Analytical measurements used a Waters Xterra 4.6×150 mm column and an injection volume of 1 µL, flow was 1 mL/min. Preparative HPLC was performed using Xbridge™ PrepShield RP18-OBD C18-19×150 mm column. Mass spectrometry analysis was done with electron spray ionization technique on Waters Qtof Premier MS using a NE-1000 syringe pump for direct infusion; data processing was carried out using Waters Masslynx. Qualitative luminescence measurements were done on a Jasco J815 CD spectrometer using 100 µL of sample in a 3×3 mm quartz cuvette. UV absorption spectra were measured on a UV2401 PC Shimadzu spectrometer. For quantitative luminescence measurements, the samples (either powders or solutions in Milli-Q water at concentration 2, 0.2 and 0.04 mM) were placed into 2.4 mm quartz capillaries and measured on a Horiba-Jobin-Yvon Fluorolog 3 spectrofluorimeter equipped with visible (220-800 nm, photon-counting unit R928P) and NIR (950-1450 nm, photon-counting units H10330-45 from Hamamatsu or DSS-IGA020L Jobin-Yvon solid-state InGaAs detector, cooled to 77K) detectors. All spectra were corrected for the instrumental functions. Luminescence lifetimes of Tb<sup>III</sup>-complexes were determined under excitation at 300 nm provided by a Xenon flash lamp monitoring the signal at 545 nm (<sup>5</sup>D<sub>4</sub>→<sup>7</sup>F<sub>5</sub> transition). Quantum yields were measured according to an absolute method using an integration sphere (GMP SA). Each sample was measured several times under slightly different experimental conditions. Estimated experimental error for quantum yields determination is 10%. Nile red (NR) fluorescence measurements were performed on a Jasco J-815 CD spectrometer. The temperature was controlled using a Jasco PFD 4252/15 Peltier temperature unit. All samples contained Nile red in 2 µM concentrations and were excited at

550 nm. The maximum Nile red emission wavelength ( $\lambda_{\text{max}}$ ) was determined as a function of the calix[4]arene concentration.

### Synthesis

General procedure for the amide coupling of the amino-calix[4]arenes (10a,b) to tris-1,4,7-tert-butoxycarbonylmethyl-10-carboxymethyl-1,4,7,10-tetraazacyclododecane (tris-t-Bu-DOTA): to a suspension of EDC (2.2 mmol), HOBt (2.2 mmol), and tris-t-butyl-DOTA (2.2 mmol) in 20 mL DMF 1.1 mL dry DIPEA was added under N<sub>2</sub> atmosphere and the resulting mixture was stirred for 20 min. A solution of the corresponding calix[4]arene (170  $\mu\text{mol}$ ) in 5 mL DMF was added and the reaction mixture was stirred for 2 days before removing the solvent in vacuo. The remaining solid was dissolved in CH<sub>2</sub>Cl<sub>2</sub> (50 mL), washed 2 $\times$  with brine, 1 $\times$  with 0.1N NaOH, and then with water until the pH of the aqueous phase was neutral. The organic phase was dried over Na<sub>2</sub>SO<sub>4</sub> and the solvent was evaporated. The crude products 11a and 11b were purified from EtOH by ultrafiltration over a 1 kDa membrane with the yield of 80% (410 mg) and 69% (336 mg), respectively.

5,11,17,23-Tetrakis(tris-4,7,10-t-butoxycarbonylmethyl-1,4,7,10-tetraazacyclododec-1-yl-acetamidyl)-25,26,27-tripropoxy-28-phthalimidopropoxycalix[4]arene (11a): <sup>1</sup>H-NMR (300 MHz, DMSO-d<sub>6</sub>, 100 °C):  $\delta$  = 0.98 (12 H, t,  $J$  = 5.2 Hz, CH<sub>3</sub>), 1.40, 1.46 (108 H, 2 s, t-Bu), 1.88 (8 H, sext,  $J$  = 5.2 Hz, CH<sub>2</sub>CH<sub>3</sub>), 2.74 – 3.30 (100 H, N-CH<sub>2</sub>CO, N-CH<sub>2</sub>-CH<sub>2</sub>-N, Ar-CH<sub>2</sub>-Ar), 3.87 (8H, t,  $J$  = 5.2 Hz, O-CH<sub>2</sub>), 4.43 (4 H, d,  $J$  = 9.9 Hz, Ar-CH<sub>2</sub>-Ar), 6.86 (8 H, brs, Ar-H), 9.27 (4 H, brs, NH). ESI-HRMS: calc.:  $m/z$  = 755.4765 (M+4H)<sup>4+</sup>, found: 755.4870.

5,11,17,23-Tetrakis(tris-4,7,10-tert-butoxycarbonylmethyl-1,4,7,10-tetraazacyclododec-1-yl-acetamidyl)-25,26,27,28-tetrapropoxycalix[4]arene (11b): <sup>1</sup>H-NMR (300 MHz, DMSO-d<sub>6</sub>, 100 °C):  $\delta$  = 0.98 (12 H, t,  $J$  = 5.2 Hz, CH<sub>3</sub>), 1.42, 1.46 (108 H, 2 s, t-Bu), 1.88 (8 H, sext,  $J$  = 5.2 Hz, CH<sub>2</sub>CH<sub>3</sub>), 2.74 – 3.30 (100 H, N-CH<sub>2</sub>CO, N-CH<sub>2</sub>-CH<sub>2</sub>-N, Ar-CH<sub>2</sub>-Ar), 3.87 (8H, t,  $J$  = 5.2 Hz, O-CH<sub>2</sub>), 4.43 (4 H, d,  $J$  = 9.9 Hz, Ar-CH<sub>2</sub>-Ar), 6.86 (8 H, br s, Ar-H), 9.27 (4 H, brs, NH). ESI-HRMS: calc.:  $m/z$  = 718.7185 (M+4H)<sup>4+</sup>, found: 718.7282.

General procedure for the deprotection of the t-Bu-DOTA-calix[4]arenes: the t-Bu protected calix[4]arene (150  $\mu\text{mol}$ ) was dissolved in CH<sub>2</sub>Cl<sub>2</sub> (10 mL) and TFA (10 mL) was added slowly. The reaction mixture was stirred at ambient temperature overnight and subsequently the solvents were removed in vacuum. The obtained solid was re-dissolved in

1 mL of water and freeze-dried to obtain the product as a yellow fluffy powder. The yield was not determined due to the fact that there were still TFA salts in the product, which did not interfere with the next step of the synthesis and could be removed during the purification step of the final product (see below).

5,11,17,23-Tetrakis(tris-4,7,10-carboxymethyl-1,4,7,10-tetraazacyclododec-1-yl-acetamidyl)-25,26,27-tripropoxy-28-phthalimidopropoxycalix[4]arene:  $^1\text{H-NMR}$  (300 MHz, DMSO- $d_6$ , 100 °C):  $\delta$  = 0.89 (12 H, t,  $J$  = 6.9 Hz,  $\text{CH}_3$ ), 1.80 (8 H, sext,  $J$  = 6.9 Hz,  $\text{CH}_2\text{CH}_3$ ), 3.01-3.61 (100 H, N- $\text{CH}_2\text{CO}$ , N- $\text{CH}_2\text{-CH}_2\text{-N}$ , Ar- $\text{CH}_2\text{-Ar}$ ), 3.76 (8H, t,  $J$  = 6.9 Hz, O- $\text{CH}_2$ ), 4.32 (4 H, d,  $J$  = 12.3 Hz, Ar- $\text{CH}_2\text{-Ar}$ ), 6.91 (8 H, brs, Ar-H), 9.53 (4 H, brs, NH).

5,11,17,23-Tetrakis(tris-4,7,10-carboxymethyl-1,4,7,10-tetraazacyclododec-1-yl-acetamidyl)-25,26,27,28-tetrapropoxycalix[4]arene:  $^1\text{H-NMR}$  (300 MHz, DMSO- $d_6$ , 100 °C):  $\delta$  = 0.89 (12 H, t,  $J$  = 6.9 Hz,  $\text{CH}_3$ ), 1.80 (8 H, sext,  $J$  = 6.9 Hz,  $\text{CH}_2\text{CH}_3$ ), 3.01-3.61 (100 H, N- $\text{CH}_2\text{CO}$ , N- $\text{CH}_2\text{-CH}_2\text{-N}$ , Ar- $\text{CH}_2\text{-Ar}$ ), 3.76 (8H, t,  $J$  = 6.9 Hz, O- $\text{CH}_2$ ), 4.32 (4 H, d,  $J$  = 12.3 Hz, Ar- $\text{CH}_2\text{-Ar}$ ), 6.91 (8 H, brs, Ar-H), 9.53 (4 H, brs, NH).

General procedure for the complexation of  $\text{Tb}^{\text{III}}$ -ions in the DOTA-functionalized calix[4]arenes (**12a,b**): the ligands (150  $\mu\text{mol}$ ) obtained after the deprotection of t-Bu groups were dissolved in water (5 mL) and the pH was adjusted to 5.5 by the addition of 1M NaOH. Then the  $\text{TbCl}_3$  (660  $\mu\text{mol}$ ) was added as an aqueous solution and the pH was kept constant using Metrohm Dosimeter 665. After the consumption of NaOH stopped, the solution was stirred overnight and then freeze-dried to result in the crude product that was purified by prep-HPLC. Due to the paramagnetic nature of the  $\text{Tb}^{\text{III}}$  ions, no NMR investigations of the products were possible, therefore MS spectra were taken and compared to the predicted isotopic patterns of the compounds, which were found in a good agreement with the experimental values (Figure 3.3).

$\text{Tb}^{\text{III}}$ -complex of 5,11,17,23-tetrakis(tris-4,7,10-carboxymethyl-1,4,7,10-tetraazacyclododec-1-yl-acetamidyl)-25,26,27-tripropoxy-28-phthalimidopropoxycalix[4]arene (**Tb-12a**): ESI-HRMS: calc.:  $m/z$  = 989.9197 ( $\text{M}+2\text{H}$ ) $^{3+}$ , found: 989.8913.

$\text{Tb}^{\text{III}}$ -complex of 5,11,17,23-tetrakis(tris-4,7,10-carboxymethyl-1,4,7,10-tetraazacyclododec-1-yl-acetamidyl)-25,26,27,28-tetrapropoxycalix[4]arene (**Tb-12b**): ESI-HRMS: calc.:  $m/z$  = 941.2423 ( $\text{M}+3\text{H}$ ) $^{3+}$ , found: 941.3101.

## References

1. Gutsche, C. D.; Muthukrishnan, R. *J. Org. Chem.* **1978**, 43, (25), 4905-4906.
2. Konczyk, J.; Nowik-Zajac, A.; Kozlowski, C. A. *Sep. Sci. Technol.* **2016**, 51, (14), 2394-2410.
3. Schühle, D. T.; Peters, J. A.; Schatz, J. *Coord. Chem. Rev.* **2011**, 255, (23-24), 2727-2745.
4. Sreenivasu Mummidivarapu, V. V.; Hinge, V. K.; Rao, C. P. *Dalton Trans.* **2015**, 44, (3), 1130-1141.
5. Lawal, O.; Iqbal, K. S. J.; Mohamadi, A.; Razavi, P.; Dodd, H. T.; Allen, M. C.; Siddiqui, S.; Fucassi, F.; Cragg, P. J. *Supramol. Chem.* **2009**, 21, (1-2), 55-60.
6. Blanchard, S.; Le Clainche, L.; Rager, M.-N.; Chansou, B.; Tuchagues, J.-P.; Duprat, A. F.; Le Mest, Y.; Reinaud, O. *Angew. Chem. Int. Ed.* **1998**, 37, (19), 2732-2735.
7. Baldini, L.; Cacciapaglia, R.; Casnati, A.; Mandolini, L.; Salvio, R.; Sansone, F.; Ungaro, R. *J. Org. Chem.* **2012**, 77, (7), 3381-9.
8. Modi, K.; Panchal, U.; Mehta, V.; Panchal, M.; Kongor, A.; Jain, V. K. *J. Luminesc.* **2016**, 179, 378-383.
9. Schühle, D. T.; Schatz, J.; Laurent, S.; Vander Elst, L.; Muller, R. N.; Stuart, M. C. A.; Peters, J. A. *Chem. Eur. J.* **2009**, 15, (13), 3290-3296.
10. Schühle, D. T.; Polasek, M.; Lukes, I.; Chauvin, T.; Toth, E.; Schatz, J.; Hanefeld, U.; Stuart, M. C. A.; Peters, J. A. *Dalton Trans.* **2010**, 39, (1), 185-191.
11. Bünzli, J.-C. G. *Coord. Chem. Rev.* **2015**, 293-294, (Supplement C), 19-47.
12. Escabi-Perez, J. R.; Nome, F.; Fendler, J. H. *J. Am. Chem. Soc.* **1977**, 99, (24), 7749-7754.
13. Darwent, J. R.; Dong, W.; Flint, C. D.; Sharpe, N. W. *J. Chem. Soc., Faraday Trans.* **1993**, 89, (6), 873-880.
14. Bunzli, J. C. G.; Froidevaux, P.; Harrowfield, J. M. *Inorg. Chem.* **1993**, 32, (15), 3306-3311.
15. G. Bunzli, J.-C.; Ihringer, F.; Dumy, P.; Sager, C.; D. Rogers, R. *J. Chem. Soc., Dalton Trans.* **1998**, (3), 497-504.
16. Fischer, C.; Sarti, G.; Casnati, A.; Carrettoni, B.; Manet, I.; Schuurman, R.; Guardigli, M.; Sabbatini, N.; Ungaro, R. *Chem. Eur. J.* **2000**, 6, (6), 1026-1034.
17. Sato, N.; Yoshida, I.; Shinkai, S. *Chem. Lett.* **1993**, 22, (7), 1261-1264.
18. Bonnet, C. S.; Pellegatti, L.; Buron, F.; Shade, C. M.; Villette, S.; Kubicek, V.; Guillaumet, G.; Suzenet, F.; Petoud, S.; Toth, E. *Chem. Commun.* **2010**, 46, (1), 124-126.
19. Lator, R.; DiGesso, J. L.; Mueller, A.; Matthews, S. E. *Chem. Commun.* **2007**, (46), 4907-4909.
20. Vázquez López, M.; Eliseeva, S. V.; Blanco, J. M.; Rama, G.; Bermejo, M. R.; Vázquez, M. E.; Bünzli, J.-C. G. *Eur. J. Inorg. Chem.* **2010**, 2010, (28), 4532-4545.
21. Howell, C. R.; Edwards, H. S.; Gajadhar-Plummer, S. A.; Kahwa, A. I.; McPherson, L. G.; Mague, T. J.; White, J. A.; Williams, J. D. *Molecules* **2003**, 8, (7).
22. He, X.; Liang, H.; Huang, L.; Pan, C. *J. Phys. Chem. B* **2004**, 108, (5), 1731-1735.
23. Pérez-Rodríguez, M.; Varela, L. M.; García, M.; Mosquera, V.; Sarmiento, F. *J. Chem. Eng. Data* **1999**, 44, (5), 944-947.

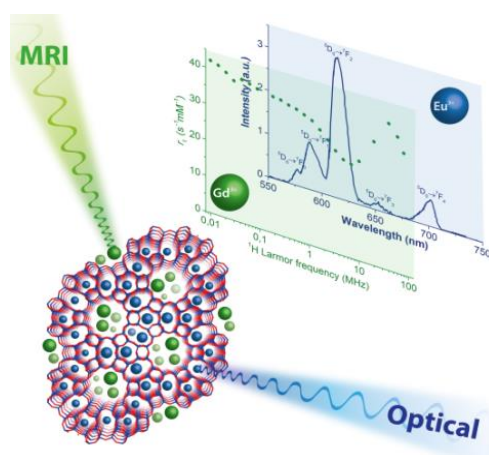


24. Murru, M.; Parker, D.; Williams, G.; Beeby, A. *Journal of the Chemical Society, Chem. Commun.* **1993**, (14), 1116-1118.
25. Chen, G.; Wardle, N. J.; Sarris, J.; Chatterton, N. P.; Bligh, S. W. A. *Dalton Trans.* **2013**, 42, (39), 14115-14124.
26. Gutsche, C. D.; Lin, L.-G. *Tetrahedron* **1986**, 42, (6), 1633-1640.
27. Kelderman, E.; Verboom, W.; Engbersen, J. F. J.; Reinhoudt, D. N.; Heesink, G. J. T.; van Hulst, N. F.; Derhaeg, L.; Persoons, A. *Angew. Chem. Int. Ed. Engl.* **1992**, 31, (8), 1075-1077.
28. Klimentová, J.; Vojtišek, P. *Journal of Molecular Structure* **2007**, 826, (1), 48-63.

---

# Nanozeolite-LTL with Gd<sup>III</sup> Deposited in the Large and Eu<sup>III</sup> in the Small Cavities as a Magnetic Resonance Optical Imaging Probe

# 4



---

The contents of this chapter have been published in:

F. Mayer, W. Zhang, T. Brichart, O. Tillement, C. S. Bonnet, É. Tóth, Joop A. Peters, K. Djanashvili  
*Chem.-Eur. J.*, **2014**, *20*, 3358-3364

## Introduction

In the beginning of 2013 around 200 different zeolite structures were known, of which more than 40 are naturally occurring and the others are synthetic frameworks.<sup>1</sup> This immense diversity is the basis for a broad array of applications, that ranges from catalysis and molecular filtration to medical, agricultural and biological uses and consequently, researchers from all those fields are working on the development of new materials and their application.<sup>2,3</sup> One of the most known and widely applied zeolites is the Linde Type A zeolite (LTA). Its framework is built up from sodalite cages, which are connected in a cubic structure via the tetragonal faces. An important application of this zeolite is as an additive in washing powders, where it acts as a water softener.<sup>4</sup> This application is based on one of the most striking properties of zeolites, namely the extensive ion exchange behavior. The aluminosilicate frameworks of almost all zeolites are anionic, due to tetrahedrally coordinated Al which is replacing Si in the zeolite structure. The negative charges are usually compensated by incorporated cations (mainly Na<sup>+</sup>, K<sup>+</sup>, Mg<sup>2+</sup>, Ca<sup>2+</sup>) but because of the porous nature of the zeolites a part of those ions is accessible for the surrounding solution and can be exchanged by almost any other cation that fits into the cavities. And indeed, after exchanging zeolites with rare earth ions, the obtained materials have been successfully exploited as cracking catalysts in petrochemical processes.<sup>5</sup> The fact that rare earth elements, mainly the lanthanides, are also widely applied in medical applications, such as magnetic resonance imaging (MRI), drew the attention of researchers from the field of MR imaging towards zeolites.<sup>6-8</sup>

Nowadays, the aim is to develop highly efficient magnetic probes that would enable MRI to perform molecular imaging. In this context, it is required that the sensitivity of the imaging modality is increased so far, that preferably single reporter units, or at least concentrations as low as possible can be visualized. For this purpose the spatial resolution of MRI seems to be just right, however it lacks the high sensitivity of other imaging techniques, such as optical or nuclear imaging.<sup>9</sup> Lanthanide loaded zeolites can help to overcome this sensitivity issue by delivering a high payload of active material in one probe.<sup>10</sup> Another advantage of the zeolites is that the compartmentalization of the volume inside can be used to trap ions in different framework environments.<sup>11</sup> This accurate control over the ion locations leads to increased performances of the single components in the zeolite and offers the possibility to

combine different imaging modalities in a single probe. In the meantime, several zeolite frameworks were loaded with lanthanide ions in order to use the obtained materials in medical imaging. It was found that the framework structure is of very high importance for the performance in MRI.<sup>12-14</sup> The mobility of water in the different pore systems is crucial for high relaxivities  $r_1$  (the relaxation rate enhancement in  $s^{-1}$  per mmol of paramagnetic ion). For this reason, larger pore size seems to be favorable for MRI probes. On the other hand, the luminescence of lanthanides is efficiently quenched by water, so that ions for this application need to be shielded from water in the first coordination sphere as efficiently as possible.<sup>15</sup>

Amongst others the zeolites Y and LTL were already applied in the design of bimodal imaging probes due to the fact that they comprise relatively large pores. Zeolite Y is composed of sodalite units (like zeolite A) which are connected via the six-membered facettes to form a superstructure with a large void space in the center.<sup>1,6</sup> The free diameter of this space is 11.8 Å and the opening towards the hexagonally arranged neighboring pores has a diameter of 7.4 Å. This three-dimensional porous structure allows for relatively fast water diffusion within the framework and therefore much higher performance in MRI than the zeolites with smaller pores. This is why Gd loaded NaY was already studied and described intensively over the last 3 decades.<sup>6,7,14,16,17</sup> It was found, that despite the large pore diameter exchange of the bulk water with the water in the zeolite pores is the limiting factor for the relaxivity.<sup>6</sup> This is reflected in the temperature dependence of the relaxivity, which is increasing upon heating due to a faster diffusion. Moreover, an inverse dependence of the relaxivity on the loading was found. At high loadings the efficiency of every single Gd-ion drops considerably from 37.8  $s^{-1}mM^{-1}$  to 9.6  $s^{-1}mM^{-1}$  upon increase of the loading from 1.3 to 5.4 wt.-% (@ 25 °C and 60 MHz). However, the ion exchanged zeolites were very stable and no obvious leaching of the incorporated Gd<sup>3+</sup> could be found in the pH range from neutral down to pH 2.5 and in the presence of up to 25 mM alkali metal ions.<sup>6,7</sup>

While in the case of zeolite Y an ion exchange procedure was applied, in zeolite LTL, which is another candidate in the design of bimodal optical/MR imaging probes, paramagnetic Gd-DOTA complexes were grafted to the surface of the zeolite particles. This procedure resulted in a loading of 0.84 wt.-% Gd<sup>3+</sup> and high relaxivities of around 36  $s^{-1}mM^{-1}$  (@ 20 MHz and 37 °C). The fluorescence signal of the designed dual probe resulted from the incorporated organic dye pyronine in the linear cavities of the zeolite LTL framework.<sup>8</sup>

The major drawbacks of this approach were found in the low loading of  $\text{Gd}^{3+}$  compared to the ion exchange procedure and the low flexibility of the method. The use of other dyes or even other imaging modalities requires a thorough optimization of the loading procedure. However, the framework of zeolite LTL comprises large pores as well as small cavities and therefore, we envision zeolite LTL to be an interesting candidate for the design of bimodal imaging probes via ion exchange.<sup>11</sup> In detail, the framework of this type of zeolite is built up from so-called cancrinite cages (Figure 4.1a), which are connected via their upper and lower 6-membered rings to form columns (Figure 4.1b, I), interlinked to neighboring columns via oxygen bridges (II). The larger channels (III) formed by those columns are separated from each other by elliptical 8-membered ring channels (IV), parallel to the original columns along the c-axis of the crystal. The diameter of the narrowest point of the 12-membered ring ‘superchannels’ (III) is 7.1 Å, whereas at the widest point the channel has a free diameter of 12.6 Å (Figure 4.1c). Ion-exchange in zeolite LTL only takes place in these large channels, as the other spaces are not accessible from the bulk solution.<sup>17</sup> Nevertheless, loading sites other than the big cavities can be accessed by thermal treatment of the Ln-exchanged zeolites. The relocation of the large  $\text{Ln}^{3+}$  into the smaller cavities requires high temperatures, but has to be done carefully in order not to destroy the zeolite framework.<sup>11</sup> Ln-ions once

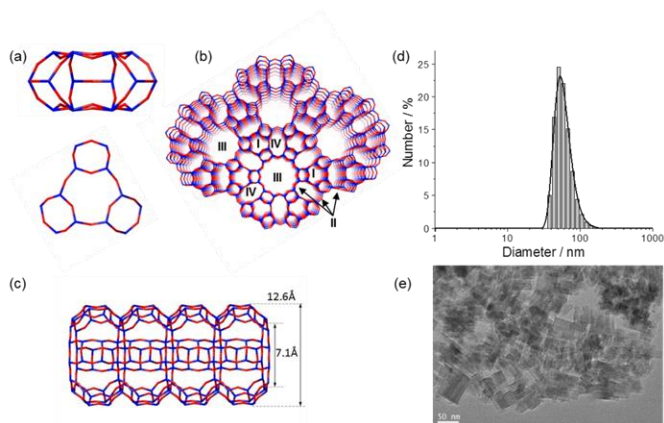


**Figure 4.1.** Framework and particle size of zeolite LTL: (a) cancrinite cages (top = view along (100), bottom = view along (001)); (b) detail of the zeolite framework viewed along (001); (c) a side view along (100) of the largest channel and its dimensions; (d) Hydrodynamic radius determined by DLS; (e) TEM image of zeolite LTL crystals.

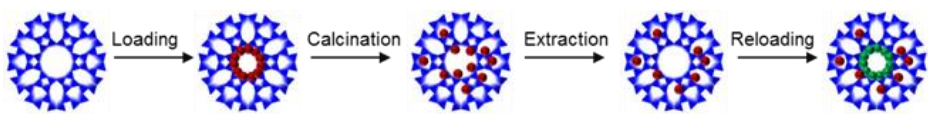
moved into small cages, are locked there and cannot be exchanged or extracted anymore. In contrast, ions in the largest channels are prone to exchange and can be extracted by saturated NH<sub>4</sub>Cl solutions for more than 90% within 24 h. This peculiar arrangement allows for selective deposition of luminescent lanthanides in environments with little water and Gd-ions in the large channels with fast water exchange.

## Results and Discussion

### Loading of zeolite-LTL with lanthanide ions

In this study, Eu<sup>3+</sup> was chosen as an optical reporter because of its sharp emission bands in the visible region (570-720 nm).<sup>15</sup> The removal of the highly quenching water molecules coordinated to the Eu<sup>3+</sup> center is responsible for a dramatic increase of the luminescence intensities and lifetimes upon locking this lanthanide into the small cavities.

**Table 4.1.** Preparation and studies on the properties of double loaded zeolite LTL.<sup>a)</sup>



	Ln-LTL-L	Ln-LTL-C <sup>b)</sup>	Ln-LTL-E	Ln-LTL-R	Gd-Al-TUD1 <sup>c)</sup>	Gd-NaY <sup>d)</sup>
loading (wt%) <sup>e)</sup>	5.2 (5.2/0)	5.0 (1.7/3.3)	3.3 (0.0/3.3)	7.9 (4.6/3.3)	3.8	5.0
Si/Al ratio	3	3	3	3	3.5	1.6
$q^{f)}$	<u>6.1</u>	6.1/0.9	<u>0.9</u>	6.1/0.9	3.6	<u>7</u>
$w$	<u>15</u>	-	<u>32</u>	-	94	37
$r_1$ (mM <sup>-1</sup> s <sup>-1</sup> ) <sup>g)</sup>	37.8	17.8	8.9	43.8 <sup>h)</sup>	30.0	12.0
$r_1'$ (g <sup>-1</sup> Ls <sup>-1</sup> ) <sup>g)</sup>	12.5	5.7	1.9	13.7 <sup>h)</sup>	7.3	3.8
$\tau_m$ (ns)	0.19	-	1660	-	0.27	625
$\tau_{zeo}$ (μs)	<u>0.01</u>	-	<u>0.01</u>	-	<10	33
$\tau_v$ (ps)	26.0	-	9.2	-	48	22
$\Delta^2$ (10 <sup>19</sup> s <sup>2</sup> )	3.8	-	2.9	-	1.2	5.1
$\ln I/T_{2e}$ (s <sup>-1</sup> ) <sup>i)</sup>	22.1	22.2	-	-	22.3	22.64
$\ln I/T_{2e}$ (s <sup>-1</sup> ) <sup>j)</sup>	22.4	21.6	-	-	22.1	22.63
$I_{@615nm}$ (p.d.u.)	120	538	718	415	-	-

<sup>a)</sup>Zeolite framework in polyhedral view, indicating the TO4 tetrahedra (T = Si, Al; Na is not depicted), all parameters are determined at 25 °C; <sup>b)</sup>6h at 600 °C; <sup>c)</sup>Ref 16; <sup>d)</sup>Ref 7; <sup>e)</sup>determined by BMS for Gd-LTL and by EDX for Gd/Eu-LTL (ratio large/small cavity in brackets); <sup>f)</sup>determined by luminescence decay of Eu-LTL; <sup>g)</sup>60 MHz, 25 °C; <sup>h)</sup>Eu in the small, Gd in the big cavities; <sup>i)</sup>As determined from EPR line widths at 0.34 T; <sup>j)</sup>Calculated with best fit parameters.

**Table 4.2.** Results of the leaching study in water and phosphate solution.

	water				NaH <sub>2</sub> PO <sub>4</sub>
	pH 4	pH 5	pH 6	pH 8	45 mg/L, pH 7
initial Gd <sup>3+</sup> [ $\mu$ M]	685.8	597.3	508.8	465.5	591.0
free Gd <sup>3+</sup> [ $\mu$ M]	5.7	2.1 <sup>a</sup>	2.9 <sup>a</sup>	3.3 <sup>a</sup>	0.4 <sup>a</sup>
leaching [%]	0.84	0.36	0.57	0.73	0.08

<sup>a</sup> below detection limit of the colorimetric assay.

On the other hand, Gd<sup>3+</sup> was envisaged as an MRI reporter since high  $r_1$  relaxivities can be achieved with it.<sup>9</sup> As  $r_1$  is directly proportional to the number of water molecules coordinated to the Gd-center ( $q$ ), loading of Gd<sup>3+</sup> into the big pores of the LTL-zeolite pre-loaded with Eu<sup>3+</sup> into the small cages offers an elegant approach for the exploitation of the unique physical properties of each of these lanthanides for the design of a bimodal optical/MRI probe.

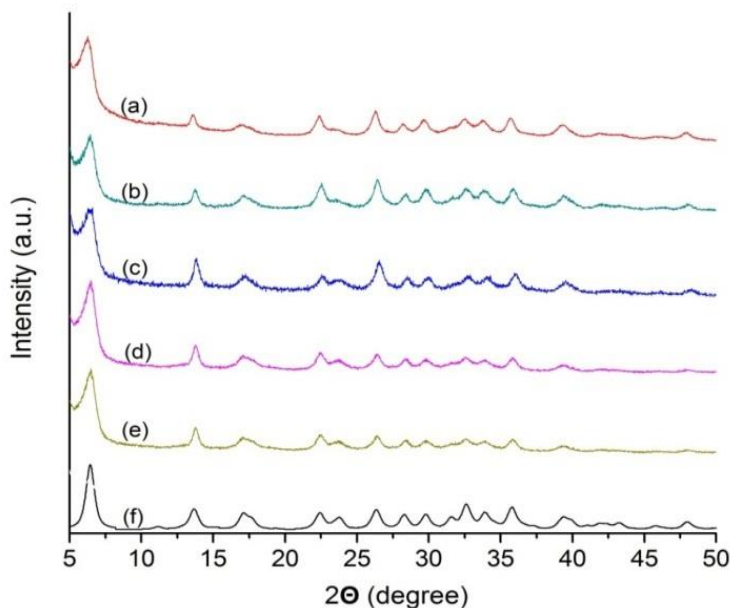


**Figure 4.2.** XRD patterns of the zeolite framework after different steps of the loading procedure. The zeolite as obtained (a) was calcined at 600 °C in absence (b) and presence (c) of Ln<sup>3+</sup> ions without any significant change in the XRD pattern. The initial loading (d) and the extraction step (e) did also not alter the framework. The last diffractogram represents the powder pattern as it was calculated from the database of zeolite structures for the Linde Type L framework with a wavelength of 1.78897 Å (Co K $\alpha$ ) and U = 0.5 for the peak width adjustment.<sup>1</sup>

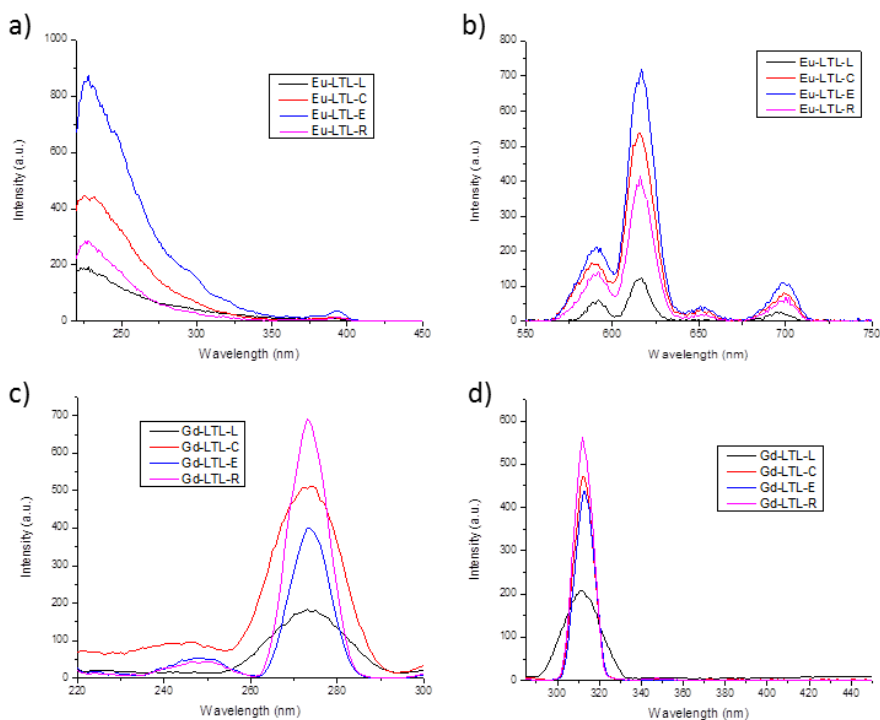


**Figure 4.3.** Excitation (a/c) and emission (b/d) spectra of Eu-loaded samples and Gd-loaded samples were obtained in time-resolved mode with a delay of 0.1 ms and an averaging time of 0.1 s. Due to the large difference in luminescence intensity of Gd-LTL-L and Gd-LTL-C in the excitation (c) and Gd-LTL-L in the emission spectrum (d), slits had to be adjusted (inducing the difference in peak width). The result of this change of slits for Gd-loaded samples is that intensities are difficult to compare precisely. For the Eu-loaded sample, slits of all 4 samples were kept the same, resulting in the following relation in fluorescence intensities: Eu-LTL-L < Eu-LTL-C < Eu-LTL-R < Eu-LTL-E.

For the initial ion exchange stirring the Na-LTL in an aqueous  $\text{LnCl}_3$  solution for 24 h turned out to be sufficient for a loading of 5.2 wt-% of Ln into the zeolite (Table 4.1, Ln-LTL-L). Since only 3.6 alkali ions per unit cell are located in the large channels,<sup>11</sup> the theoretical maximum exchange capacity for  $\text{Ln}^{3+}$  ions is 6.4 wt-%. In this context, the achieved 5.2% loading (corresponding to 0.97 Ln ions per unit cell) is very close to complete substitution of the exchangeable alkali ions. The loading did not change substantially upon calcination of the material (Ln-LTL-C), which is not surprising as no  $\text{Ln}^{3+}$  is extracted during this step and only intra-zeolitic ion-migration takes place. To prove this relocation, three different samples were subjected to extensive ion extraction insaturated  $\text{NH}_4\text{Cl}$  solution. The first sample was Gd-loaded (Gd-LTL-L), and the next two were calcined during 6 h at 400



or 600 °C (Gd-LTL-C). Before extraction, all three samples had the same Gd<sup>3+</sup> content of ~5 wt-%, but after extracting for 72 h the determined Gd<sup>3+</sup> loading was 0.48%, 2.29% and 3.30% (Gd-LTL-E), for the three samples respectively, showing that only after calcination a considerable amount of Gd<sup>3+</sup> is retained during the extraction step. The influence of the temperature on the migration of the ions is illustrated by the fact that after an increase from 400 to 600 °C, the amount of the migrated ions increased from 2.3 to 3.3 wt-%. A subsequent reloading (analogue to the first loading step) resulted in samples with Gd-loading increased by 4.6% (Gd-LTL-R), which is almost as high as during the first step, indicating that in all cases the cavities are available for reloading. After each step, X-ray diffraction patterns were recorded to demonstrate that the structure of the zeolite is not affected by the treatment (Figure 4.2). The amount of Gd<sup>3+</sup> present in the zeolite framework after each step was determined by bulk magnetic susceptibility (BMS)<sup>18</sup> measurements on aqueous suspensions stabilized with 1 wt-% of xanthan gum. Via the mass of the dispersed zeolite the loading was calculated (Table 4.1). To prove the principle, the same loading procedure was applied to introduce Eu<sup>3+</sup> into LTL, followed by a calcination-extraction sequence to lock the ions in the different framework environments.

The harsh conditions needed for the extraction indicate the strength of the ion absorption in zeolite. Under all conditions needed for the here described investigations, no leaching of Gd<sup>3+</sup> ions could be detected. A leaching study was performed in the pH range from 4 to 8 and in the presence of phosphate ions. Only at pH 4, the detection limit (4 μM) of the colorimetric assay was reached after a 24 h incubation time (Table 4.2). Clearly, the feasibility of these materials for medical or biological applications will require a more detailed leaching study under physiological conditions, as well as the decoration of the surface with organic moieties along with a thorough toxicological assessment.

#### ***Luminescence of the loaded zeolite-LTL***

Dispersions of Ln-LTL-L, Ln-LTL-C and Ln-LTL-E (Ln = Eu and Gd) in water were investigated in respect to their photophysical properties. The luminescence intensities for both, Gd<sup>3+</sup> and Eu<sup>3+</sup>-loaded samples, increased upon calcination and even further after the extraction step (Figure 4.3). This effect is accompanied by an increase in the luminescence

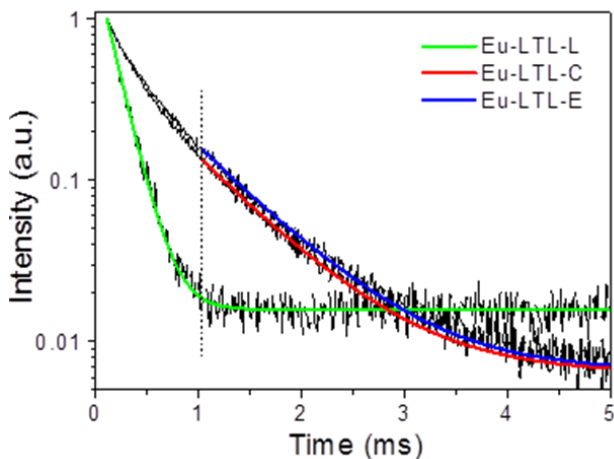


**Figure 4.4.** Normalized luminescence decay profiles of Eu-LTL-L, Eu-LTL-C, and Eu-LTL-E dispersions, the smooth lines represent the fits that were used to calculate  $q$ -values, using the data above 1 ms for Eu-LTL-C and Eu-LTL-E.

decay lifetime (Figure 4.4). Both phenomena can be explained by the decrease of the amount of water molecules in the first coordination sphere of the lanthanide ions leading to a reduction of possible non-radiative decay pathways.<sup>19</sup> To get an insight into the different coordination behavior the luminescence lifetimes were used to determine the number of water molecules in the first coordination sphere of  $Eu^{3+}$  ions in either location. From the fitting of the decay curves (Figure 4.4), the average  $q$ -values were evaluated to be 6.2, 0.9 and 0.8 for Eu-LTL-L, Eu-LTL-C and Eu-LTL-E, respectively. To exclude contributions from the fast-decaying ions in the large channels, the obtained curves for LTL-C and LTL-E samples were only fitted for lifetimes  $> 1$  ms. Thus, the  $q$ -values reported for those samples only represent the  $Eu^{3+}$ -ions in the small cages. To reproduce the complete decay curves, a bi-exponential fit with one decay constant fixed to the value obtained for Eu-LTL-L (0.158 ms) resulted in functions that fit the whole curve with adjusted  $R^2$  values  $> 0.99$  and a second decay constant that was identical with the one, that was obtained from the mono-exponential fit  $> 1$  ms. Going from Eu-LTL-C to Eu-LTL-E, the ratios of the pre-exponential factor changed in favor of the longer decaying function, showing that the number of Eu-ions in the big cage was reduced during the washing procedure.

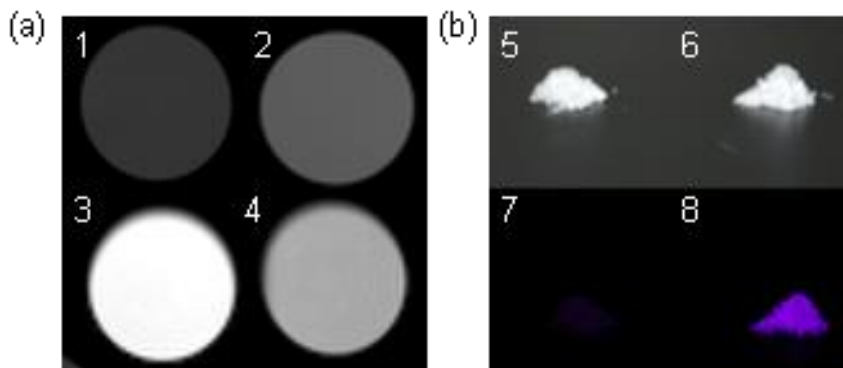


**Figure 4.5.** (a)  $T_1$ -weighted images (7T, 25 °C) of phantoms formed by four pallets containing 1% xanthan (1), water (2), Gd-LTL-L (3) and Gd-LTL-E (4) suspended in 1% xanthan at Gd concentration of 0.5 mM; (b) Optical images of solid powders of Eu-LTL-L (5, 7) and Eu-LTL-E (6, 8) under daylight (upper panel) and UV-light of 258 nm (lower panel).

As mentioned above, to optimally exploit the imaging performance of  $Gd^{3+}$  and  $Eu^{3+}$  in the LTL zeolite, the latter should be localized in the small cages to reduce the quenching by water, whereas  $Gd^{3+}$  profits from the high  $q$ -values in the large channels. These effects are illustrated in Figure 4.5. However, coordinated water is not the only parameter governing  $r_1$ . Other parameters governing the relaxivity were evaluated using proton nuclear magnetic relaxation dispersion ( $^1H$  NMRD) of aqueous dispersions of Gd-LTL-L and Gd-LTL-E (see Table 4.3) stabilized with 1% xanthan gum. The  $^1H$  NMRD profiles were recorded at different temperatures (Figure 4.6) from 25 to 50 °C, however for the fittings only the results at 25 °C were used because at higher temperatures a slight decrease of  $r_1$  was observed over time. A more detailed study on the temperature behavior of the samples was

**Table 4.3.** Composition of the different  $Gd^{3+}$ -loaded samples for NMRD measurements.

	Gd-LTL-L	Gd-LTL-C	Gd-LTL-E	Gd/Eu-LTL-Rb
total loading (wt-%) <sup>a</sup>	5.2	5.0	3.3	7.9
big cage (wt-%) <sup>a</sup>	5.2	1.7	0.0	4.6
small cage (wt-%) <sup>a</sup>	0.0	3.3	3.3	3.3
ratio big/small	-	0.52	-	1.39b
czeo (mg/mL)	1.12	2.63	14.44	0.96
cGd <sup>3+</sup> (mM)	0.37	0.84	3.03	0.28

<sup>a</sup> %-w/w of the  $Ln^{3+}$  in respect to the zeolite. <sup>b</sup>Eu<sup>3+</sup> in the small cage, Gd<sup>3+</sup> in the big cage.

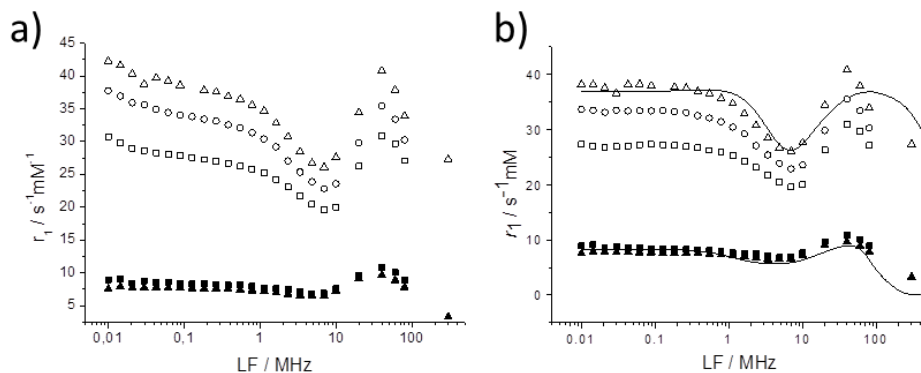


**Figure 4.6.**  $^1H$  NMRD profiles of the Gd-LTL-L (open symbols) and Gd-LTL-E (filled symbols) at 25 °C (triangles), 37 °C (circles), and 50 °C (squares) before (a) and after (b) correction for the silica contribution. The curves were calculated with best-fit values, tabulated in Tables 4.1.

carried out to reveal the origin of this effect. Therefore, a Gd-LTL-L dispersion of known Gd-concentration (stabilized with 1 wt-% xanthan) was divided in three equal parts, each part was incubated at a defined temperature and the relaxivity was determined over time (Figure 4.7). While the  $r_1$  measured at 7 T and 25 °C remained constant, the initial value of 21.8  $mM^{-1}s^{-1}$  drops to 17.6 and 12.9  $mM^{-1}s^{-1}$  at 37 and 50 °C, respectively. This change looks dramatic, but after cooling back to 25 °C, the relaxivities were restored to 21.3 and 19.9  $s^{-1}mM^{-1}$  for the 37 and 50 °C samples, respectively. This behavior indicates that there are two effects overlapping. A remarkable temperature dependence of the relaxivity with a strong decrease upon heating can be found in the first 10 min. This is the time that the sample needs to equilibrate before it reaches the desired temperature. However, this effect is 100% reversible and only assigned to the temperature dependence of the parameters governing relaxivity. The second effect is irreversible and can be displayed by fitting the linear part of the profiles (indicated by the lines in Figure 4.7). To determine the origin of this effect, the loaded zeolite was incubated in pure water at various temperatures without xanthan being present. After cooling back to 25 °C it was mixed with xanthan for better stability and subsequently the relaxivity was determined. With these experiments it was found, that in the absence of xanthan during the heating phase, the irreversible component of the relaxivity change did not appear. As this effect was not observed for other particles before, we assume that the xanthan at higher temperatures starts to enter the linear pores of the zeolite LTL framework and thus limits the water exchange. This increase in the residence time of water

within the zeolite ( $\tau_{zeo}$ ) can be held responsible for the reduction of the relaxivity according to equation 1. To make sure that this effect does not influence the results of the fittings, the data obtained at temperatures  $> 25$  °C is only used for qualitative considerations.

$$r_1 = \frac{w+q}{55500} \left( \frac{1}{T_{1,zeo} + \tau_{zeo}} \right) \quad (1)$$

When investigating the  $^1\text{H}$  NMRD profiles in detail, it can be seen that the relaxivity is not independent of the Larmor frequency (LF) at low magnetic fields. The trend of  $r_1$  to decline up to 1 MHz rather than being constant, as usually observed, can be explained by a contribution of the zeolite to the relaxivity due to the long correlation time modulation of the dipole–dipole relaxation of the protons of relatively immobile water molecules adsorbed on the surface of the zeolite particles.<sup>20</sup> Similar phenomena have previously been observed in the NMRD profiles of Gd-chelates grafted to hydroxyapatite and  $\text{TiO}_2$  particles.<sup>21-23</sup>

By contrast, the low field parts of the NMRD profiles for the Gd-LTL-E are perfectly horizontal (Figure 4.6a). Most likely, the strong adsorption of water to the surface of loaded zeolite particles involves silanol groups, which are removed during calcination. Thus, for the

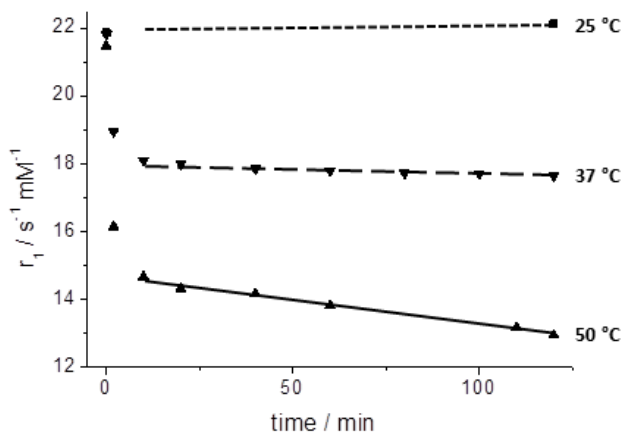


**Figure 4.7.** The time profile of the longitudinal relaxivity  $r_1$  (300 MHz) at different temperatures. The slopes of the lines are representing the decay of the relaxivity over time. Slopes of those lines are  $2.1 \cdot 10^{-3} \text{ s}^{-1} \text{mM}^{-1} / \text{min}$ ,  $-3.1 \cdot 10^{-3} \text{ s}^{-1} \text{mM}^{-1} / \text{min}$  and  $-13.9 \cdot 10^{-3} \text{ s}^{-1} \text{mM}^{-1} / \text{min}$  for 25, 37 and 50 °C, respectively.

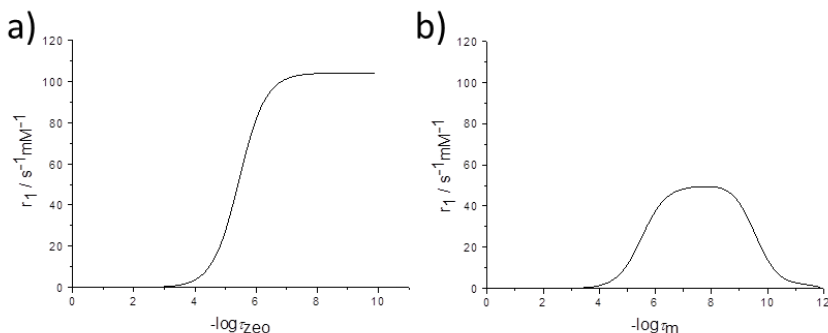


**Figure 4.8.** Simulation of  $r_1$  as a function of a)  $\tau_{zeo}$  (fixed  $\tau_m = 6.5 \times 10^{-10}$  s) and b)  $\tau_m$  (fixed  $\tau_{zeo} = 6.6 \times 10^{-8}$  s) using Eq. 1-5, assuming  $\tau_R > 10^{-8}$  s,  $\tau_{zeo} = 1.4 \times 10^{-11}$  s,  $A_2 = 2.1 \times 10^{19}$  s $^{-2}$ ,  $w = 15$ , and  $q = 6$ .

fitting of the obtained  $^1H$  NMRD data, a fraction of the silica profile reported by Gillis et al.<sup>20</sup> was subtracted and the magnitude of that fraction was iterated until the low-field part of the resulting profile was horizontal up to a LF of  $\sim 1$  MHz. The resulting profiles are represented in Figure 4.6b. The local maxima at about 60 MHz in NMRD profiles of the presently studied systems are typical for systems with relatively long rotational correlation times ( $\tau_R$ ). Equation 1 (see following pages) shows that  $r_1$  is proportional to  $q$ , which explains the substantial decrease in  $r_1$  upon calcination of Gd-LTL-L. During the calcination, a loss of five water molecules in the first coordination sphere of the  $Ln^{3+}$ -ion occurs. In contrast,  $r_2$  is not depending on  $q$  and is similar for Gd-LTL-L and Gd-LTL-E with 93 and 72 s $^{-1}$  mM $^{-1}$  (7T, 25 °C), respectively. This leads to  $r_2/r_1$  ratios of 3.4 for the loaded vs 22.0 for the extracted material. The loaded values is between 1 and 10, as required for optimal performance as positive CA.<sup>17</sup>

$^1H$  NMRD profiles are influenced by a large number of parameters, which makes the quantitative evaluation of these data a difficult task. Therefore, several constraints were introduced. The values of  $q$  were fixed at 6 and 1 for Gd-LTL-L and Gd-LTL-E respectively, the values determined by the luminescence decay of the corresponding Eu-loaded samples. As we have demonstrated that for zeolites,  $r_1$  is independent of  $\tau_R$  implying that  $\tau_R \geq 10^{-8}$  s,  $\tau_R$  was fixed to  $10^{-8}$  s.<sup>7</sup>

Further constraints could be derived from the peculiar temperature dependence of the relaxivities (Figure 4.6), which appear to be opposite for Gd-LTL-L and Gd-LTL-E: for the

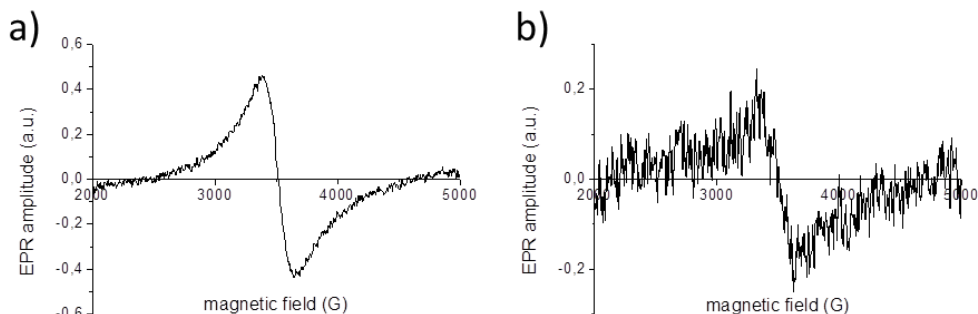


**Figure 4.9.** EPR spectra of Gd-LTL-L and Gd-LTL-E in aqueous solution containing 1 wt-% xanthan gum. Concentrations were 0.94 mM and 0.83 mM for Gd-LTL-L and Gd-LTL-E, respectively. The  $g$ -factors are 1.982 (LTL-L) and 1.988 (LTL-E) and the linewidth ( $\Delta H_{pp}$ ) is 250.3 and 285.4 G.

former,  $r_1$  decreases with temperature, whereas it increases for the latter. The parameters mainly determining the temperature dependence of  $r_1$  are the residence time of the water molecules in the first coordination sphere of  $Gd^{3+}$  ( $\tau_m$ ) and that of the water molecules inside the zeolite ( $\tau_{zeo}$ ). Obviously, both residence times decrease with increasing temperature meaning that the exchange rates speed up. Two characteristic simulations of the dependence of  $r_1$  on  $\tau_{zeo}$  and  $\tau_m$  are displayed in Figure 4.8. An inspection of these curves shows that the temperature dependencies can only be explained if  $\tau_m < 10^{-9}$  s for Gd-LTL-L and  $> 10^{-7}$  s Gd-

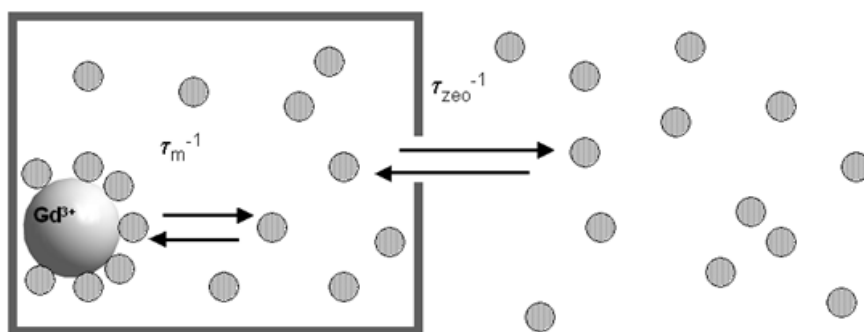


**Figure 4.10.** Schematic representation of the two-step mechanism to account for the relaxivity in an aqueous suspension of  $Gd^{3+}$ -loaded zeolite nanoparticles.

LTL-E. Furthermore, the decrease of  $r_1$  with temperature for Gd-LTL-L requires that the temperature effect due to  $\tau_{zeo}$  is small, thus either  $\tau_{zeo} > 10^{-4}$  or  $< 10^{-8}$  s. The former possibility can be excluded, since that cannot explain the high relaxivities observed for Gd-LTL-L. Based on these considerations  $\tau_{zeo}$  was fixed at  $10^{-8}$  s and  $\tau_m$  was constrained to  $< 10^{-9}$  s for Gd-LTL-L and to  $> 10^{-7}$  s Gd-LTL-E. Finally, further constraints were imposed by performing the fittings of the NMRD profiles simultaneously with EPR line widths (Figure 4.9) using a set of equations derived previously.

In zeolitic systems studied until now, the diffusion of water from the interior of the zeolite to the bulk limits the relaxivity. In this case, the analysis of NMRD profiles requires additional parameters to take this effect into account. Therefore, we have previously developed a two-step model (Figure 4.10).<sup>7</sup> First, the relaxivity of the water inside the zeolite nanoparticles ( $T_{1zeo}$ ) is derived by considering the exchange between water molecules in the first coordination sphere of Gd<sup>3+</sup> and free water molecules inside the zeolite (eq. 2). Here,  $w$  is the number of free water molecules (not bound to Gd<sup>3+</sup>) inside the zeolite per Gd<sup>3+</sup> ion and  $T_{1m}$  is the longitudinal relaxation time of inner sphere water protons, which is given by the Solomon-Bloembergen-Morgan equation (eq. 3).<sup>24,25</sup>

$$\frac{1}{T_{1zeo}} = \frac{\frac{q}{w}}{\tau_m + T_{1m}\left(1 + \frac{q}{w}\right)} \quad (2)$$

$$\frac{1}{T_{1m}} = \frac{2}{15} \left(\frac{\mu_0}{4\pi}\right)^2 \frac{\hbar^2 \gamma_S^2 \gamma_I^2}{r_{GdH}^6} S(S+1) \left( \frac{3\tau_{d1}}{1 + \omega_I^2 \tau_{d1}^2} + \frac{7\tau_{d2}}{1 + \omega_S^2 \tau_{d2}^2} \right) \quad (3)$$

Here,  $r_{GdH}$  is the effective distance between the Gd<sup>3+</sup> electron spin and the water protons,  $\gamma_S$  and  $\gamma_I$  are the electron and proton gyromagnetic ratios, respectively, and  $\tau_{di}^{-1} = \tau_m^{-1} + \tau_R^{-1} + T_{ie}^{-1}$  ( $i = 1, 2$ ). The electronic relaxation rates ( $T_{ie}$ ) are approximated by equations (4) and (5), where  $\omega_S$  is the Larmor frequency,  $\Delta^2$  is the trace of the square of the zero-field splitting (ZFS) tensor, and  $\tau_v$  is the correlation time for the modulation of ZFS.

$$\frac{1}{T_{1e}} = 1/25 \Delta^2 \tau_v [4S(S+1) - 3] \left( \frac{1}{1 + \omega_S^2 \tau_v^2} + \frac{4}{1 + 4\omega_S^2 \tau_v^2} \right) \quad (4)$$

$$\frac{1}{T_{2e}} = \Delta^2 \tau_v \left( \frac{5.26}{1 + 0.372 \omega_S^2 \tau_v^2} + \frac{7.18}{1 + 1.24 \omega_S^2 \tau_v^2} \right) \quad (5)$$



In the second step, the exchange of water between the inside of the zeolite and the bulk by the diffusion through the zeolite channels is considered. This enables the propagation of the relaxation enhancement from the interior of the material to the bulk water outside. If the chemical exchange between protons in two magnetically distinct environments (inside and outside the zeolite) is taking place under highly dilute conditions of the paramagnetic entities, equation (1) can be derived for the overall longitudinal relaxivity.

Here,  $\tau_{\text{zeo}}$  is the residence lifetime of water protons inside the zeolite. The contribution of water molecules diffusing along the paramagnetic center without being bound to it (the outer sphere contribution) can be neglected for both the exterior and the interior of the investigated materials because the contribution of this mechanism to the overall relaxivity has been shown to be small for zeolite-immobilized  $\text{Gd}^{3+}$ , particularly at Larmor frequencies higher than 0.1 MHz. This model has been validated for several zeolitic systems.<sup>6,16</sup> For the fitting procedure of the obtained NMRD data, the following values were used. The distance  $r_{\text{GdH}}$  was fixed at 3.1 Å,  $E_v$  at 1 kJ mol<sup>-1</sup>,  $q$  at the values obtained from the luminescence decay experiments ( $q = 1$  and 6 for the extracted and loaded sample, respectively), and  $w$  at the values calculated from the molecular formula of the zeolite  $\text{K}_6\text{Na}_3(\text{H}_2\text{O})_{21}\text{Al}_9\text{Si}_{27}\text{O}_{72}$  in combination with the loading. In detail, an average of one  $\text{Gd}^{\text{III}}$  ion per unit cell was loaded into the framework. 21 water molecules are present per unit cell of which 15 are free and 6 are coordinated to the Gd-center ( $q = 6$ ). Furthermore, the correlation times  $\tau_m$  and  $\tau_{\text{zeo}}$  were limited by the boundaries discussed above. Attempts to fit the data with correlation times outside these boundaries led to unsatisfactory fits and/or to unrealistic values for the variable parameters, such as negative activation energies. It may be expected that  $\tau_{\text{zeo}}$  is the same for calcined and uncalcined Gd-LTL and it should be smaller than 10<sup>-7</sup> s. Since Figure 8 shows that under these conditions  $\tau_{\text{zeo}}$  has almost no significant influence on  $r_1$ , its value was fixed at 10<sup>-8</sup> s. Finally, we have included in the fittings some values of transverse electronic rates ( $1/T_{2e}$ ) as obtained from EPR peak-to-peak line widths (Figure 4.9) with equation (6), where  $\mu_B$  is the Bohr magneton,  $g_L$  the electron Landé factor,  $h$  the Planck constant, and  $\Delta H_{\text{pp}}$  the peak-to-peak line width.

$$\frac{1}{T_{2e}} = \frac{g_L \mu_B \pi \sqrt{3}}{h} \Delta H_{\text{pp}} \quad (6)$$

Although the number of variables was still considerable the obtained best fit values turned out to be reasonable. They are compiled in Table 4.1 and NMRD profiles calculated with these values are represented as curves in Figure 4.6b. For comparison some previously determined data on Gd<sup>3+</sup>-loaded zeolite NaY and mesoporous material AITUD-1 are included in Table 4.1. The best-fit values of the parameters governing the transversal electronic relaxation rate ( $1/T_{2e}$ ),  $\tau_v$  and  $\Delta^2$ , are in the range usually observed for Gd<sup>3+</sup> loaded zeolites,<sup>9</sup> resulting in values of  $1/T_{2e}$  that are in good agreement with the values measured by EPR at 0.34 T (Table 4.1).

Interestingly, the values for  $\tau_m$  are very small compared to that of Gd-NaY with a comparable loading.<sup>7</sup> In Gd-NaY systems, the water exchange process in the zeolite supercages speeds up substantially upon increasing the Gd<sup>3+</sup> loading, which is a consequence of the increase of the Gd<sup>3+</sup> concentration inside the zeolite cavities, which makes the probability of a water molecule being located in the inner coordination sphere of the Gd<sup>3+</sup> ion higher. In the presently studied Gd-LTL-L system, the residence time of water inside the zeolite ( $\tau_{zeo}$ ) is so short that in this case the exchange process is probably not limited to the water inside the zeolite nanoparticles. For the Gd-LTL-E sample, however, the value for  $\tau_m$  is rather large, which may be rationalized by the locked location of the

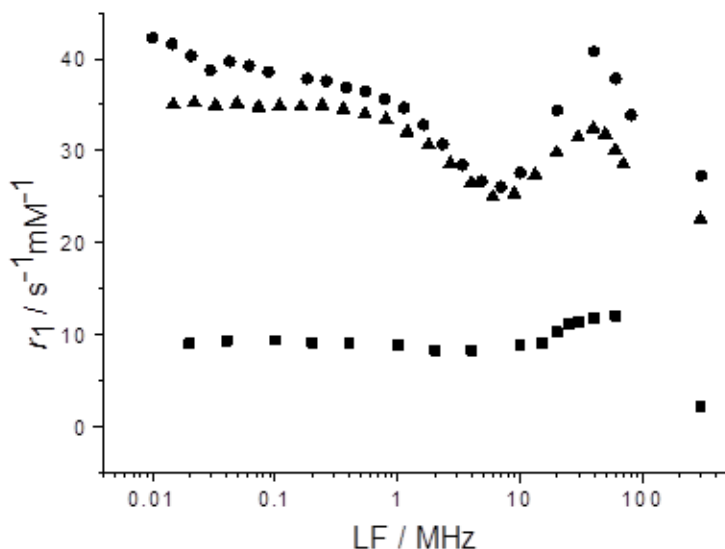


**Figure 4.11.** <sup>1</sup>H NMRD profiles of Gd-LTL-L (circles, 5.18 % loading, 25 °C), Gd-AITUD-1 (triangles, 3.8% loading, 25 °C)<sup>17</sup> and Gd-NaY (squares, 5% loading, 37 °C).<sup>16</sup>

Gd<sup>3+</sup> ions after calcination. Assuming that the exchange follows a dissociative mechanism, the encapsulation may lead to a relatively high steric strain on the remaining bound water molecule and, consequently, lead to a relatively large free enthalpy gap between the ground state and the eight-coordinate transition state and thus to a relatively slow water exchange rate.

The very high water-exchange rate between the interior and exterior of Gd-LTL compared to that of Gd-NaY (2 orders of magnitude higher) is somewhat surprising since both zeolites have 12-membered ring entrance windows with sizes of 7.1 and 7.4 Å, respectively. Most likely the linear channels are the reason for this fast diffusion within the material. This is corroborated by intracrystalline self-diffusivity measurements by Caro et al., who demonstrated the water mobility in zeolites NaX and NaY with 3-dimensional channel structures to be beneath that in zeolite ZSM-5 with a linear channel structure.<sup>26</sup> The exchange rate of Gd-LTL is about as fast as for mesoporous materials,<sup>16, 27</sup> which have channels with diameters of 1-20 nm. Accordingly, both materials have comparable <sup>1</sup>H NMRD profiles with high relaxivities in comparison to the Gd-NaY zeolites (Figure 4.11). However, the here presented Gd-LTL material is favorable for application as MRI contrast agent in contrast to Gd-AITUD-1, which showed significant leaching of Gd<sup>3+</sup>. It should be noted that relaxivities expressed in s<sup>-1</sup> mM<sup>-1</sup> do not give a good impression of the efficacy of these materials as MRI contrast agents, due to the difference in loading. Therefore, it is more useful to compare the relaxivity density in s<sup>-1</sup>Lg<sup>-1</sup>. Loaded Gd-LTL has a relaxivity density of 13.7 s<sup>-1</sup>Lg<sup>-1</sup> at 60 MHz and 25 °C, which is about a factor of two higher than the values for the best zeolitic systems reported up to now (Table 4.1). This unmatched relaxivity density is also significantly higher than the one of a clinically applied Gd-DOTA (6.6 s<sup>-1</sup>Lg<sup>-1</sup> at 20 MHz, 25 °C).

## Conclusions

In conclusion, this work demonstrates interesting photo-physical as well as magnetic properties of nanozeolite-LTL acquired upon its loading with Eu<sup>3+</sup> and Gd<sup>3+</sup> ions in the small and big cavities, respectively. The high MRI performance can be explained by the fastest water exchange that was found in zeolitic systems up to now, while the enhanced

luminescence could be achieved by the efficient isolation of the Eu<sup>3+</sup> ions from the water molecules in the first coordination sphere. Based on these findings, nanozeolite LTL is an interesting candidate for the development of high-performance dual imaging probes, with the potential to be exploited for radioisotopes for imaging and/or therapy. However, before the first *in vivo* studies can be started, more biological tests will be necessary, including a detailed leaching study, as well as cell toxicity and uptake studies. The functionalization of the surface with organic groups will also be investigated to further improve the stability and biocompatibility of this promising system.

## Experimental details

All chemicals in this study were used as obtained. The K-LTL nanocrystals were obtained from NanoScape (Planegg, GE). GdCl<sub>3</sub> and EuCl<sub>3</sub> were obtained as hexahydrates from Strem Chemicals, Newburyport, USA. NaCl, NH<sub>4</sub>Cl were obtained from Sigma Aldrich, St. Louis, MO 63103, U.S.A. In all reactions MilliQ water (>18.2 MΩ) was used.

**Methods.** X-Ray diffraction patterns of the zeolites before and after loading and after each step of the preparation were measured using a Bruker AXS/D8 Advance diffractometer equipped with a Lynxeye detector and Co K<sub>α</sub> radiation ( $\lambda = 1.78897 \text{ \AA}$ , 35 kV, 40 mA). The measurement range was from 5 to 70 °2θ with a step size of 0.02° in continuous mode and an acquisition time of 0.5s per step. The scan was repeated until a good signal to noise ratio was achieved.

Gd concentrations were determined by the BMS method.<sup>18</sup> All measurements were done on a Varian Unity Inova 300 NMR spectrometer with *tert*-butanol as internal standard. The sample was prepared by dispersing a defined amount of the Gd containing zeolite in a 10 v/v-% aqueous *tert*-butanol solution containing 1 wt-% xanthan. The induced shift was measured against an aqueous *tert*-butanol solution in a standard inner tube that was added to the sample tube. The concentration was calculated from the shift following the procedure described in literature.

<sup>1</sup>H NMRD profiles were recorded on a Stelar SMARtracer Fast Field Cycling NMR relaxometer (0.01-10 MHz) and a Bruker WP80 NMR electromagnet adapted to variable field measurements and controlled by a SMARtracer PC-NMR console. The temperature was monitored by a VTC91 temperature control unit and maintained by a gas flow. The

temperature was determined by previous calibration with a Pt resistance temperature probe. The longitudinal relaxation rates ( $1/T_1$ ) were determined in water. The samples were prepared by dispersing defined amounts of zeolite (see Table 4.3) in 1 wt-% xanthan solution.

Luminescence excitation and emission spectra and luminescence lifetimes were determined using a Varian Cary Eclipse spectrophotometer using a pulsed Xenon light source. The samples were prepared from dried zeolite materials by dispersion in distilled water and multiple sonications.

The EPR spectra were recorded on a Bruker ESP300 Spectrometer, operating at 9.43 GHz, 0.34 T, X-band), at 298 K with typical parameters: MW power 4mW, modulation amplitude 1.0 mT and time constant 0.03 s.

EDX spectra were recorded on a JEOL-JMS 6010 Scanning Electron Microscope with an acceleration voltage 20kV. The spot analysis of larger agglomerates of particles (as result of freeze-drying and deposition on the SEM sample holder) was used to determine the Gd and Eu content of the samples. Therefore, the samples were put on conductive tape, that was fixed on an aluminum holder.

DLS was done on a Zetasizer Nano ZS from Malvern Instruments Ltd (Malvern, UK). The machine is equipped with a 4.0 mW, 633 nm He-Ne Laser and the  $173^\circ$  back-scatter mode was used to analyze the obtained particles. The multiple-peak fitting procedure implemented in the Software for Zetasizer (Version 6.12) was used to evaluate the autocorrelation function. Diameters are given as number weighted mean values of the obtained particle size distributions. Dispersions were prepared from commercial dry material by suspending it in MilliQ water using a  $\frac{1}{4}$ " ultrasonic probe for 2 min.

**Zeolite loading.** The obtained K-LTL zeolite was first ion exchanged with NaCl. This was done in order to obtain Na-LTL, which is supposed to be more active in the ion exchange with the Ln ions. For this purpose, 1 g of K-LTL was stirred in 20 mL NaCl solution (1 M) for 20 h. After finishing the exchange, the sample was centrifuged and the solid was washed with 20 mL of water (3x) and then re-dispersed in 15 mL of the corresponding Ln-containing solution (80 mM) at pH 5.5 and stirred for 24 h. After this procedure, the dispersion was dialyzed against 1 L of water (3x). The obtained solution was freeze dried and the resulting powder was collected as Ln-LTL-L samples.

**Ion relocation.** The ion relocation was done in a standard calcination oven. The Ln-LTL-L samples were put in porcelain crucibles and heated to 100 °C at a rate of 1 °C/min in order

to allow the water in the zeolite to escape slowly without damaging the structure. Then the samples were heated to the desired temperature (400 or 600 °C) at a rate of 10 °C/min. After reaching the temperature, it was kept constant for 6 h. Then the oven was turned off and left to cool to room temperature. The calcined zeolites were stored in ambient atmosphere for rehydration and they were named Ln-LTL-C.

**Extraction.** 1.4 g of the Ln-LTL-C samples were dispersed in 15 mL of saturated aqueous NH<sub>4</sub>Cl solution. After stirring for 72 h the dispersion was centrifuged and the solid was washed with 20 mL of water (3x). The re-dispersed sample was then freeze dried to obtain the final Ln-LTL-E product. A detailed investigation indicated that the extraction was already finished after 24 h. Already after this shorter period more than 90% of the Ln ions were extracted and no change in the following 48 h could be found. The so obtained material could be reloaded with another or the same lanthanide according to the above-described loading procedure. The NaCl exchange step was not repeated in the second round of loading, because it can be expected that there are only loosely bound NH<sub>4</sub><sup>+</sup> ions present in the channels. The obtained reloaded material was named Ln-LTL-R.

**Stability study.** The assessment of Gd<sup>3+</sup> leaching of the Gd-LTL-L sample was performed with aqueous Gd-LTL-L dispersions. For this purpose, a defined amount of Gd-LTL-L was dispersed in 5 mL aqueous incubation medium and sonicated for 10 min in an ultrasonic bath. The dispersion was divided into 4 portions and kept in a thermo-shaker at 37°C for defined amounts of time. After the incubation time the zeolite dispersion was centrifuged at 13.2k rpm for 5 min and the supernatant was tested for free Gd<sup>3+</sup> by a colorimetric essay described by Barge et al.<sup>28</sup> In short, 100 µL of the supernatant was thoroughly mixed with 1 mL of a freshly prepared acetate buffered xylenol orange solution. Then the absorption spectrum was measured in the spectral range from 350 to 600 nm. The ratio of the absorptions at 573 nm and 433 nm was calculated and used to determine the Gd<sup>3+</sup> concentration via a calibration curve, measured in the same way with Gd<sup>3+</sup> stock solutions of known concentrations. The detectable concentrations of Gd<sup>3+</sup> were in a range of 4 to 50 µM with an error of ± 2.5 µM. In Table 4.2 the results of the measurements are summarized for the incubation in water at different pH and for the incubation in NaH<sub>2</sub>PO<sub>4</sub>. The initial Gd<sup>3+</sup> concentration of the Gd-LTL-L dispersions was calculated from the amount of zeolite that was subjected to extraction and the free Gd concentration is the concentration that was found in the supernatant after the extraction, all experiments were repeated in triplo and the values displayed are averaged

results. The only significant leaching (above the error and limit of detection) was found after 24 h of incubation in an HCl solution at pH 4.

## References

1. Database of Zeolite Structures Database of Zeolite Structures [www.iza-structure.org](http://www.iza-structure.org) (10/2013).
2. Čejka, J.; van Bekkum, H.; Corma, A.; Schueth, F., *Introduction to Zeolite Science and Practice*. 3<sup>rd</sup> Revised Ed.; Elsevier B.V.: Amsterdam, the Netherlands, **2007**.
3. van Bekkum, H.; Kouwenhoven, H. W., *Zeolite Manual for the Organic Chemist*. Mijnbestseller.nl: 2012.
4. Le Van Mao, R.; Vu, N. T.; Xiao, S.; Ramsaran, A. *J. Mater. Chem.* **1994**, 4, (7), 1143-1147.
5. Scherzer, J. *Catal. Rev.* **1989**, 31, (3), 215-354.
6. Csajbók, É.; Bányai, I.; Vander Elst, L.; Muller, R. N.; Zhou, W.; Peters, J. A. *Chem. Eur. J.* **2005**, 11, (16), 4799-4807.
7. Platas-Iglesias, C.; Vander Elst, L.; Zhou, W.; Muller, R. N.; Geraldes, C. F. G. C.; Maschmeyer, T.; Peters, J. A. *Chem. Eur. J.* **2002**, 8, (22), 5121-5131.
8. Tsotsalas, M.; Busby, M.; Gianolio, E.; Aime, S.; De Cola, L. *Chem. Mater.* **2008**, 20, (18), 5888-5893.
9. Caravan, P.; Ellison, J. J.; McMurry, T. J.; Lauffer, R. B. *Chem. Rev.* **1999**, 99, (9), 2293-2352.
10. Aime, S.; Cabella, C.; Colombatto, S.; Geninatti Crich, S.; Gianolio, E.; Maggioni, F. *J. Magn. Res. Imaging* **2002**, 16, (4), 394-406.
11. Newell, P. A.; Rees, L. V. C. *Zeolites* **1983**, 3, (1), 22-27.
12. Balkus Jr., K. J.; Sherry, D. A.; Young, S. W. Zeolite-enclosed transistion and rare earth metal ions as contrast agents for the gastrointestinal tract. 1992.
13. Rubin, D. L.; Falk, K. L.; Sperling, M. J.; Ross, M.; Saini, S.; Rothman, B.; Shellock, F.; Zerhouni, E.; Stark, D.; Outwater, E. K.; Schmiedl, U.; Kirby, L. C.; Chezmar, J.; Coates, T.; Chang, M.; Silverman, J. M.; Rofsky, N.; Burnett, K.; Engel, J.; Young, S. W. *J. Magn. Res. Imaging*, **1997**, 7, (5), 865-872.
14. Young, S. W.; Qing, F.; Rubin, D.; Balkus, K. J.; Engel, J. S.; Lang, J.; Dow, W. C.; Mutch, J. D.; Miller, R. A. *J. Magn. Res. Imaging*, **1995**, 5, (5), 499-508.
15. Bünzli, J.-C. G. *Chem. Rev.* **2010**, 110, (5), 2729-2755.
16. Norek, M.; Neves, I. C.; Peters, J. A. *Inorg. Chem.* **2007**, 46, (15), 6190-6196.
17. Peters, J. A.; Djanashvili, K. *Eur. J. Inorg. Chem.* **2012**, 2012, (12), 1961-1974.
18. Corsi, D. M.; Platas-Iglesias, C.; van Bekkum, H.; Peters, J. A. *Magn. Reson. Chem.* **2001**, 39, (11), 723-726.
19. Horrocks, W. D.; Sudnick, D. R. *J. Am. Chem. Soc.* **1979**, 101, (2), 334-340.
20. Gillis, P.; Peto, S.; Muller, R. N. *Magn. Res. Imaging* **1991**, 9, (5), 703-708.
21. Kubíček, V.; Rudovský, J.; Kotek, J.; Hermann, P.; Vander Elst, L.; Muller, R. N.; Kolar, Z. I.; Wolterbeek, H. T.; Peters, J. A.; Lukeš, I. *J. Am. Chem. Soc.* **2005**, 127, (47), 16477-16485.
22. Rehor, I.; Kubicek, V.; Kotek, J.; Hermann, P.; Lukes, I.; Szakova, J.; Vander Elst, L.; Muller, R. N.; Peters, J. A. *J. Mater. Chem.* **2009**, 19, (10), 1494-1500.
23. Vitha, T.; Kubíček, V. c.; Hermann, P.; Elst, L. V.; Muller, R. N.; Kolar, Z. I.; Wolterbeek, H. T.; Breeman, W. A. P.; Lukeš, I.; Peters, J. A. *J. Med. Chem.* **2008**, 51, (3), 677-683.
24. Bloembergen, N.; Morgan, L. O. *J. Chem. Phys.* **1961**, 34, 9.
25. Solomon, I. *Physical Review* **1955**, 99, (2), 559-565.

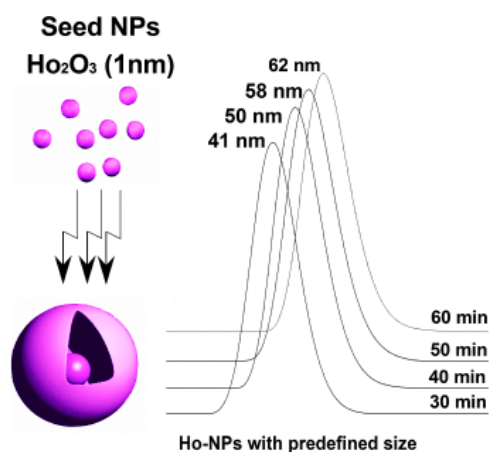


26. Caro, J.; Höcevar, S.; Kärger, J.; Riekert, L. *Zeolites* **1986**, 6, (3), 213-216.
27. Tse, N. M. K.; Kennedy, D. F.; Kirby, N.; Moffat, B. A.; Muir, B. W.; Caruso, R. A.; Drummond, C. J. *Adv. Healthcare Mater.* **2013**, 2, (6), 836-845.
28. Barge, A.; Cravotto, G.; Gianolio, E.; Fedeli, F. *Contrast Med. Mol. Imaging* **2006**, 1, (5), 184-188.

---

# Microwave Assisted Seeded Growth of Lanthanide-Based Nanoparticles for Imaging and Therapy

# 5



## Introduction

Nanoparticulate systems have shown potential in various medical applications, including imaging, cell tracking, drug delivery, and therapy.<sup>1</sup> Systems based on lanthanides are of special interest because the members of this fascinating group of elements combine a large chemical similarity with a great variety in physical properties. This combination opens avenues in medical imaging, therapy, and combinations thereof (theranostics).<sup>2</sup> In tumor diagnosis and therapy, nanosized particulates are favorable devices because they tend to accumulate in tumors more than they do in healthy tissues through the so-called Enhanced Permeability and Retention (EPR) effect.<sup>3</sup> The chemical and physical behavior of nanoparticles (NPs) is governed by their high surface-to-volume ratio, which renders their properties depending on size and shape. In this respect they are different from the corresponding bulk materials. Based on this phenomenon, superparamagnetic iron oxide NPs have already been successfully applied as contrast agents (CAs) in magnetic resonance imaging (MRI).<sup>4</sup> The high magnetization of these particles reduces the transverse relaxation time ( $T_2$ ) of water in their neighborhood resulting in contrast enhancement in the obtained MR images.

Previously, we have demonstrated the great potential of paramagnetic lanthanide oxide NPs as MRI CAs.<sup>5-7</sup> These particles have a very high density of  $\text{Ln}^{3+}$  ions and therefore, exhibit a strong magnetization in external magnetic fields. In contrast to the iron oxide particles, the magnetization of these materials does not show saturation at higher magnetic fields (up to at least 30 T). Consequently, the efficiency of these particles as  $T_2$  CA, usually expressed as the  $r_2$ -relaxivity (enhancement in  $1/T_2$  per mmol of metal ion) increases with the magnetic field strength. Furthermore, several lanthanides have radioisotopes with characteristics favorable for imaging and/or therapy, which offers perspectives for combinations of MRI with nuclear imaging (PET/SPECT) and/or therapy.<sup>8,9</sup> An example of such a multimodal approach is the application of  $^{166}\text{Ho}$ , which next to its interesting magnetic properties, is a  $\beta$ - and  $\gamma$ -emitter ( $E_{\text{max}, \beta} = 1.84$  MeV and  $E_{\text{max}, \gamma} = 80.6$  keV), suitable for radionuclide therapy ( $t_{1/2} = 26.8$  h, penetration depth of 3.2 mm) and gamma imaging, respectively. Clinical trials demonstrated the effectiveness of  $^{166}\text{Ho}$ -containing microspheres in the radio-treatment of tumours<sup>10</sup> and arthritis.<sup>11</sup> Their treatment involves direct injection

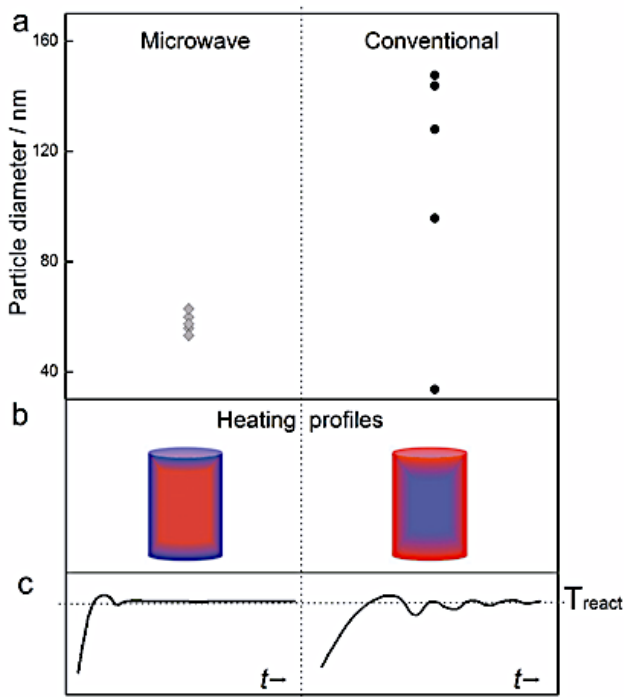


**Figure 5.1.** Comparison of two sets of five different batches of Ho-NPs prepared with heating in microwave (left) and oil bath (right): a) mean diameters; schematic representation of temperature (b) and heating (c) profiles.

of microspheres into diseased tissue or blood vessels surrounding it, which is a clinically applied treatment nowadays. Those spheres can simultaneously be visualized by MRI. However, this procedure is restricted to a small number of reachable tumours.<sup>12,13</sup> In order to make the combination of therapy and MRI also applicable to other tissues it is desirable to have access to NPs that are small enough to pass the capillary system and yet show high magnetization. A maximum of magnetization was previously determined for lanthanide NPs of 120-140 nm diameter.<sup>5</sup> But for a definition of the optimal size of a nanoparticulate probe for in vivo applications more parameters besides the size-dependence of chemical and physical properties need to be considered, such as biodistribution and pharmacokinetics. Optimization of these often opposing parameters needs to be compromised by fine-tuning of the size, but doing so in a reproducible way remains a bottleneck.

## Results and Discussion

Methods described in the literature on the preparation of lanthanide NPs often concern hydro(solvo)thermal synthetic procedures that involve high temperatures/pressures, and most importantly, result in NPs of either non-spherical shape (rods, wires, cubes) or ultrasmall size ( $<10$  nm).<sup>14,15</sup> One of the simplest procedures to produce spherical Ln-containing NPs is the precipitation from homogeneous solution of the corresponding lanthanide chloride upon hydrolysis of urea.<sup>16,17</sup> In our hands, however, good results were

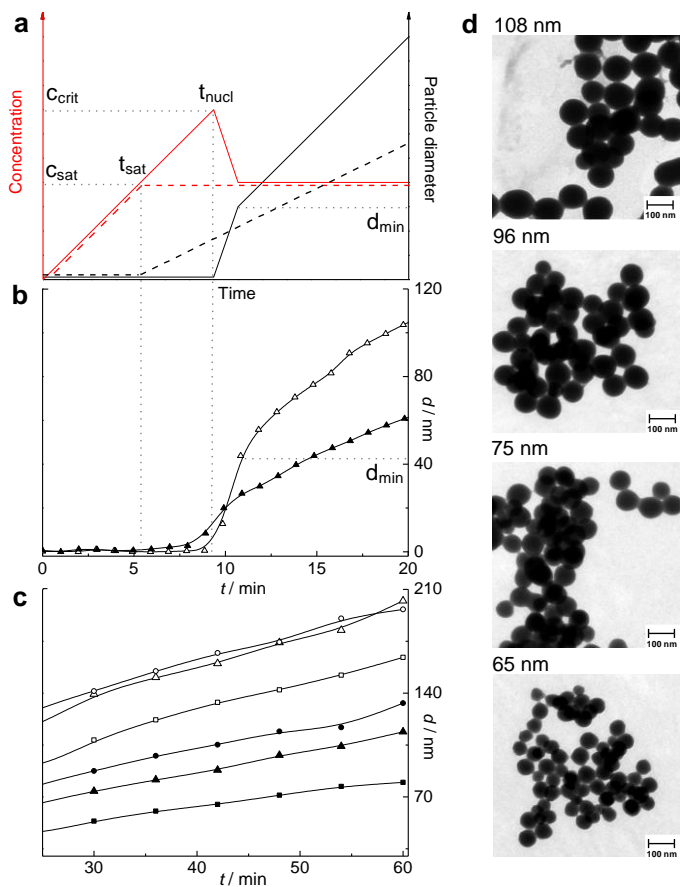


**Figure 5.2.** Investigation of the growing process: a) theoretical considerations show a significant difference between homogeneous (solid) and heterogeneous (dashed) nucleation; in situ DLS experiments: b) nucleation process in the presence (▲) or absence (Δ) of small seed particles (SSP) at 77 °C; c) the growing process was investigated at 73, 74 and 75 °C (■, ▲, ◆ with, and □, Δ, ◇ without SSP) by stopping microwave experiments at different times; d) TEM images of NPs of different sizes.

obtained with individual experiments, but the reproducibility appeared to be low; the average sizes of repeated experiments varied over a range of more than 100 nm (Figure 5.1). The inhomogeneity of conventional heating during hydrolysis of urea was envisioned to be the main cause of the irreproducibility. Therefore, microwave heating was applied instead. This change significantly improved the reproducibility of the particle sizes, but the diameter range of 20-50 nm was still not accessible. An explanation for this phenomenon was found in the mechanism of homogeneous nucleation.<sup>18,19</sup> At constant temperatures, a steady rate of hydrolysis can be assumed, resulting in a linear increase of solute concentration (Figure 5.2a, red solid line). In the case of homogeneous precipitation nuclei have to be formed first. This process has a positive  $\Delta G$  below  $c_{crit}$ , and therefore, concentrations higher than the saturation concentration ( $c_{sat}$ ) are required. Only when the critical concentration ( $c_{crit}$ ) is reached, stable nuclei can be formed, and precipitation starts rapidly in the supersaturated solution. Re-establishment of the equilibrium leads to a drop of the concentration back to  $c_{sat}$  accompanied by a fast precipitation and a jump in particle size from 0 to  $d_{min}$  (black solid line). Therefore, particles with the sizes below  $d_{min}$  cannot be prepared from homogeneous solutions. To circumvent this abrupt rise in particle diameter upon nucleation small seed particles (SSP) were employed to push the process towards the mechanism of heterogeneous nucleation (Figure 5.2b).

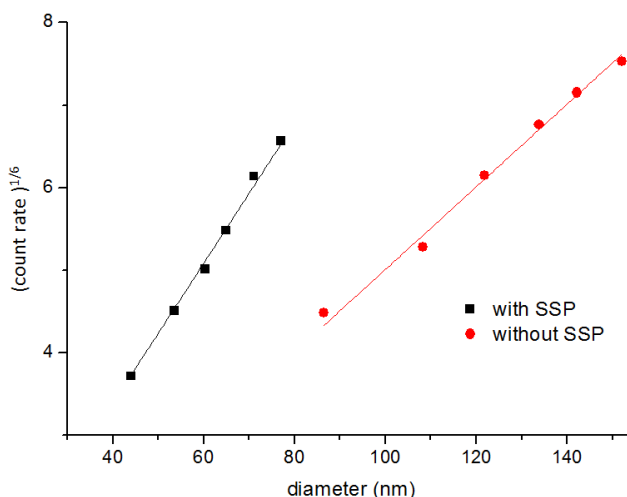


**Figure 5.3.** Plot of  $\sqrt[6]{\text{count rate}}$  vs diameter to estimate the number of particles that were produced during the precipitation reaction.

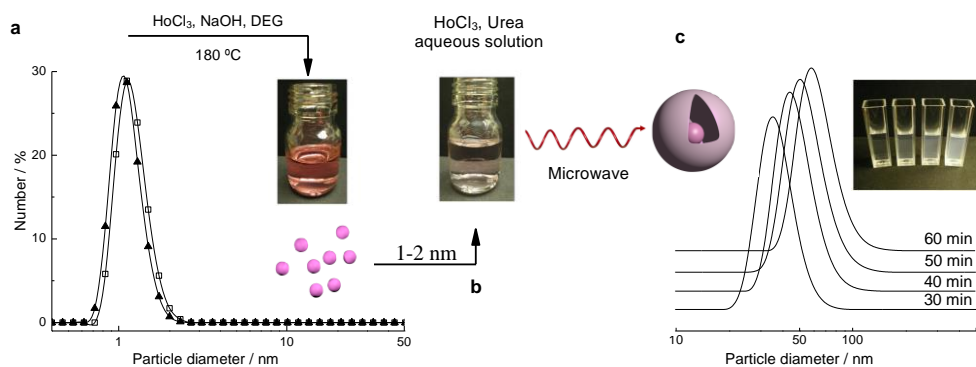


**Figure 5.4.** Schematic representation of the two-step synthetic procedure: a) the DLS patterns of Ho<sub>2</sub>O<sub>3</sub> (□) and Dy<sub>2</sub>O<sub>3</sub> (▲) particles show a narrow size distribution around 1-2 nm; b) the seed particles in DEG are added to an aqueous solution of urea and HoCl<sub>3</sub> to form the final reaction mixture for the subsequent heating in a laboratory microwave oven to a defined temperature; c) DLS analysis of the dialyzed NPs demonstrates the size-dependence of the reaction time: at 72 °C the obtained diameters are 40.7, 49.5, 57.5 and 62.4 nm with aging for 30, 40, 50 and 60 min, respectively.

After reaching the saturation concentration ( $c_{\text{sat}}$ ) precipitation starts instantaneously on the surface of the SSP (red dashed line). Therefore, concentrations higher than  $c_{\text{sat}}$  are never reached and the risk of secondary nucleation is minimal. This was further investigated by the correlation of the measured light scattering intensities to the obtained particle diameters. The intensity of the light scattering increases with the 6<sup>th</sup> power in dependence of the diameter ( $I \sim d^6$ ). Therefore, a plot of count rate (CR)<sup>1/6</sup> vs diameters obtained from DLS measurements will result in a straight line, if the other factors contributing to the intensity of light scattering (number of particles, wavelength of the light, refractive index) are constant (Figure 5.3). The linear correlation clearly displays that the increase of light scattering is only attributed to the growth of the particles, therefore indicating that there are no new particles formed after the growing process starts. This is well in agreement with the theory (Figure 5.2) because nucleation takes place at higher concentrations ( $c_{\text{nucl}}$ ) than what is maintained during the growing step ( $c_{\text{sat}}$ ) in the case of homogeneous as well as heterogeneous nucleation. The different slopes of the fittings (0.0501 for homogeneous and 0.0848 for heterogeneous), however, indicate that there is an important difference in the two methods in general. As all factors determining the light scattering are the same, except for the number of particles, we attribute this difference to a much higher number of particles in the seeded method than

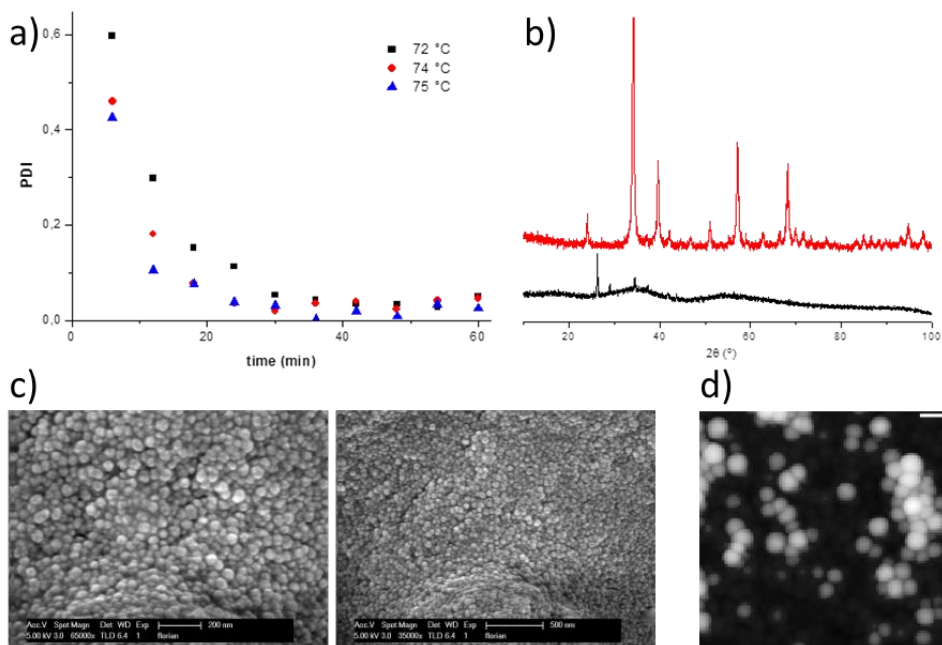


**Figure 5.5.** Development of the PDI during the reaction. For narrow size distributions a reaction time of >30 min is optimal (a). XRD patterns of the particles before (black) and after (red) calcination. The transition from amorphous material to crystalline  $\text{Ho}_2\text{O}_3$  is clearly visible (b). SEM (c) and AFM (d) images of the particles. Scale bars represent 200 (left) and 500 nm (right) in the SEM images and 200 nm in the AFM image.

what is obtained in the non-seeded method. The ratio can be calculated by dividing the slopes while keeping in mind that the scattering increases with the 6<sup>th</sup> power of the diameter. With this method we found that the number of particles is more than 20 times higher with our method than with the homogeneous precipitation method without seed particles.

Based on these considerations, the newly developed procedure proves to be a facile, highly reproducible method for the preparation of Ln-based NPs with predefined diameters in the range of 20 to 200 nm. As seed particles we chose small lanthanide oxide particles that were prepared according to the polyol procedure described by Bridot *et al.*<sup>20</sup> A defined amount of the obtained dispersion was added directly to an aqueous solution of urea and the corresponding lanthanide chloride. This mixture finally was heated in a microwave oven to induce hydrolysis of the urea resulting in formation of ammonium carbonate (Figure 5.4). As soon as the solubility product was reached, poorly soluble Ln(III)-carbonate precipitated initiating the growth of the present nuclei. By adjusting the applied conditions (temperature



and time) the size of the obtained particles was easily tunable, *e.g.*, for Ln = Ho and  $T = 73$  °C, the mean diameters obtained turned out to be 53.6, 71.1 and 79.8 nm, after 30, 48 and 60 min, respectively (Figure 5.2c). This corresponds to averaged growth rate of less than 1 nm/min, which is reasonably fast and at the same time slow enough to allow accurate size-control. When the desired size was reached, the precipitation was quenched by rapid cooling, followed by removal of the remaining Ln(III)-salts and urea via dialysis. A minimum reaction time of 30 min was found to be favorable because the polydispersity index (PDI) dramatically dropped during the first 30 min before reaching a constant low value ( $< 0.1$ ) (Figure 5.5a). As shown in Figure 5.2c, variations of temperature by only 1 °C give rise to significant differences in the precipitation rate. This underscores the importance of accurate temperature control for obtaining reproducible results. The constant growth rate suggests that the seeds grow uniformly, and dynamic light scattering (DLS) experiments indicate that no new crystal nuclei are formed during this process to preserve the narrow size distribution. To show the universal applicability of the method, the experiments were repeated with dysprosium, instead of holmium. No statistically relevant changes in the obtained sizes were found when the same conditions were applied.

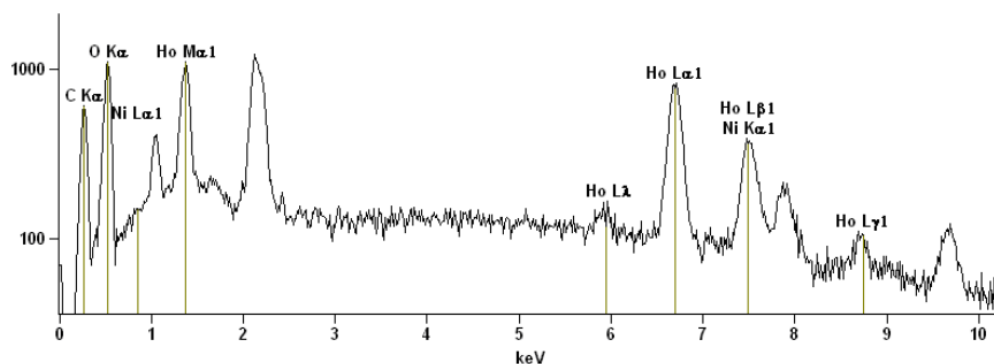


**Figure 5.6.** EDX spectrum of  $\text{Ho}_2(\text{CO}_3)_3$  particles after freeze drying. The signals at 2.2 and 9.8 keV represent the Au  $M_\alpha$  and the Au  $L_\alpha$  energies, respectively (from sputtering the sample with gold). The quantitative analysis of the data indicates a holmium content of  $57.6 \pm 0.8\%$  (w/w) (theory  $\text{Ho}_2(\text{CO}_3)_3 \cdot \text{H}_2\text{O}$ : 62.5% (w/w)). This difference can be ascribed to some remaining urea after the dialysis.

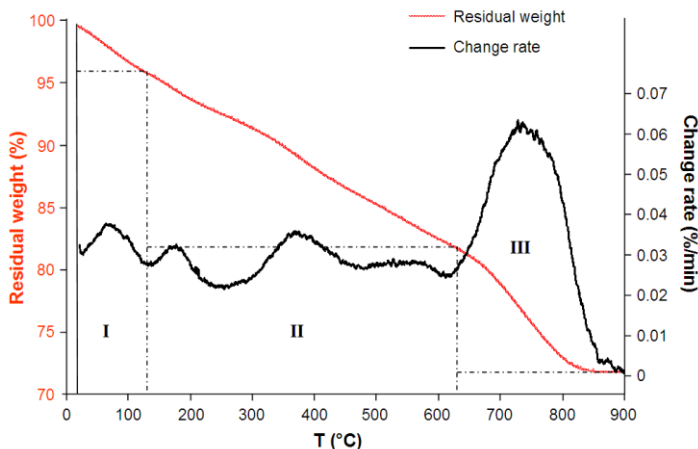


**Figure 5.7.** Thermo-gravimetric analysis of freeze-dried holmium nanoparticles.

After dialysis the particles show a high  $\zeta$ -potential (about +40 mV) and they were stable in water for weeks without any changes in DLS pattern or  $\zeta$ -potential. TEM, SEM and AFM showed that the NPs were perfectly spherical and homogeneous with diameters that were in good agreement with those measured by DLS (Figures 5.2 and 5.5). Energy dispersive X-ray spectroscopy (EDX) of the Ho-NPs showed the Ho-content to be 58% (w/w) (Figure 5.6), which is in reasonable agreement with the calculated value for  $\text{Ho}_2(\text{CO}_3)_3 \cdot \text{H}_2\text{O}$  (62.5%). The thermogravimetric (TGA) profile exhibited a continuous loss of weight between room temperature and 820 °C (Figure 5.7). The total weight loss (28.1%) compares well with the loss of 28.4% calculated for the transition of  $\text{Ho}_2(\text{CO}_3)_3 \cdot \text{H}_2\text{O}$  to  $\text{Ho}_2\text{O}_3$ . Because the particles are amorphous, the transitions are not very sharp but stretch over a wide temperature range. However, it is still possible to divide the profile in three discrete parts. The first step displays the loss of the water that is included in the material and is completed at 120 °C. The second step represents the decomposition of two (of the three) carbonate anions. It stretches over more than 500 °C and finishes at 630 °C. In the last step, all the remaining carbonates are decomposing and the pure and crystalline  $\text{Ho}_2\text{O}_3$  is formed. A similar TGA profile has been reported for Dy-carbonate.<sup>13,21</sup> The powder XRD pattern of freeze-dried samples (Figure 5.5b) showed no reflections corresponding to  $\text{Ho}_2(\text{CO}_3)_3$ ; only two broad humps were observed at about 35 and 55° 2 $\theta$ , respectively. This is typical for amorphous spherical particles. Similar XRD patterns have been reported for amorphous spherical Gd- and Dy-

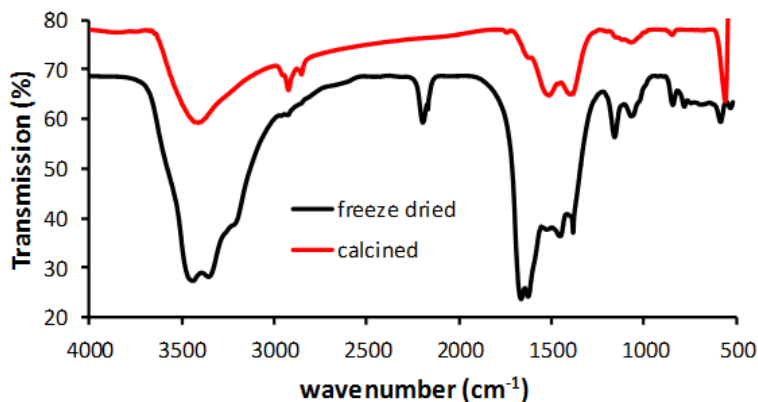


**Figure 5.8.** FT-IR spectra of freeze dried and calcined particles.

carbonate particles.<sup>13,22</sup> After calcination of the sample at 800 °C for 1 h, the XRD spectrum displayed sharp reflections typical for  $\text{Ho}_2\text{O}_3$ . FT-IR spectra of the solids obtained after freeze drying and after calcining the particles are displayed in Figure 5.8. They confirm the presence of minor amounts of urea that was found with EDX analysis. But the typical  $\text{Ho}_2(\text{CO}_3)_3$  absorption bands are clearly present at 3300 – 3400 ( $\nu_{\text{OH}}$ ) and 846  $\text{cm}^{-1}$  ( $\nu_{\text{CO}_3}$ ).<sup>21</sup> After calcination at 650 °C, the spectrum changed dramatically. The appearance of a strong peak at 550  $\text{cm}^{-1}$  is typical for  $\text{Ho}_2\text{O}_3$ .<sup>23</sup> The remaining carbonate peaks after calcination at 650 °C suggest that this temperature is not sufficient to convert the entire carbonate into oxide. This is also supported by TGA, where the last transition takes place at  $T > 650$  °C (Figure 7).

The suitability of the particles under study as MRI contrast agent was tested on a 0.25 mM ( $\text{Ho}^{3+}$  concentration) aqueous suspension of the extensively dialyzed particles with diameters of 41, 69 and 81 nm. The concentration was determined via the BMS (bulk magnetic susceptibility, BMS) method.<sup>24</sup> Insertion of the sample into a strong magnetic field (7.0T) was accompanied by spontaneous precipitation of the particles. Obviously, the  $\zeta$ -potential of +42 mV was not sufficient to prevent coagulation in the magnetic field gradients during the insertion of the sample. Upon the addition of 0.05% (w/w) of the cationic surfactant cetyl trimethyl ammonium bromide (CTAB) to the dispersion, the  $\zeta$ -potential could be increased to +65 mV, while the viscosity of the sample remained low.

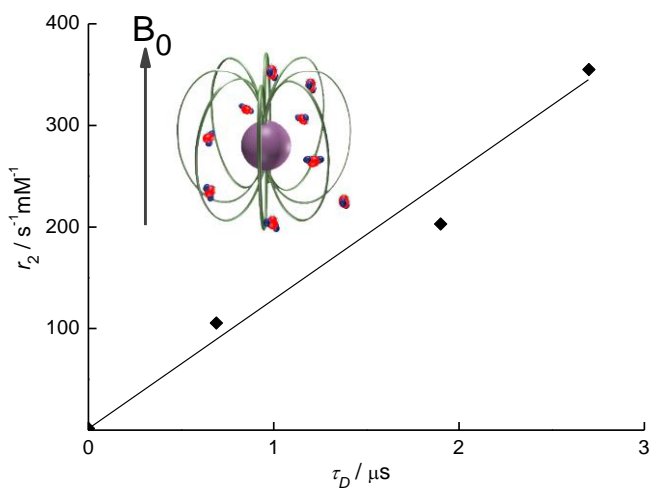


**Figure 5.9.** Size-dependent magnetic behavior of Ho-containing NPs. The magnetic field inhomogeneities created by the magnetized NPs cause rapid  $r_2$  relaxation of  $^1\text{H}$  nuclei of the water molecules diffusing along the NPs (the inset image), resulting in dark spots for water molecules close to the NPs in  $T_2$ -weighted MR images.  $r_2$  (at  $B_0 = 7$  T) is represented as a function of the estimated diffusion correlation time  $\tau_D$  ( $\tau_D = r_c^2/D$ , where  $r_c$  is the radius of core of the particle,  $D = 2.5 \times 10^{-9} \text{ m}^2 \text{ s}^{-1}$  is the diffusion coefficient of water at 25 °C).  $\tau_D = 0$  represents in theory particles with a diameter of 0 nm, which is realized by a solution of  $\text{HoCl}_3$ .

This was sufficient to stabilize the particles in dispersion in magnetic fields for more than two hours without any observable aggregation or precipitation as demonstrated by DLS and relaxivity measurements. The transverse relaxivities ( $r_2$ ) of these samples at 7T, shown in Figure 9, increase linearly with the particle size, and are expected to increase even further as function of the magnetic field, as predicted earlier for  $\text{Dy}_2\text{O}_3$ .<sup>6</sup> This makes Ho-containing NPs promising devices for high field MRI combined with radiotherapy.

## Conclusions

In conclusion, microwave-assisted seeded-growth is a highly reproducible method to prepare uniform spherical NPs composed of stable amorphous Ln-carbonates. For *in vivo* applications, a biocompatible coating will be required to prevent leaching of  $\text{Ho}^{3+}$ -ions; procedures to craft a silica shell around the particle have already been described in literature.<sup>5,16,20</sup> The accessible size range is suitable for  $T_2$  MR imaging as the particles show extremely high transversal relaxation enhancement of the water protons. As the particle

diameters can be easily tuned by the adjustment of temperature and aging time, the desired compromise between the MRI performance and the biodistribution can be realized.

## Experimental details

**Dynamic light scattering** was done on a Zetasizer Nano ZS from Malvern Instruments Ltd (Malvern, UK). The machine is equipped with a 4.0 mW, 633 nm He-Ne Laser and the 173° back-scatter mode was used to analyze the obtained particles. The multiple-peak fitting procedure implemented in the Software for Zetasizer (Version 6.12) was used to evaluate the autocorrelation function. All diameters are given as number weighted mean values of the obtained particle size distributions. The same machine was used for  $\zeta$ -potential measurements. For these measurements, polystyrene cuvettes with gold plated electrodes (MA DTS 1060) were used. Dispersions for the measurements were used as obtained after dialysis.

**Microscopy.** TEM images were taken on a Zeiss EM 10 transmission electron microscope with 80 kV acceleration voltage. Samples were prepared by dipping copper grids into the dispersion twice and afterwards leaving them to dry for at least one hour at room temperature. SEM images were taken on a Philips XL30 scanning electron microscope in ultra-high resolution mode at a voltage of 5 kV. EDX investigations were done on a JEOL JSM-840 scanning electron microscope. Samples were prepared from freeze dried particles that were fixed on conductive tape and sputtered with a gold layer for better conductivity. AFM was performed on an Ntegra atomic force microscope in semicontact (tapping) mode.

**X-ray diffraction** patterns of freeze dried  $\text{Ho}_2(\text{CO}_3)_3$  particles and calcined samples were measured using a Bruker D8 Advance diffractometer equipped with a Lynxeye detector and  $\text{Cu-K}_\alpha$  radiation. The measuring ranges from 5 to 95 °2 $\theta$  with a step size of 0.02 °2 $\theta$  and a scan speed of 0.15 s<sup>-1</sup>.

**Thermogravimetry** was measured using a Perkin–Elmer TGA7 thermogravimetric analyser. The measurements were performed in air. The temperature range investigated was from 25 to 900 °C at a heating rate of 10 °C/min. The sample consisted of freeze-dried particles and the initial weight was typically between 4 and 10 mg.

**BMS and relaxivity** measurements were done on a Varian Unity Inova 300 NMR machine. Concentrations were determined using the bulk magnetic susceptibility method with t-

butanol as the reference. For BMS measurements 400  $\mu\text{L}$  of the dispersion were diluted with 50  $\mu\text{L}$  of conc. HCl to dissolve the particles and 50  $\mu\text{L}$  *tert*-butanol were added. The induced shift was measured against water and *tert*-butanol in a standard inner tube that was added to the sample tube. The concentration was calculated from the shift following the procedure described in literature.<sup>24</sup> Water proton transfers relaxation times  $T_2$  were determined from 0.25 mM aqueous dispersions of particles of different sizes using the Carr-Purcell-Meiboom-Gill pulse sequence (CPMG) with the interval between two refocusing pulses ( $\tau_{\text{CP}}$ ) of 1 ms. The experimental values of relaxation rates were corrected for diamagnetic contributions of pure water ( $0.5 \text{ s}^{-1}$ ).

**IR spectra** were taken on a Perkin Elmer Spectrum One FT-IR spectrometer. Samples were prepared by mixing the proper number of freeze-dried particles with dry KBr and pressing it in the form of a pellet.

**Synthesis of small seed particles.**  $\text{LaCl}_3 \cdot 6\text{H}_2\text{O}$ ,  $\text{DyCl}_3 \cdot 6\text{H}_2\text{O}$ , or  $\text{HoCl}_3 \cdot 6\text{H}_2\text{O}$  (Strem Chemicals) were dissolved in 8% hydrochloric acid. The solutions obtained were filtered over a 200  $\mu\text{m}$  Nylon syringe filter (Rotilabo) and evaporated until dryness in high vacuum before use. The resulting material ( $\text{LnCl}_3 \cdot 6\text{H}_2\text{O}$ , 4 mmol) was added to 20 mL of diethylene glycol (DEG) and the solution was stirred at ambient temperature for 30 min. After addition of 1 mL aqueous NaOH (3 M), the mixture was heated to 140  $^\circ\text{C}$  and stirred for 1 h. Next, the temperature was increased to 180  $^\circ\text{C}$  and after another 5.5 h, the clear solution obtained was slowly cooled to room temperature and then filtered over a 200  $\mu\text{m}$  Nylon syringe filter (Rotilabo).

**Growing of bigger particles with predefined size.** To 50 mL of a solution containing  $\text{LnCl}_3$  (0.02 M) and urea (1 M), 200  $\mu\text{L}$  of the suspension of small particles in DEG were added. The mixture was filtered (Rotilabo Nylon syringe filter, 200  $\mu\text{m}$ ), transferred into a teflon microwave container XP1500 (50 mL), and heated in a Mars5 microwave oven by CEM Corp. equipped with an EST-300 temperature sensor. The temperature was increased up to the reaction temperature within 5 min and maintained at that value for a predefined time. After finishing, the reaction was quenched by rapid cooling to 0  $^\circ\text{C}$ . The obtained bluish opaque dispersions were dialyzed against demineralized water ( $3 \times 500 \text{ mL}$ , cellulose membrane, molecular weight cut off 12.7 kDa) for one day. A yield of typically 20-40 mg of  $\text{Ln}_2(\text{CO}_3)_3$  NPs, depending on the size, was obtained.

**Preparation of particles applying conventional heating.** A solution (50 mL) was prepared containing urea (1 M) and  $\text{LnCl}_3$  (0.02 M). This solution was divided in 5 portions. Those portions were filtered and transferred to a round bottom flask equipped with a magnetic stirring bar. Then the flasks were put into a preheated oil bath of 75 °C. After 45 min the reactions were quenched by rapidly cooling the dispersions to 0 °C. The obtained particle sizes were determined by DLS.

**In situ DLS experiments.** To investigate the nucleation process in situ DLS measurements were performed. 2 mL of the reaction mixture (as described above) were put in a Quartz UV/Vis-cuvette, placed into the preheated sample chamber (77 °C) of the DLS machine and the measurement was started immediately and repeated every minute. Every measurement consisted of 4 runs of 10 seconds each. This was enough to measure the intensity of light scattering, but not sufficient to give reliable results in respect to size and PDI. Therefore, after 25 min a longer measurement (20 scans) was carried out. The herewith determined size was used to calculate the diameter for all the previous measurements from the total count rate, using the relation  $d = c \cdot \sqrt[6]{\text{count rate}}$  (d= diameter, c= constant).

## References

1. Lavik, E.; von Recum, H. *ACS Nano* **2011**, 5, (5), 3419-3424.
2. Lammers, T.; Aime, S.; Hennink, W. E.; Storm, G.; Kiessling, F. *Acc. Chem. Res.* **2011**, 44, (10), 1029-1038.
3. Torchilin, V. *Adv. Drug Del. Rev.* **2011**, 63, (3), 131-135.
4. Laurent, S.; Bridot, J.-L.; Vander Elst, L.; Muller, R. N. *Future Med. Chem.* **2010**, 2, (3), 427-449.
5. Norek, M.; Kampert, E.; Zeitler, U.; Peters, J. A. *J. Am. Chem. Soc.* **2008**, 130, (15), 5335-5340.
6. Norek, M.; Pereira, G. A.; Geraldles, C. F. G. C.; Denkova, A.; Zhou, W.; Peters, J. A. *J. Phys. Chem. C* **2007**, 111, (28), 10240-10246.
7. Norek, M.; Peters, J. A. *Prog. Nucl. Magn. Reson. Spectrosc.* **2011**, 59, (1), 64-82.
8. Rösch, F. *Radiochim. Acta* **2007**, 95, (6), 303.
9. Rösch, F.; Baum, R. P. *Dalton Trans.* **2011**, 40, (23), 6104-6111.
10. Smits, M.; Nijsen, J.; van den Bosch, M.; Lam, M.; Vente, M.; Huijbregts, J.; van het Schip, A.; Elschot, M.; Bult, W.; de Jong, H.; Meulenhoff, P.; Zonnenberg, B. *J. Exp. Clin. Cancer Res.* **2010**, 29, (1), 70.
11. Song, J. S.; Suh, C. H.; Park, Y. B.; Lee, S. H.; Yoo, N. C.; Lee, J. D.; Kim, K. H.; Lee, S. K. *Eur. J. Nucl. Med.* **2001**, 28, (4), 489-497.
12. Johnson, N. J. J.; Oakden, W.; Stanisz, G. J.; Scott Prosser, R.; van Veggel, F. C. J. *M. Chem. Mater.* **2011**, 23, (16), 3714-3722.
13. Tian, Y.; Tian, J.; Li, X.; Yu, B.; Shi, T. *Chem. Commun.* **2011**, 47, (10), 2847-2849.
14. Bult, W.; Seevinck, P. R.; Krijger, G. C.; Visser, T.; Kroon-Batenburg, L. M. J.; Bakker, C. J. G.; Hennink, W. E.; van het Schip, A. D.; Nijsen, J. F. W. *Pharmaceutical Research* **2009**, 26, (6), 1371-1378.
15. Vente, M. A. D.; Nijsen, J. F. W.; Wit, T. C.; Seppenwoolde, J. H.; Krijger, G. C.; Seevinck, P. R.; Huisman, A.; Zonnenberg, B. A.; Ingh, T. S. G. A. M.; van het Schip, A. D. *Eur. J. Nucl. Med. Mol. Imag.* **2008**, 35, (7), 1259-1271.
16. Happy; Tok, A. I. Y.; Su, L. T.; Boey, F. Y. C.; Ng, S. H. *J. Nanosci. Nanotechnol.* **2007**, 7, (3), 907-915.
17. Xu, Z.; Gao, Y.; Huang, S.; Ma, P. a.; Lin, J.; Fang, J. *Dalton Trans.* **2011**, 40, (18), 4846-4854.
18. LaMer, V. K.; Dinegar, R. H. *Journal of the American Chemical Society* **1950**, 72, (11), 4847-4854.
19. Sugimoto, T. *Journal of Colloid and Interface Science* **2007**, 309, (1), 106-118.
20. Bridot, J.-L.; Faure, A.-C.; Laurent, S.; Rivière, C.; Billotey, C.; Hiba, B.; Janier, M.; Josserand, V.; Coll, J.-L.; Vander Elst, L.; Muller, R.; Roux, S.; Perriat, P.; Tillement, O. *J. Am. Chem. Soc.* **2007**, 129, (16), 5076-5084.
21. Ali, A. A.; Hasan, M. A.; Zaki, M. I. *Mater. Res. Bull.* **2008**, 43, (1), 16-29.
22. Li, I. F.; Su, C.-H.; Sheu, H.-S.; Chiu, H.-C.; Lo, Y.-W.; Lin, W.-T.; Chen, J.-H.; Yeh, C.-S. *Adv. Funct. Mater.* **2008**, 18, (5), 766-776.
23. McDevitt, N. T.; Baun, W. L. *Spectrochim. Acta* **1964**, 20, (5), 799-808.
24. Corsi, D. M.; Platas-Iglesias, C.; van Bekkum, H.; Peters, J. A. *Magn. Reson. Chem.* **2001**, 39, (11), 723-726.





## Summary

Since lanthanides were discovered in the 18<sup>th</sup> century, they fascinate scientists due to their similarity in chemical behavior and versatility in physical properties. It is thus not surprising, that lanthanides are part of uncountable applications in modern industry, electronics, magnets, light sources and medical applications. Especially, as the lanthanide elements are not naturally occurring in living organisms, it is essential that the molecular dynamics and chemical as well as physical properties are understood in detail for *in vivo* applications. In this thesis, different lanthanide-containing compounds and nanoparticles were investigated to gain deeper knowledge of fundamental processes governing physical properties and synthetic procedures.

In **Chapter 1**, a brief overview of the history of the lanthanides is given, including an overview of some chemical and physical properties. In the later paragraphs, applications of lanthanides in magnetic resonance, optical and radionuclide imaging, as well as radiotherapy are highlighted, the basic background concerning the chemical and physical requirements are described, and the necessary steps towards optimal imaging agents are outlined. In the following, the latest discoveries and regulatory developments with respect to toxicological concerns are briefly explained and the contributions of lanthanides to the design and development of multimodal imaging/therapeutic probes are discussed. The benefits of delivering high payloads of lanthanide ions to the site of interest are described in the last section of the chapter. Here, different types of nanoparticles are considered, ranging from porous to solid particles.

The following chapters concern studies carried out to gain deeper knowledge of the molecular dynamics in lanthanide-DOTA complexes (**Chapter 2**), the aggregation and luminescence properties of Ln-DOTA decorated calix[4]arenes (**Chapter 3**), magnetic and luminescent properties and synthesis of porous (**Chapter 4**) and solid (**Chapter 5**) nanovesicles.

In **Chapter 2** the rotation of the carboxylate groups in DOTA complexes of Ln- and Sc-ions was investigated with DFT calculations and with variable temperature <sup>17</sup>O NMR studies at 4.7-18.8 T. The data obtained show that the rotation is much slower than the other dynamic processes taking place in these complexes, such as the water exchange in the first

coordination sphere of the lanthanide ion. The exchange between the bound and unbound carboxylate oxygen atoms for the largest Ln-ions (La  $\rightarrow$  Sm) follows a pathway via a transition state in which both oxygens of the carboxylate group are bound to the Ln-ion, whereas for the smaller metal ions (Tm, Lu, Sc) the transition state has a fully decoordinated carboxylate group. The activation free energies show a steady increase from about 75 to 125-135 kJ mol<sup>-1</sup> going from La to Lu. This computed trend is consistent with the results of the <sup>17</sup>O NMR measurements. Fast exchange between bound and unbound carboxylate oxygen atoms was observed for the diamagnetic La-DOTA, whereas for Pr-, Sm-, Lu-, and Sc-DOTA the exchange was slow on the NMR timescale. The trends in the linewidths for the various metal ions as a function of the temperature agree with trend in the rates as predicted by the DFT calculations.

In **Chapter 3**, self-aggregating calix[4]arenes carrying four DOTA ligands on the upper rim were synthesized and complexed with Tb<sup>3+</sup>. The luminescence properties of Tb<sup>3+</sup>-DOTA-calix[4]arene-4OPr containing four propyl-groups was investigated and compared with those of the analogue substituted with a phthalimide chromophore (Tb<sup>3+</sup>-DOTA-calix[4]arene-3OPr-OPht). It was shown that, given its four aromatic rings, the calix[4]arene core acts as an effective sensitizer of Tb-centered luminescence. Substituents on the lower rim can modulate the aggregation behavior, which in turn determines the luminescence properties of the compounds. In solid state, the quantum yield of the phthalimide derivative is almost three times as high as that of the propyl-functionalized analogue demonstrating a beneficial role of the chromophore on Tb-luminescence. In solution, however, the effect of the phthalimide group vanishes, which we attribute to the large distance between the chromophore and the lanthanide, situated on the opposite rims of the calix[4]arene. Both, the quantum yields and the luminescence lifetimes show clear concentration dependence in solution, related to the strong impact of aggregation on the luminescence behaviour. Such luminescent calix[4]arene platforms accommodating stable lanthanide complexes can be considered valuable building blocks for the design of dual MR/optical imaging probes.

**Chapter 4** focuses on the application of zeolites as nanocarriers for an increased delivery of lanthanide ions and the design of dual MRI/optical imaging probes. A novel strategy was developed and characterized to selectively deposit Eu<sup>3+</sup> and Gd<sup>3+</sup> ions into distinct framework locations of zeolite-LTL (Linde type L) to exploit the best imaging performance of each

lanthanide. It was demonstrated that the carefully ion-exchanged Gd/Eu-containing nanocrystals acquire exceptional magnetic properties in combination with enhanced luminescence. This smart exploitation of the framework structure yields the highest relaxivity density ( $13.7 \text{ s}^{-1}\text{Lg}^{-1}$  at 60 MHz and 25 °C) reported so far for aluminosilicates, rendering these materials promising candidates for the design of dual magnetic resonance/optical imaging probes, as demonstrated in preliminary phantom and luminescence studies. With the determined characteristics it was possible to derive the most relevant parameters that govern the luminescence and MRI properties. Further investigations showed that there is no detectable leaching of free lanthanide ions in the colorimetric assay with xylenol orange.

To ensure the high lanthanide content in the particles, a synthetic route to prepare size-tunable solid lanthanide carbonate nanoparticles was developed and presented in **Chapter 5**. The size of the particles can be predefined to an accuracy of up to a few nanometers by microwave-assisted temperature control and the choice of aging time. This was the first time that spherical solid lanthanide containing particles in the size range from 20 to 200 nm were made available. The size of the particles determines the biodistribution as well as the imaging properties and is thus of highest importance for imaging and therapeutic applications. To characterize the synthetic mechanism, the theory of homogeneous precipitation and seeded growth was verified by experimental results with good agreement of theory and practice.



## Samenvatting

Sinds de ontdekking van lanthaniden in de 18<sup>de</sup> eeuw fascineren ze wetenschappers vanwege hun overeenkomstig chemisch gedrag en veelzijdige fysische eigenschappen. Het is dus niet verrassend dat lanthaniden deel uitmaken van talloze applicaties in de moderne industrie, elektronica, magneten, lichtbronnen en medische toepassingen. Omdat deze elementen in levende organismen niet van nature voorkomen is het belangrijk om zowel de moleculaire dynamica als de chemische en fysische processen goed te begrijpen, vooral voor *in vivo* toepassingen. In dit proefschrift zijn verschillende lanthanide-bevattende verbindingen en nanodragers onderzocht om meer kennis te vergaren over fundamentele processen die de fysische eigenschappen en syntheseroutes bepalen.

In **Hoofdstuk 1** wordt een kort overzicht gegeven van de geschiedenis van lanthaniden, inclusief een overzicht van enkele chemische en fysische eigenschappen. In de latere paragrafen worden toepassingen van lanthaniden in magnetische resonantie, optische en radionuclide diagnostiek en radiotherapie belicht. Daarnaast wordt de fundamentele achtergrond met betrekking tot de chemische en fysische vereisten beschreven, evenals de benodigde stappen richting optimale imaging reagentia. Recente ontdekkingen op het gebied van toxiciteit worden kort besproken, en de bijdrage van lanthaniden aan de ontwikkeling van multimodale imaging/therapeutische reagentia wordt ook behandeld. De voordelen van grote hoeveelheden lanthanide ionen op een bepaalde locatie te kunnen verzamelen worden beschreven in het laatste deel van het hoofdstuk. Er wordt hier naar verschillende soorten nanodragers, van poreuze tot niet poreuze deeltjes, gekeken.

De volgende hoofdstukken hebben betrekking op studies die zijn uitgevoerd om de moleculaire dynamica in lanthanide-DOTA complexen (**Hoofdstuk 2**), de aggregatie en luminescerende eigenschappen van Ln-DOTA calix[4]arenes (**Hoofdstuk 3**), magnetische en luminescerende eigenschappen en synthese van poreuze (**Hoofdstuk 4**) en niet poreuze (**Hoofdstuk 5**) nanodeeltjes beter te begrijpen.

In **Hoofdstuk 2** wordt de rotatie van de carboxylaatgroepen in DOTA-complexen van verschillende Ln en Sc-ionen onderzocht door middel van DFT berekeningen en <sup>17</sup>O NMR metingen met verschillende temperaturen bij 4.7 – 18.8 T. De verkregen resultaten laten zien dat de rotatie veel langzamer is dan de andere dynamische processen bij deze complexen,

---

zoals de wateruitwisseling in de eerste coördinatiesfeer van het lanthanide-ion. De uitwisseling tussen gebonden en ongebonden zuurstofatomen van de carboxylaatgroep vindt via een overgangstoestand plaats. Daarbij zijn beide zuurstofatomen van de carboxylaatgroep gebonden aan het Ln-ion in het geval van de grotere lanthaniden (La → Sm), terwijl bij de kleinere metaalionen (Tm, Lu, Sc) de carboxylaatgroepen in de overgangstoestand volledig ongecoördineerd zijn. De activeringsvrije energieën vertonen een gestage toename van ongeveer 75 tot 125-135 kJ mol<sup>-1</sup> voor de lanthanidereeks tussen La en Lu. Deze berekende trend is consistent met de resultaten van de <sup>17</sup>O NMR metingen. Snelle uitwisseling tussen gebonden en ongebonden carboxylaatzuurstofatomen werd waargenomen voor de diamagnetische La-DOTA, terwijl voor Pr-, Sm-, Lu- en Sc-DOTA de uitwisseling langzaam was op de NMR-tijdschaal. De trends in de lijnbreedtes voor de verschillende metaalionen als functie van de temperatuur komen overeen met de trend in de snelheden zoals voorspeld door de DFT-berekeningen.

In **Hoofdstuk 3** werden zelfaggregerende calix[4]arenen geconjugeerd met vier DOTA-liganden op de bovenrand gesynthetiseerd en gecomplexeerd met Tb<sup>3+</sup>. De luminescentieeigenschappen van Tb<sup>3+</sup>-DOTA-calix[4]areen-4OPr met vier propylgroepen werden onderzocht en vergeleken met die van Tb<sup>3+</sup>-DOTA-calix[4]areen-3OPr-OPht met een phthalimide chromofoor. Er werd aangetoond dat de calix[4]areenkern werkt als een effectieve sensibilisator van Tb-aangestuurde luminescentie dankzij zijn vier aromatische ringen. Verdere modulatie van de luminescentieeigenschappen van de verbindingen wordt bepaald door het aggregatiegedrag die door de substituenten op de onderrand veroorzaakt wordt. De kwantumopbrengst van het ftaalimidederivaat in de vaste toestand is bijna drie keer zo hoog als die van de propyl-gefunctionaliseerde analoog, wat een gunstige rol van de chromofoor op de Tb-luminescentie aantoont. In oplossing verdwijnt echter het effect van de ftaalimidegroep, wat we toeschrijven aan de grote afstand tussen de chromofoor en het lanthanide, gelegen aan de tegenoverliggende randen van het calix[4]areen. Zowel de kwantumopbrengsten als de luminescentielevensduur in oplossing vertonen een duidelijke concentratieafhankelijkheid, gerelateerd aan de sterke invloed van aggregatie op het luminescentiegedrag. Dergelijke luminescerende calix[4]areenplatformen die stabiele lanthanidecomplexen vormen kunnen als waardevolle bouwstenen beschouwd worden voor het ontwerp van dubbele MR/optische imaging reagentia.

**Hoofdstuk 4** richt zich op de toepassing van zeolieten als nanodragers voor een efficiënte levering van lanthanide-ionen en het design van dubbele MRI/optische imaging reagentia. Er werd een nieuwe strategie ontwikkeld en gekarakteriseerd om selectief  $\text{Eu}^{3+}$  en  $\text{Gd}^{3+}$  ionen af te zetten in verschillende holtes van zeoliet-LTL (Linde type L) om de beste imagingprestaties van elk lanthanide te bereiken. Er werd aangetoond dat een zorgvuldige ionenuitwisseling van Gd/Eu in nanokristallen uitzonderlijke magnetische eigenschappen vertoont in combinatie met verbeterde luminescentie. Deze slimme benutting van de framestructuur levert de hoogste relaxiviteitsdichtheid op ( $13.7 \text{ s}^{-1}\text{Lg}^{-1}$  bij 60 MHz en  $25^\circ\text{C}$ ) die ooit gerapporteerd is voor alumosilicaten, waardoor deze materialen veelbelovende kandidaten zijn voor het design van dubbele magnetische resonantie/optische imaging reagentia. Dit fenomeen werd aangetoond in preliminaire fantoom- en luminescentiestudies. Uit de verkregen waarden was het mogelijk om de meest relevante parameters af te leiden die de luminescentie en MRI-eigenschappen bepalen. Verder onderzoek toonde aan dat er geen detecteerbare uitloging van vrije lanthanideionen plaatsvond zoals bleek uit de colorimetrische test met xylenoloranje.

Om het hoge lanthanidegehalte in de deeltjes te bereiken, werd een synthetische route ontwikkeld om vaste carbonaatnanodeeltjes van lanthaniden te maken zoals gepresenteerd in **Hoofdstuk 5**. De grootte van de deeltjes kan vooraf worden gedefinieerd met een nauwkeurigheid van enkele nanometers door een microwave-gestuurde temperatuurcontrole en de reactietijd keuze. Dit was de eerste keer dat sferische vaste lanthanide-bevattende deeltjes met diameters tussen 20 en 200 nm beschikbaar werden gemaakt. De grootte van de deeltjes bepaalt zowel de biologische verdeling als de imagingeigenschappen en is dus van het grootste belang voor diagnostische en therapeutische toepassingen. Om het synthesemechanisme te bestuderen, werd de theorie van homogene precipitatie en zaadgroei door experimentele resultaten ondersteund met goede overeenstemming tussen theorie en praktijk.





# List of publications

## Publications

1. Luminescence Properties of Self-Aggregating TbIII-DOTA-Functionalized Calix[4]arenes  
F. Mayer, S. Tiruvadi Krishnan, D.T. Schühle, S.V. Eliseeva, S. Petoud, É. Tóth, K. Djanashvili  
*Frontiers in Chemistry*, **2018**, 6, 1-9
2. Prototropic Exchange Governs T1 and T2 Relaxivities of a Potential MRI Contrast Agent Nanozeolite Gd-LTL with a High pH Responsiveness  
W. Zhang, J. A. Peters, F. Mayer, L. Helm, K. Djanashvili  
*J. Phys. Chem. C*, **2015**, 119, 5080-5089
3. Molecular Architecture Control in Synthesis of Spherical Ln-Containing Nanoparticles  
W. Zhang, J. Martinelli, F. Mayer, C.S. Bonnet, F. Szeremeta, K. Djanashvili  
*RSC Advances*, **2015**, 5, 69861-69869
4. Nanozeolite-LTL with Gd<sup>III</sup> deposited in the large and Eu<sup>III</sup> in the small cavities as an MR-Optical imaging probe  
F. Mayer, W. Zhang, T. Brichart, O. Tillement, C. S. Bonnet, É. Tóth, Joop A. Peters, K. Djanashvili  
*Chem. Eur. J.*, **2014**, 20, 3358-3364
5. Rare earth oxysulfide nanoparticles as multimodal imaging agents for T<sub>2</sub>-weighted MR, X-ray tomography and photoluminescence  
S. Osseni, S. Lechevallier, M. Verelst, P. Perriat, J. Dexpert-Ghys, D. Neumeyer, R. Garcia, F. Mayer, K. Djanashvili, J.A. Peters, E. Magdeleine, H. Gros-Dagnac, P. Celsis, R. Mauricot  
*Nanoscale*, **2014**, 1, 555-564
6. Microwave assisted seeded growth of lanthanide-containing nanoparticles for imaging and therapy  
F. Mayer, J.A. Peters, K. Djanashvili  
*Chem. Eur. J.* **2012**, 18, 8004-8007

- 
7.  $^{17}\text{O}$  NMR and Density Functional Theory Study of the Dynamics of the Carboxylate Groups in DOTA Complexes of Lanthanides in Aqueous Solution  
F. Mayer, C. Platas-Iglesias, L. Helm, J.A. Peters, K. Djanashvili  
*Inorg. Chem.* **2012**, *51*, 170-178

## Oral presentations

1. Uniform lanthanide (III)-based nanoparticles as multimodal contrast agents  
SMITH 2012: From preclinical research to clinical application, Bangkok, Thailand, April 10, **2012**
2. Preparation of Uniform Holmium(III)-Based Nanoparticles by Controlled Seeded-Growth  
COST D38 final meeting, Oxford, United Kingdom, September 14, **2011**
3. Calix[4]arenes as Platforms for Fluorescent Amphiphiles  
KNCV/NOW Wageningen symposium, Wageningen, The Netherlands, April 8, **2011**
4. Dynamics of the Carboxylates in Ln-DOTA Complexes studied by  $^{17}\text{O}$ -NMR and DFT calculations  
COST Action D38 – working group meeting, Torino, Italy, March 25, **2011**

## Posters

1. Fluorogenic Click Reactions for Nanoparticles Functionalization  
F. Mayer, B. van der Est, R. Goverde, K. Djanashvili  
Annual meeting COST Action TD1004 “Theranostics Imaging and Therapy: An Action to Develop Novel Nanosized Systems for Imaging-Guided Drug Delivery”, October 28-30, **2012**, London, UK
2. Fluorogenic Click Reactions for Nanoparticles Functionalization  
F. Mayer, B. van der Est, R. Goverde, K. Djanashvili  
NWO study group meeting: Design and Synthesis, October 22-24, **2012**, Lunteren, Netherlands

3. Holmium Based Nanoparticles for Imaging and Therapy  
F. Mayer, J. A. Peters, K. Djanashvili  
Frontiers, Delft, The Netherlands, **2011**
4. Holmium Based Nanoparticles for Imaging and Therapy  
F. Mayer, J. A. Peters, K. Djanashvili  
CHAINS2011, Utrecht, November 28-30, **2011**
5. Fluorescent calix[4]arenes for labelling of supramolecular aggregates  
F. Mayer, S.T. Krishnan, D.T. Schühle, T. Chauvin, É. Tóth, J.A. Peters, K. Djanashvili  
Annula Workshop COST D38 “Metal-Based Systems for Molecular Imaging Applications”, Thessaloniki, Greece, June 21-23, **2010**
6. Synthesis and Cycloisomerization Reaction of 1-Propargyl-2-(2-thienylethynyl)pyridinium Triflates  
F. Mayer, U. Jäger, G. Maas  
Design&Synthesis, Structure & Reactivity and Biomolecular Chemistry, Lunteren, The Netherlands, **2009**
7. Holmium Oxide Based Nanoparticles for Imaging and Therapy  
F. Mayer, J.A. Peters, K. Djanashvili  
Gratama Workshop 2009, Delft, The Netherlands, September 14-15, **2009**



## Acknowledgements

Writing a PhD thesis is always the last part of a long journey, which is filled with interesting, valuable, and unforgettable memories. The most important part of these memories are the people that share them and thus, it is more than appropriate to say ‘Thank you’ at the end of this journey, well knowing, that this piece of work would not have been possible without all these people.

My first and deepest thanks go to my promotor Kristina. Kristina, without your trust and belief in me, I would not have finished this work after all these years. Your way of teaching technical details of the NMR machines, scientific background and the way you accepted my decisions while always letting me feel your support is invaluable. I could not have imagined a better supervisor and I am well aware that you did not always have the easiest time with me. Nevertheless, most importantly, I am proud to call you a friend. Thank you so much for everything!

Next, it is more than appropriate to acknowledge my promotor Ulf. Ulf, I will always remember our interesting scientific discussions, which I really enjoyed and I am happy that you are my promotor. Thank you very much for all your support.

Joop, your dedication to science is absolutely admirable. Although being retired, you were always present and willing to help when there were questions. I will never forget our regular tea-time in the NMR lab with Kristina and Daniel. Thank you very much for being a neverending source of information and a consultant whenever needed.

Thanks are due to Bert Wolterbeek for the collaboration within the 3binding project.

Now it is time to thank a person, without whom I would never even have had the idea to apply for a PhD position in Delft. Daniel, thank you very much for being such a great labmate in Ulm as well as in Delft. I appreciate the time we spent discussing science, traveling for conferences but also the many hours we spent in bars and restaurants having fun.

I owe a deep thanks to all my colleagues of the BOC group. You all made my stay in Delft so pleasant and a great time to remember. Special thanks go to Mieke van der Kooij for all the assistance in organizational things and the willingness to help with whatever she could. I also want to thank Isabel Arends for accepting me in her group at the time I started in BOC and all my labmates from the downstairs and upstairs labs. Frank, Jeroen, Jonathan, Wuyuan,

Maarten, Adeline, Paul, Katya, Serena, Selin, Monica, Caroline, Remco and all the others, thank you for the fun we had together. The same goes for all the guys from the SAS group. Job, Patrick, Christophe, Marta, Dainius, Ivona – it was a pleasure to have you around!

I also want to thank Marcel Bus for all his help with synthetic and analytical issues around the nanoparticles.

I would like to thank the people that were part of the COST actions D38, TD1004 and TD1007 for always welcoming me in a friendly way, sharing scientific interest and making my PhD time in Delft very special due to this strong network.

Kathrin, you always supported me in my decision to do my PhD in Delft although this was not easy for you. Thank you very much for sharing 14 years of your life with me and for all the support during this time.

Martin, after growing up in the same neighbourhood, living over such a large distance makes it difficult to keep a friendship alive. Thank you for always being there and giving me the feeling of coming home, even if we did not meet for a long time.

Denis, thank you for supporting me with electron microscopy and synthetic issues on silica particles and for always being a friend – online and in real life.

Life did not stop after I left the university, and thus, I also met a number of people that contributed in one way or the other to the success of this work.

Mr. Meßmer, I want to thank you for the trust you had, when you hired me and for not accepting that I did not finish this work. Finally, it is done now!

Thanks go to my colleagues in QS/QM for making my professional life so enjoyable and thus giving me the power to finish this thesis next to working.

Special thanks go to Sina, who is there when I need someone to talk, to drink, to dance or to discuss. You became a real friend during the last year. Also thank you for being an essential part of the cover.

Zuletzt möchte ich noch einen tiefen Dank an meine Familie aussprechen, ohne die dies alles nicht möglich gewesen wäre. Mama, Papa und Benni, vielen Dank für die Unterstützung, die ich bedingungslos von euch erhalten habe und auch heute noch erhalte und für das Gefühl immer bei euch daheim zu sein.

## **Curriculum Vitae**

Florian Mayer was born on February 4, 1983 in Ehingen (Donau), Germany. He went to school in Allmendingen and Ehingen (Donau) and obtained his secondary school degree from Gymnasium Ehingen in 2002. After social service he started his studies of chemistry at the University of Ulm (Germany) in 2003 and graduated with the thesis entitled XXX at the department “Organische Chemie I” under the supervision of Prof. G. Maas in 2008. In the year of his graduation, he received the Dr. Barbara Mez-Starck award for the best students of each year.

In 2009 he started his PhD at the Delft University of Technology in the Biocatalysis and Organic Chemistry group under the supervision of Dr. K. Djanashvili. He was focusing on the synthesis and investigation of different lanthanide containing compounds to gain deeper knowledge of fundamental processes governing the properties relevant for medical imaging. After he left the university, he started working in pharmaceutical industry and stayed there since October 2014.